PARALLELIZED CARTESIAN GRID METHODOLOGY FOR NON-EQUILIBRIUM HYPERSONIC FLOW ANALYSIS OF BALLUTES

A Thesis
Presented to
The Academic Faculty

by

Jin Wook Lee

In Partial Fulfillment
of the Requirements for the Degree
Doctor of Philosophy in the
School of Aerospace Engineering

Georgia Institute of Technology
August 2007

PARALLELIZED CARTESIAN GRID METHODOLOGY FOR NON-EQUILIBRIUM HYPERSONIC FLOW ANALYSIS OF BALLUTES

Approved by:

Dr. Stephen M. Ruffin, Adviser
School of Aerospace Engineering
Georgia Institute of Technology

Dr. Mitchell Walker
School of Aerospace Engineering
Georgia Institute of Technology

Dr. Marilyn J. Smith
School of Aerospace Engineering
Georgia Institute of Technology

Dr. Shuangzhang Tu
School of Engineering
Jackson State University

Dr. Robert D. Braun
School of Aerospace Engineering
Georgia Institute of Technology

Date Approved: 9 July 2007

...to my parents

and Jenny, Michelle and Joshua

ACKNOWLEDGEMENTS

As I terminate ten years of my education in Aerospace Engineering, I must express my sincerest appreciation to two very special mentors in my career: my advisor Dr. Stephen M. Ruffin and my undergraduate advisor Dr. T.Q. Dang. Firstly, I would like to thank Dr. Ruffin for infusing in me the concrete fundamentals of CFD and an incisive mind to break up difficult engineering problems to manageable pieces, through many of his lectures and uncountable pieces of advice during meetings. I would like to thank Dr. Dang for inspiring me, when I was quite clueless back then, to appreciate the beauty of fluid dynamics and the joy of learning. I would not have been able to reach this point without their great devotion and endless patience.

I would like to thank Dr. Marilyn Smith for her insightful advice during the thesis proposal. I would like to thank Reuben Rohrschneider and Dr. Robert Braun for providing me with a chance to look at the bigger picture, outside my areas of expertise. Reuben provided many useful tool sets and data for this thesis.

I would like to thank my former labmate J.D. Lee for the many nights of discussions and for sharing many good memories at Georgia Tech. I would also like to thank all my former and current labmates of ARTLAB; David Marshall, Susheel K. Sekhar, Tim Eymann, Srujal Patel, Alessio Orssini, Joel Malo-Molina, and Alexander Pace for their team work and friendship.

I am grateful to my parents, Sooyong Lee and Mikyung Sohn, for their unconditional support and love. It should have been difficult for them to send their sixteen year old son thousands of miles away to follow his dream. I only hope to pass on a portion of their love to my children, Michelle and Joshua.

Finally, I wish to say thank you to my wife, Jenny, for her love and all the six

years of sacrifice for this degree, which includes financial obligations. At this moment of starting a new chapter of my life, I am very grateful that she is with me.

TABLE OF CONTENTS

LIST OF TABLES

LIST OF FIGURES

SUMMARY

Hypersonic flow analysis is performed on an inflatable aerocapture device called a "Ballute" for Titan's Mission. An existing unstructured Cartesian grid methodology is used as a starting point by taking advantage of its ability to automatically generate grids over any deformed shape of the flexible ballute. The major effort for this thesis work is focused on advancing the existing unstructured Cartesian grid methodology. This includes implementing thermochemical nonequilibrium capability and porting it to a parallel computing environment using a Space-Filling-Curve (SFC) based domain decomposition technique.

The implemented two temperature thermochemical nonequilibrium solver governs the finite rate chemical reactions and vibrational relaxation in the high temperature regimes of hypersonic flow. In order to avoid the stiffness problem in the explicit chemical solver, a point implicit method is adopted to calculate the chemical reaction source term. The AUSMPW+ scheme with MUSCL data reconstruction is adopted as the numerical scheme to avoid non-physical oscillations and the carbuncle phenomenon. The results for five species air model and for thirteen species N2-CH4-Ar model to simulate Titan entry are included for verification against DPLR (NASA Ames' structured grid hypersonic flow solver).

The efficient parallel computation of any unstructured grid flow solver requires an adequate grid decomposition strategy because of its complex spatial data structure. The difficulties of even and block-contiguous partitioning in frequently adapting unstructured Cartesian grids are overcome by implementing the 3D Hilbert SFC. Grids constructed by the SFC for parallel environment promise short inter-CPU communication time while maintaining perfect load balancing between CPUs. The load

imbalance due to the local solution adaption is simply apportioned by re-segmenting the curve into even pieces. The detailed structure of the 3D Hilbert SFC and parallel computing efficiency results based on this grid partition method are also presented.

Finally, a structural dynamics tool (LS-DYNA) is loosely coupled with the present parallel thermochemical nonequilibrium flow solver to obtain the deformed surface definition of the ballute.

Nomenclature

Abbreviation

AUSM: Advection Upstream Splitting Method

AUSMPW: Advection Upstream Splitting Method with Pressure Weight Function

BAAT: Ballute Aeroelastic Analysis Tool

CFD: Computational Fluid Dynamics

CFL: Courant-Friedrichs-Lewy, Time Step Constraint for Numerical Scheme

CPU: Central Process Unit

DPLR: Data-Parallel Line Relaxation, Hypersonic Aerothermodynamic CFD Tool

LAURA: Langley Aerothermodynamic Upwind Relaxation Algorithm, Hypersonic Aerothermodynamic CFD Tool

LS-DYNA: Livermore Software Dynamics, Structural Dynamics FEA Solver

MPI: Message Passing Interface

MUSCL: Monotone Upstream-Centered Scheme for Conservation Laws

NASA: National Aeronautics and Space Administration

NASCART-GT: Numerical Aerodynamic Simulation via CARTesian Grid Techniques, Solution Adaptive Unstructured Cartesian Grid Flow Solver

SFC: Space Filling Curve

Alphanumeric

$\hat{g}_i^{P_{1atm}}$ Gibb's free energy per unit mole at 1atm

$\Re$ Universal gas constant

$\mathbf{R}$ Summation of the species fluxes

$\vec{F}, \vec{G}, \vec{H}$ Flux vectors in the X, Y, Z directions

$\vec{S}$ Source term vector due to chemical reaction or/and vibrational excitation

$\vec{U}$ State Vector

A Slope coefficient for vibrational relaxation

a Speed of Sound

c_i Mass concentration of species i

C_p Specific heat capacity at constant pressure

C_v Specific heat capacity at constant volume

E_t Total energy

E_{ve} Vibrational-Electronic energy

H Total enthalpy

h_{0i} Heat of formation of the species i

H_{normal} Averaged sensible enthalpy containing normal component of kinetic energy

k_b Backward reaction rate coefficient

K_c Equilibrium Constant

k_f Forward reaction rate coefficient

M Mach number

MW Molecular weight

N_R Total number of reaction step

N_s Total number of species

P Pressure

q^R_{coup} Coupled radiative heat flux

q^R_{unc} Uncoupled radiative heat flux

R Specific gas constant

T Translational-Rotational temperature

T^0 Initial guessed translational-rotational temperature

T_{ve} Geometrically averaged chemical reaction temperature

T_{ve} Vibrational-Electronic temperature

u, v, w Velocities in the X, Y, Z directions

V Volume

X_i Molar concentration of the species i

Greek

α Numerical diffusivity control constant for AUSMPW+

Γ The Goulard number

γ Numerical ratio of specific heat

$\mu_{i,j}$ Reduced mass of the species i and j

$\nu^{'}_i$ Stoichiometric coefficient of the reactant of the species i

ω_{ve} Vibrational-Electronic source term

ρ Density

τ^{MW} Molar averaged vibrational relaxation time

τ^{p} Vibrational relaxation time of Park's high temperature correction

τ_c Species gradient based solution adaption criteria

τ_d Velocity divergence based solution adaption criteria

$\tilde{\kappa}$ The mixture specific constant for radiation

Subscript

$\frac{1}{2}$ At the cell interface

i Species i

L Left side of the cell interface

R Right side of the cell interface

rot Rotational energy mode

tr Translational energy mode

ve Vibrational-Electronic

Superscript

$*$ Nondimensional Value

n N^{th} Time Step

CHAPTER I

INTRODUCTION

1.1 Hypersonic Flow Analysis on Ballute Aerocapture Device

1.1.1 Ballute Aerocapture

A ballute (Balloon + Parachute = Ballute)[13] is an inflatable drag device, designed to be used for slowing down a spacecraft in an interplanetary mission. It was originally referred to an IAD (Inflatable Aerodynamic decelerator). It is typically considered for aerocapture missions which require the vehicle to remain in orbit while extracting desired scientific data [1]. Aerocapture is a form of areoassist maneuvers that uses a planet's atmosphere to slow down the spacecraft to orbital capture velocities in a single path. It results in significant mass and cost reduction compared to other propulsive methods [14] [15]. A ballute can also be used for planetary entry applications, as well as for military applications as a decelerator.

As shown in Figure 1, the ballute gets deployed from the spacecraft at the atmospheric entry interface and is released when the spacecraft gets sufficiently decelerated.

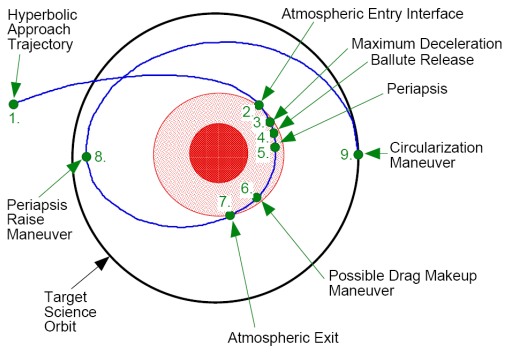

Figure 1: Example of Clamped and Trailing Ballutes [1]

It is made out of a thin flexible polymer film or Carbon-fiber material with pressurized gas inside so that it can have a significantly larger cross-sectional area per unit mass, when compared to other types of aerocapture devices such as rigid aero-shells. A larger cross-sectional area has three advantages in lowering surface heating at the stagnation point. First, it captures a larger volume of gas and generates more drag so that it can achieve the same $\triangle V$ at a higher altitude. Since the gas is thinner at higher altitudes, the amount of surface heating decreases. Second, the larger radius has a smaller velocity gradient within the boundary layer, which results in smaller convective heat transfer. Third, the larger cross-sectional area produces greater shock stand off distances. It gives the gas a longer vibrational relaxation and chemical reaction time to lower the highly significant translational temperature at the stagnation point.

Previous studies [16] [17] indicate that the amount of increase in payload mass using this thin ballute technology is typically more than 100%, compared to rigid aero-shells, in the most missions that require orbital insertion or entry into planets with atmospheres. For the Titan organic explorer mission, the ballute to spacecraft system mass fraction is estimated to be 17% and the aero-shell to spacecraft system mass fraction is estimated to be 41.5%.

1.1.2 Aerothermodynamic Characteristic of Different Ballute Configurations

Various ballute configurations have been proposed and studied [18] [19] [3] [1] [20] [21] [22] as shown in Figure 2, and they can be categorized into three elementary configurations in terms of their flow patterns and aerothermodynamic characteristics: the towed spherical ballute, the towed toroidal ballute, and the clamped ballute.

The towed spherical configuration can have a single tether, which connects the spacecraft and the ballute, aligned with the streamlines. Therefore, the tether itself does not experience severe thermal or mechanical loads. Also, it is relatively easy

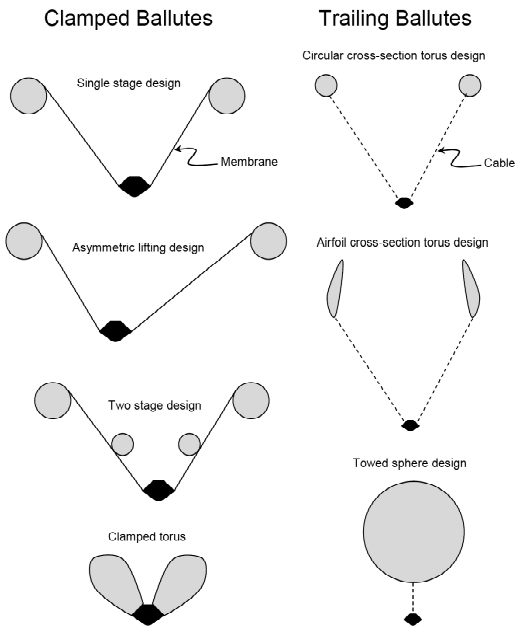

Figure 2: Example of Clamped and Trailing Ballutes [2]

to manufacture and structurally reliable. However, it is expected to have strong shock-shock interactions between the spacecraft and the ballute. In 2001, Hornug [3] performed inviscid perfect gas CFD simulation over two bodies in tandem as shown in Figure 3. This study observed a strong unsteady shock-shock interaction in the elliptical trailing body. The interaction of the bow shock of the leading body (spacecraft) with the shock of the rear body (ballute) caused the violent local increase in pressure to occur in front of the rear body, which in turn caused a shock wave to propagate forward and even to upstream of the leading body. This shock was then washed downstream again, until the leading body's shock impinged on the rear body, and the process repeated itself.

The towed toroidal configuration can also expect some unsteady shock-shock interactions but it should not affect the stability of the ballute because the supersonic wake developed from the parent spacecraft would pass through the toroid hole, as shown in Figure 4, if the radius of the toroid and the distance to the leading spacecraft are properly designed. However, a previous study by Rasheed, Fufii, and Hornung [19]

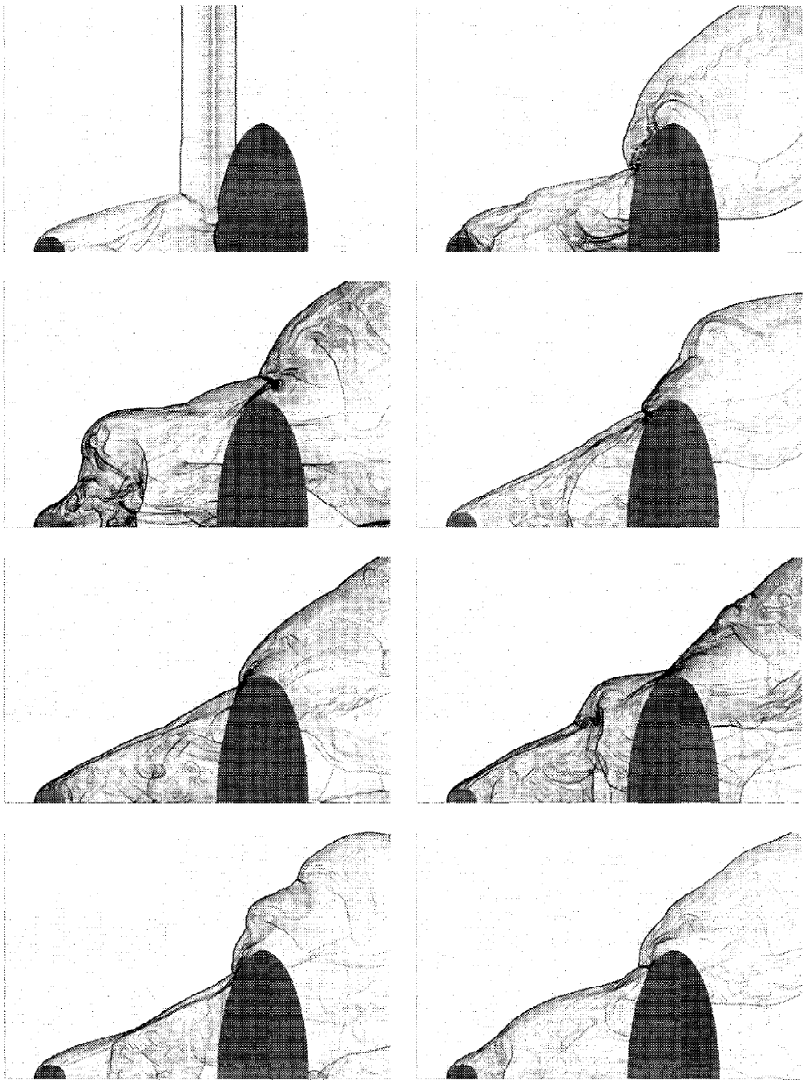

Figure 3: Unsteady Flow over a Spacecraft and simple Ballute in Tandem. Mach number=10, specific heat ratio=1.2. [3]

showed that the high heat flux resulting from the small minor radius of the torus would be a major issue for consideration.

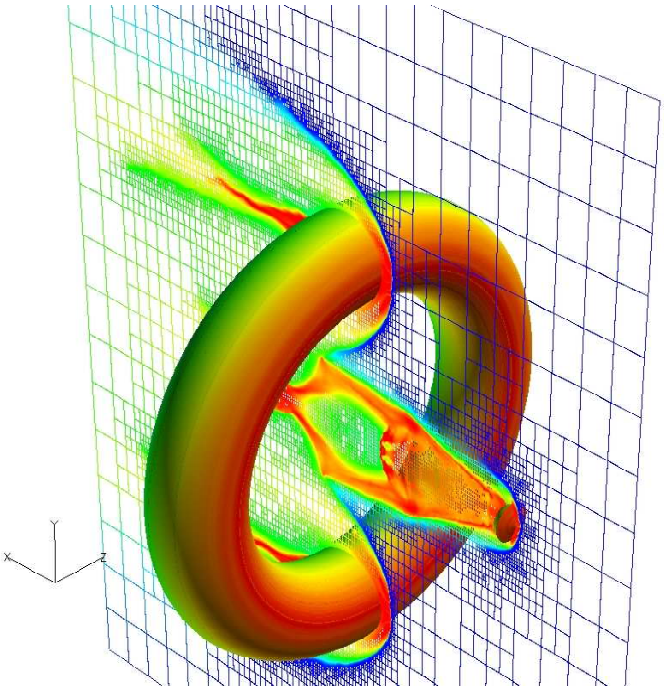

Figure 4: Flow over toroidal ballute, Temperature Contour

For the attached clamped ballute configuration, the unsteadiness effects become significantly reduced when compared to the towed systems. A similar configuration was also simulated in Hornung's 2001 paper [3] as shown in Figure 5. This was because the domain where the shocks dynamically interact becomes significantly smaller when the spacecraft and the ballute were attached to each other. Even more, this shock-shock interaction could be completely removed if the junction between the spacecraft and the ballute was continuously configured.

Previous aerothermodynamics analyses on various ballute configurations have showed that the negative effects from unsteady shock-shock interactions and the significant heating issue could be avoided by selecting the clamped ballute configuration. Therefore, the present work focuses on predicting the flow environment of a clamped ballute.

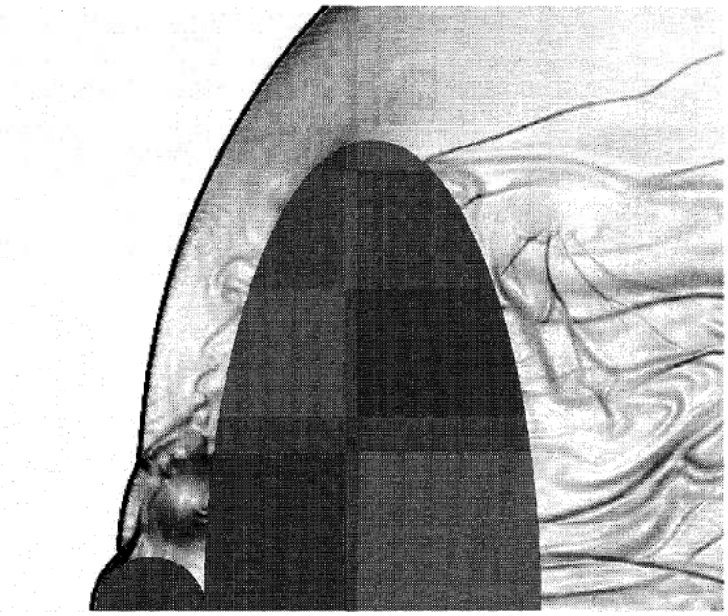

Figure 5: Flow over Clamped Ballute Configuration

1.1.3 Preceding Efforts in Ballute Aeroelastic Analysis

Ballutes are made out of flexible material. Therefore, their aeroelastic response to the aerodynamic loads have been studied by Rohrschneider [2] in a collaborative effort with the presented work. Rohrschneider used various high and low fidelity aerodynamic tools, including the unstructured Cartesian grid based perfect gas flow solver, NASCART-GT, to link them to an existing structural dynamics code, LS-DYNA. A loosely coupled method is used in this work. The surface pressure obtained from the converged steady state solution of the aerodynamic tool was transferred to LS-DYNA as the input load. The converged deformation data obtained from the steady solution of LS-DYNA was transferred back to the aerodynamics tool as the input geometry. These processes were repeated until the final deformed shape was obtained. His work also included the development of BAAT (Ballute Aeroelastic Analysis Tool), which offers a flexible interface between various aerodynamic and structural dynamics tools. In order to ensure the credibility of LS-DYNA and of

the selection of parameters, buckling of an inflated mylar column due to an axial force, and that of an inflated torus due to a radial force have been tested in his work. Both these tests showed good comparisons with experimental data. Figure 6 shows the coupled results of LS-DYNA and the current parallelized unstructured grid flow solver, NASCART-GT, in the perfect gas mode. It shows a good agreement in the overall shock structure and the structural deformation.

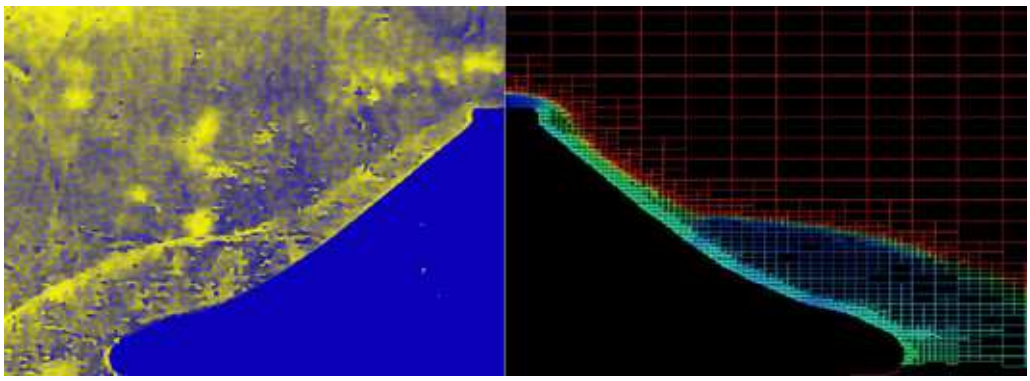

Figure 6: NASCART-GT and LS-DYNA validation(Right: Mach Number) against Wind Tunnel Schlieren Photograph[2](Left)

1.1.4 Research Objectives

The overall objective of this thesis is to predict hypersonic nonequilibrium flow environment around an interplanetary aerocapture device called "ballute" by advancing an existing unstructured Cartesian grid based methodology. The first enhancement is the parallelization of the flow solver using a space filling curve based grid partitioning strategy. The second enhancement is the incorporation of a thermochemical nonequilibrium flow solver to simulate high speed and high altitude flow environment. The present work focuses almost exclusively on inclusion of 3-D inviscid gas dynamics and reacting flow physics necessary for accurate predictions of surface pressure and aerodynamic forces for hypersonic bodies. Therefore, rigorous aerothermodynamic predictions such as of wall temperature and convective heat transfer rate have been included as recommendations for future development in this thesis. An existing serial

and perfect gas solver, NASCART-GT is used as the starting point for this work. Recently, much effort in Cartesian grid technology has been focused on the extension of the viscous capability [23] [24] [25] [26] [27] [28] [29]. However, only one preceding work [9] has been done in extending it to the hypersonic regime and even this work has not been extended to 3D. Cartesian grids have some advantages in calculating inviscid fluxes over other unstructured grid topologies like tetrahedral or prismatic grids. A Cartesian grid uses perfectly orthogonal grid cells with the body "cutting" through a background computational mesh. Therefore it does not require complex coordinate transformations or computation of contravariant velocities, so the truncation error is significantly reduced. Also, the Cartesian grid based approach has the advantage of relative computational simplicity due to the elimination of the need for a body fitted mesh. Its ability to automatically generate grids over very complex geometries by intersecting the solid surface with the mesh releases CFD users from the agony of the time consuming effort during grid generation processes. In this chapter, the background and motivation for the present research are discussed in three short sections. The first is the hypersonic nonequilibrium flow analysis on the ballute. The second is the development of the hypersonic thermochemical nonequilibrium solver. The third is the domain decomposition strategy for efficient parallelization.

In this work, effort in developing the parallelized unstructured Cartesian grids based nonequilibrium flow solver will be used to perform hypersonic flow analysis on a clamped ballute in the continuum regime of Titan's atmosphere, which is essential for aerocapture missions. Titan is the largest moon of Saturn and is the only known moon in the solar system that has a fully developed atmosphere. The density of the atmosphere of Titan is actually greater than that of Earth's with a surface pressure greater by 50%. The atmosphere is composed mainly of nitrogen, which accounts for approximately 80% to 98% by volume depending on the altitude and the season,

with the balance being argon and significant traces of hydrocarbon elements. Hydrocarbon elements are the building blocks for amino acids, a necessary ingredient for the formation of life. For this reason, Titan is of significant interest to the scientific community for the understanding of early formation of life here on Earth.

A thirteen species N2-CH4-AR chemical system is simultaneously solved with two temperature thermodynamics nonequilibrium model to understand the flow physics around the ballute. The points of interest in this analysis are the flow properties within the shock layer and the pressure load on the surface. Since the shock formation and flow variables are largely dependant on the shape of ballute, its deformation has to be taken into account for realistic flow analysis using LS-DYNA and BAAT.

1.2 Development of Thermochemical Nonequilibrium Solver

1.2.1 High Temperature Effects in Hypersonic Flow

Hypersonic flow is categorized by certain physical phenomena that do not typically play an important role in supersonic flow. These effects could be thin shock layers, high gradient entropy layers, viscous interactions due to the high displacement thickness of boundary layers, and high temperature gas effects.[30] In this subsection, some of high temperature gas behavior will be discussed with an example of air at 1 atm.

At temperatures less then 500K-800K, the gas stays calorically perfect. Only translational and rotational internal energy modes are fully excited while the excitation of the vibrational mode and chemical reactions are negligible, as a result specific heat capacities remains constant. This regime corresponds to $M_\infty \sim 3$ at ambient sea level condition.

For temperatures around 800K-2000K, the vibrational mode takes an important role in sharing the total energy with the translational and rotational modes. Near the lower temperature limit of this regime, vibrational-transitional(V-T) energy exchange between harmonic oscillator molecules dominates because most of the molecules are

near the ground vibrational state. Near the higher limit of this regime, vibrational-vibrational(V-V) energy exchange becomes significantly active because not only are vibrationally excited molecules highly populated but also V-V exchange rate is considerably faster than its V-T counter-part. Also, the vibrational oscillation becomes anharmonic as the temperature approaches the dissociation level. However, results within the harmonic oscillator approximation are known to be sufficiently accurate enough for most practical purposes[31]. This regime corresponds to $M_\infty \sim 4$ to $M_\infty \sim 7$ at ambient sea level conditions.

For temperatures above 2000k-2500k, the vibrational mode is fully excited and O2 starts dissociating. Around 4000k, O2 is completely dissociated and N2 starts dissociating. This regime corresponds to $M_\infty \sim 9$ to $M_\infty \sim 17$ at ambient sea level conditions.

When the temperature reaches 9000k, most of the N2 is dissociated. Coincidentally, this is the temperature around which the both dissociated N and O atoms become ionized. Around 12000k, all the gases are completely dissociated and about 14% of them are ionized such that there is a sufficient amount of free charges, enough to make electromagnetic forces(plasma). Radiation emitted and absorbed by the gas can become important and could eventually modify the energy distribution in the flow field. At 20000k, double dissociation begins. And finally when it reaches 30000k, the gas is completely ionized [32]. These regimes correspond to M_∞ greater or much greater than 30.

As stated earlier, these temperature brackets are based on air at 1 atmosphere. However, the range within which the physics described above occurs is also affected by the pressure. By the Le Chatelier's principle, chemical reactions lead to an increase in the number of moles at lower pressure. Therefore, molecules are more likely dissociate at higher altitudes.

All of the described effects in the above paragraphs, except for radiation, are

due to molecular collisions which occur at finite rates. When the collision rates are much faster than flow rates, then it is called as 'equilibrium flow'. Alternatively, if the collision rates are much slower than flow rates, it is called as 'frozen flow'. Unfortunately, neither of these two situations can completely describe the hypersonic flow over a space/air vehicle. There will always be regions where the collision rates are in the same vicinity of the flow rates, moreover different species will have different reaction rates and different vibrational relaxation rates. Therefore, energy transfers between bulk kinetic energy, translational energies, chemical energies, and vibrational energies of different species are actively in progress at many locations in a hypersonic thermochemical nonequilibrium flow. When these effects starts to play dominant roles then this kind of a flow is called 'nonequilibrium flow'.

When the flow is assumed to be in vibrational equilibrium while computing the finite chemical reaction rate, then it is called a chemical nonequilibrium model. This model is appropriate for the state of small departures from chemical equilibrium. When both the finite vibrational relaxation and finite chemical reaction rate are taken into account but V-V exchange rates among all polyatomic species are assumed to be equilibrium, then it is called a two temperatures thermochemical nonequilibrium model. This model is appropriate for systems composed of polyatomic molecules that have similar vibration rates.

Aeroassist devices, such as a ballute, are typically operated in nonequilibrium flight regimes. Figure 7 shows that the thermochemical nonequilibrium effects are dominant at region ©, which is about 70 to 110km high depending on the speed in the earth's atmosphere into which an aeroassist maneuver falls. The physical explanation for this classification lies in the varying molecular collision rates, which get reduced at higher altitudes due to relatively larger mean free paths. The mean free path is linearly proportional to the pressure. Considering that the pressure at an altitude of 80km in the earth's atmosphere is around 1Pa and that the highest

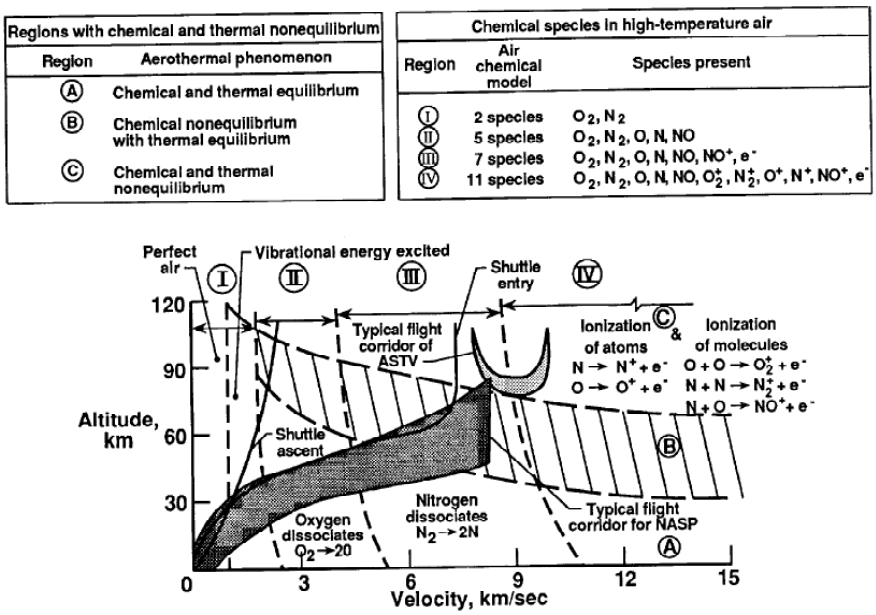

Figure 7: Comparison of vehicle flight regimes in Earth's atmosphere [4] [5]

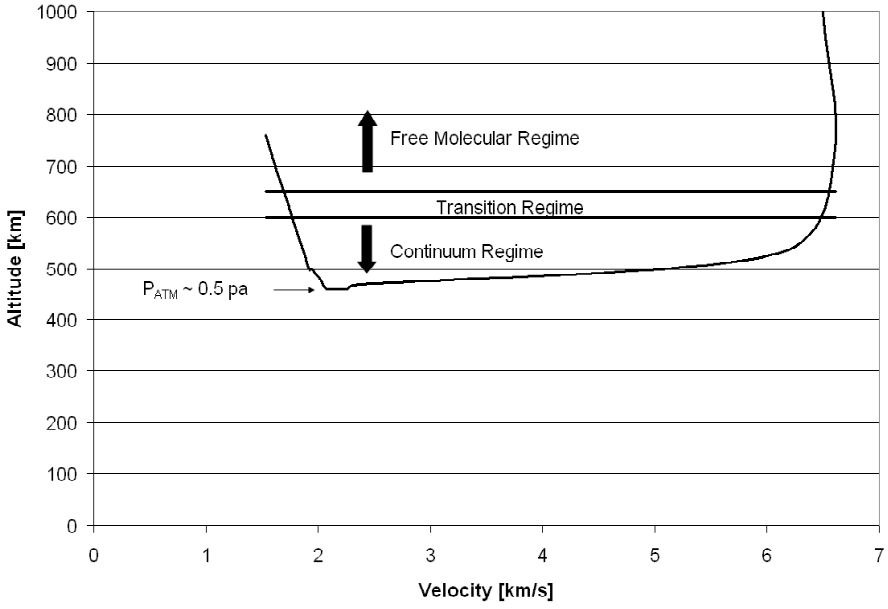

Figure 8: Altitude vs. Speed for Ballute flight regime at Titan with -39^o entry flight angle

pressure that the ballute experiences is about 0.5Pa in Titan's atmosphere, as shown in Figure 8, it can be inferred that the aerocapture mission of a ballute in Titan's atmosphere occurs in the nonequilibrium flight regime.

In fact, the operating altitude is so high that some parts of the trajectory fall into free molecular regimes. However, as shown in Figure 8 since most of the deceleration and deformation occur in the continuum regime, hypersonic flow analysis can be performed with the continuum assumption. The data in figure 8 has been taken from reference [33].

1.2.2 Existing Hypersonic Analysis Tools

In the past years, interest in various types of vehicles in hypersonic flow regime produced numerous structured grid based nonequilibrium flow solvers. According to recent publications, Laura, DPLR, and Lore are the most frequently referenced and are intensively validated against each other[34] and also against wind tunnel tests.

LAURA(Langley Aerothermodynamic Upwind Relaxation Algorithm) is mainly developed by Peter Gnoffo at the NASA Langley Research Center [35] [18] [36] [7] [37]. It uses Roe's flux difference splitting scheme with Yee's second-order symmetric total variation diminishing scheme to model the inviscid fluxes. Steady state solution is obtained using either point or line relaxation time integration scheme. The vibrational energy mode is assumed to be in equilibrium with the electronic energy, and translational energy is assumed to be in equilibrium with the rotational energy mode. The code supports multi-block structured grids and MPI communication for massive parallel computing.

DPLR is initially developed at University of Minnesota by Michael Wright and Graham Candler [38] [39]. This is further developed at NASA Ames research center [40] [12] [34]. DPLR(Data-Parallel Line Relaxation) implicit method is optimized for efficient parallel computing by arranging the body normal dependent data within

local CPU in order to perform the relaxation process simultaneously in parallel mode. DPLR uses third order modified Steger-Warming flux splitting scheme with MUSCL data reconstruction to model the inviscid fluxes. Unlike LAURA, the vibrational energy mode is separately treated from the electronic energy modes, and translational energy is assumed to be equilibrium with the rotational and electronic energy mode. It also supports multi-block structured grids. Some of the present works are validated against this code.

Lore [41] was developed at the Advanced Operations and Engineering Services Group in Europe. The flow solver uses modified AUSM scheme with MUSCL data reconstruction to achieve second-order accuracy coupled with a van Albada limiter. Time advancement to a steady-state solution is achieved using an alternating direction line Gauss Seidel implicit relaxation method. The code supports multi-block structured grids. This code covers a wide range of flight regimes from subsonic to hypersonic.

The current maturity of structured grid based codes is far beyond that for unstructured grid solvers in terms of accuracy and comprehensiveness of the physical models. Much of current effort is focused on the transition model to turbulence and more sophisticated radiative heat transfer predictions.

1.2.3 Background and Motivations to Use Unstructured Cartesian Grid Technique for Hypersonic Flow

In order to investigate the optimum configuration for various types of hypersonic vehicles, a nonequilibrium flow computational fluid dynamics tool with advanced grid techniques, which can handle complex geometries and flow fields with minimum user intervention, is desired. In order to fulfill these requirements, several adaptive unstructured grid solvers have been developed.

Aftosmis and Baron[6] developed a 2D solution adaptive algorithm to resolve a shock wave in hypersonic chemical nonequilibrium flow, figure 9. This method locally

refines the computational cells by sub-dividing the existing curvilinear mesh based on density and mass concentration gradients provided by the developing solution. This adaptive technique saves considerable amount of computation time compared to globally refined structured grids, as well as reducing human effort. However, this method involves the initial effort of generating curvilinear grids and is not adequate for complex geometries.

Gnoffo and his HEFSS(High Energy Flow Solver Synthesis) colleagues re-engineered and synthesized the existing analysis capabilities in LAURA (Structured grid hypersonic Navier-Stokes solver focused on external flow) and VULCAN (Structured grid N-S solver focused on internal flow) into a well known tetrahedral grid based unstructured grid solver, FUN3D [36] [7], figure 10. The essence of this synthesis was to significantly reduce the time and effort in generating grids and to obtain more control over the grid quality around complex shapes by utilizing the advanced grid topology of FUN3D. However, the stagnation heat was poorly predicted while comparing with the results of LAURA. According to their analysis, the primary cause of heating degradation arises from how the inviscid flow gets processed crossing the shock and shock layer to the edge of boundary layer; and not from poor formulation of viscous terms across the boundary layer itself. Other researchers [42] [8] also indicated that it is difficult to obtain second-order accurate flux reconstruction on stretched tetrahedral cells.

With the above issues from the HEFSS group in mind, Candler and his research group [8] [43] developed a new implicit unstructured grid solver, figure 11. They were able to improve the solution by using hexahedral and prismatic structured-like grids wherever possible, and using tetrahedral grid elements only where necessary, with the cost of increased user intervention. However, even while using a high-quality hexahedral grid near the surface, tetrahedral grid introduced errors near the bow shock. This work demonstrated the basic principle that a good grid design is still

critical for accurate solutions even in a modern unstructured grid solver.

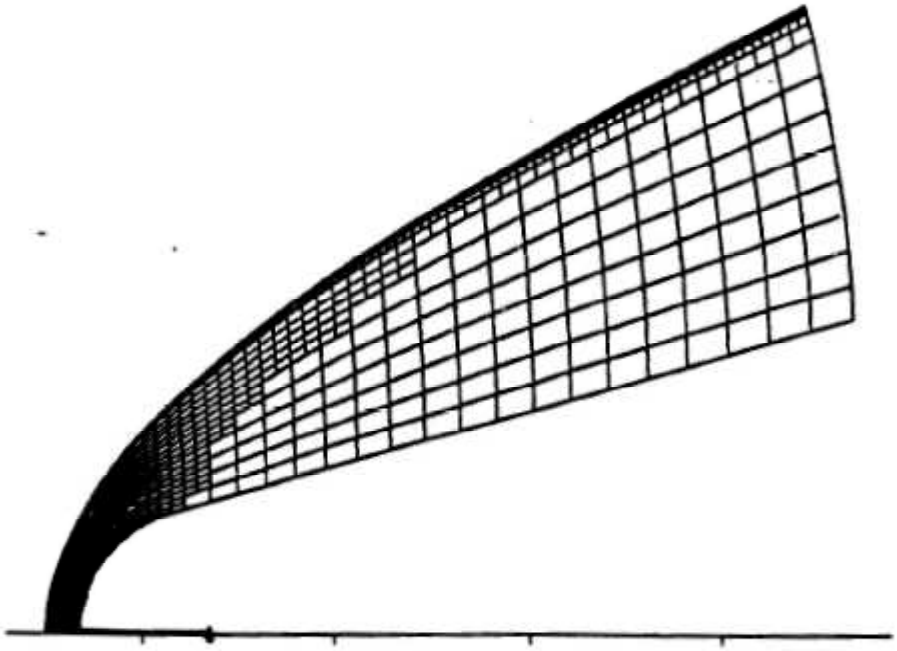

Figure 9: 2D Curvilinear Adaptive Grids [6]

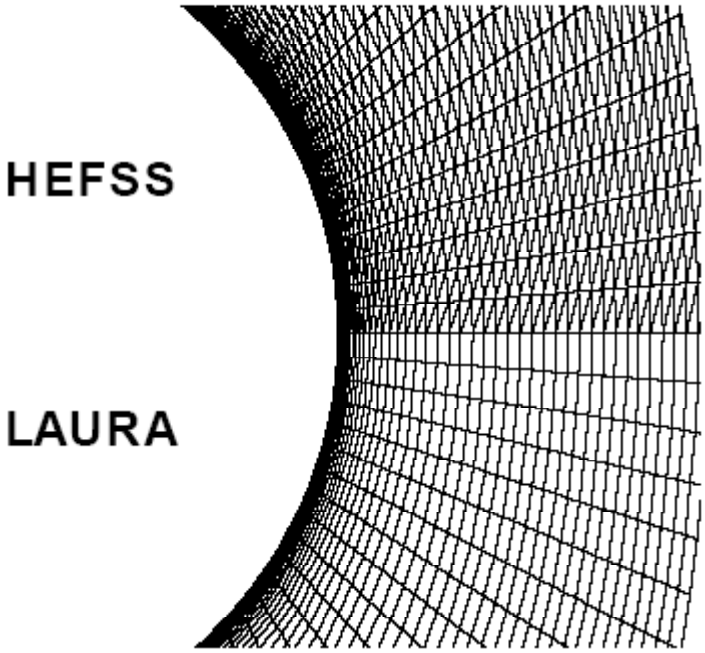

Figure 10: Structured Grid from LAURA and Tetrahedral Grids from FUN3D over Cylinder for Hypersonic Test Case [7]

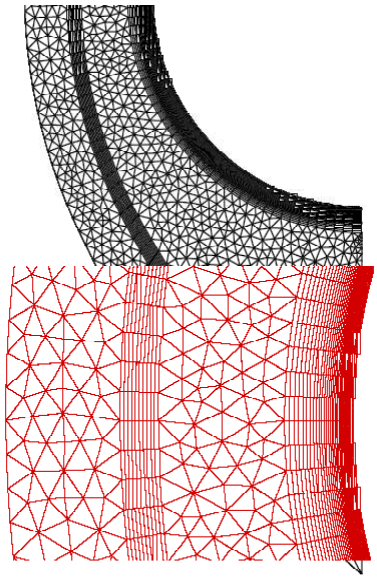

Figure 11: Quadrilateral-Tetrahedral Hybrid Unstructured Mesh over Cylinder for Hypersonic Test Case [8]

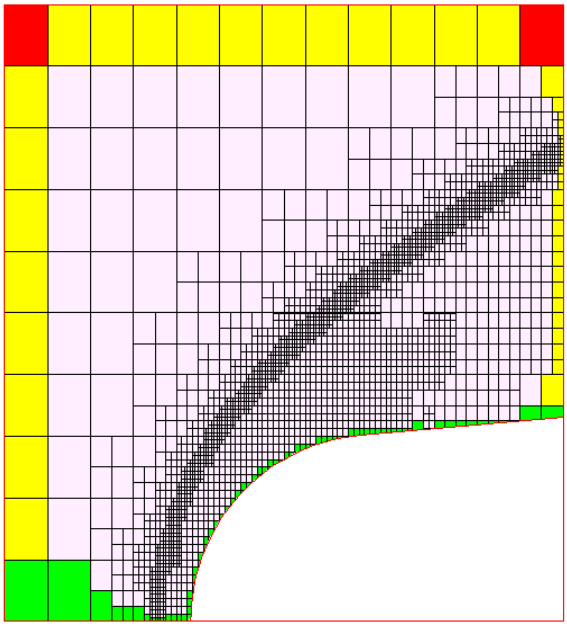

Figure 12: Cartesian Unstructured Mesh over Cylinder for Hypersonic Test Case [9]

One objective of this research is to add inviscid-nonequilibrium chemistry capability to an existing solution adaptive, unstructured Cartesian grid based, calorically perfect gas solver, NASCART-GT, as a preliminary phase of developing the unstructured grid based, hypersonic aerothermodynamics tool. Although, as described in the earlier section, Cartesian grids have many attractive features in computing inviscid fluxes when compared to other grid topologies, only one preceding work had been done in this area by Tu and Ruffin. In 2001, Tu and Ruffin[9] developed a 2D solution adaptive Cartesian grid based thermochemical nonequilibrium solver on a completely different platform from NASCART-GT.

1.2.4 Titan hypersonic flow analysis

For the successful landing of Titan Huygens Probe on January 14, 2005, there have been many efforts in predicting the flow environment numerically. In 1989, Nelson, Park, and Whiting [44] initiated the shock layer analysis with an one dimensional thermochemical nonequilibrium code. This paper also presented the collection of chemical kinetics of a N2-CH4 system, which has been commonly referred to the Nelson model in later literatures. In 1990, Park and Bershader [45]did more a in depth study of the CN radiation by calculating the major species and conducting shock tube measurements in the post shock region. In 1997, Koffi-Kpante, Zeitoun, and Labracherie [46] numerically showed that the radiative heating due to CN can be the dominating heat transfer mechanism rather than convective heating. Since the contribution of radiative heating is largely dependant on the concentration of methane in the atmosphere, the uncertainties in the atmospheric composition can cause a large variation in the predicted total radiative heat. In 2003, for a possible follow up to the Cassini-Huygens mission, Takashima, Hollis, Zoby, Sutton, Olejniczak, Wright, and Prabhu [47] conducted preliminary aerothermodynamics study for a Titan aerocapture aeroshell under the NASA In-Space Propulsion program. This study included

a relatively comprehensive set of species: N_2, N, N_2^+, C, C^+, C_2, CH, CH_2, CH_3, CH_4, H, H^+, H_2, CN, CN^+, NH, e^-. It compared different ionization reactions between Nelson's and Park's models, which resulted in large variations(more than a factor of two) in the radiative heat transfer rate. In 2004, Gökçen proposed a new set of chemical kinetics models for the N2-CH4-Ar system based on recent literatures. This new model not only includes more detailed reaction steps but the fundamental reaction rates are also very different from the previous Nelson model. He also proposed a simplification of the detailed reaction model for the purpose of entering onto Titan atmosphere to make it practical for CFD calculations. In 2004, Wright, Bose, and Olejniczak developed a methodology that could fully couple flow field with radiations. This flow field and radiation coupling addresses a non-adiabatic flow field thus it significantly reduces the temperature within the shock layers, correcting the over-predicted radiative heat transfer. It also reduces the convective heat transfer by reducing the thermal boundary layer edge temperature and decreases the shock stand off distance by about 20%. In 2006, Wright, Hollis, Bose, and Walpot published results using new convective and radiative heating models based on a series of new shock tube experimental data. In this work, the flow field was not coupled with radiation but the coupled effect was estimated using the Tauber-Wakefield expression:

$$q^R_{coup} = q^R_{unc}/(1 + \tilde{\kappa}\Gamma^{0.7}) \tag{1}$$

where q^R_{coup} is the coupled radiative heat flux, q^R_{unc} is the uncoupled radiative heat flux, $\tilde{\kappa}$ is the mixture specific constant which is about 2 for Titan, and Γ is the Goulard number, given by:

$$\Gamma = 2q^R_{unc}/(0.5\rho_\infty V^3_\infty) \tag{2}$$

All the CFD codes mentioned above are structured grid solvers and have similar thermodynamic and chemical models and only differ in the numerical schemes. Although Titan's atmosphere contains complex poly atomic molecules such as CH4, it

has been commonly believed that a two temperature model is sufficient to model all the vibration and electronic modes since N_2 is the strongly dominant species in the atmosphere.

1.3 Domain Decomposition Strategy for Efficient Parallelization

With the fast growth of high performance computing resources, major focus in computational fluid dynamics has been placed on the computation of heavily CPU intensive cases or models which were not able to be attempted ten or twenty years ago. In many cases, these cases are associated with complex flow fields or geometries which bring limitations to the structured grid solvers. Therefore, advancing the unstructured grid solver into a parallel computing environment became an essential task for CFD developers.

For the current research, the deformation of a thin flexible ballute is obtained by several coupling iterations between the flow solver and the structure solver, and this deformation need not be axisymmetric. Therefore it requires a set of full 3D simulations. Each nonequilibrium flow simulation requires additional CPU time than a perfect gas solver. In order to resolve this issue, parallelization of the conducting unstructured grid solver has been performed.

In general, parallel algorithms are categorized into task (or event) decomposition, that identifies tasks that can be executed concurrently and data (or domain) decomposition that identifies local data to each task. Parallelization of a computational fluid dynamics solver is achieved by partitioning the computational domain into several smaller zones and distributing them to different CPUs, then sharing the inter-CPU boundary cell information to update the state vectors of the boundary cells. In this way, parallelization saves the wall clock calculation time by sharing the total CPU time by multiple processors. The two main conditions of parallel computing efficiency are load balancing and grid locality (Grid regions computed by each

processor are compact). Load balancing involves synchronizing the amount of CPU time per iteration between CPUs. Grid locality involves reducing the communication time between CPUs by minimizing the inter-CPU boundary surface area. Satisfying these two conditions are not a challenging task in structured grids solver where the grids are continuously indexed by constant i,j,k lines. However, in contrast to structured grids, unstructured grids need a special consideration to meet these two conditions simultaneously because cell refinement distributions of unstructured grid are random and cell numbers are scattered. Therefore, unstructured grids need a domain decomposition strategy that reorganizes or pre-conditions the spatial data before the execution of parallel computing. In fact, many modern unstructured grid solvers are already parallelized with adequate domain decomposition strategies which are suitable for their grid topologies and solver systems.

Well known NASA developed, tetrahedral based, unstructured grid solvers, FUN3D and USM3D, as well as many other academic unstructured grid solvers, utilize the MeTiS library for mesh partitioning [48] [43] [49] [50]. MeTiS library [10] [51] [52] is a set of serial programs for partitioning graphs, partitioning finite element meshes, and producing fill reducing orderings for sparse matrices. The algorithms implemented in MeTiS are based on the multilevel recursive-bisection, multilevel k-way, and multi-constraint partitioning schemes developed by George Karypis [10] [51] [52] and his colleagues.

The MeTiS library is known as the most efficient available mesh partitioning tool and is general enough to be applied to various type of unstructured graphs. However, if there are ways to construct the spatial data which do not require an iterative partitioning process, the method would be a lot more simplified. Obviously but ironically, structured grids would be the perfect example for this kind of data structure.

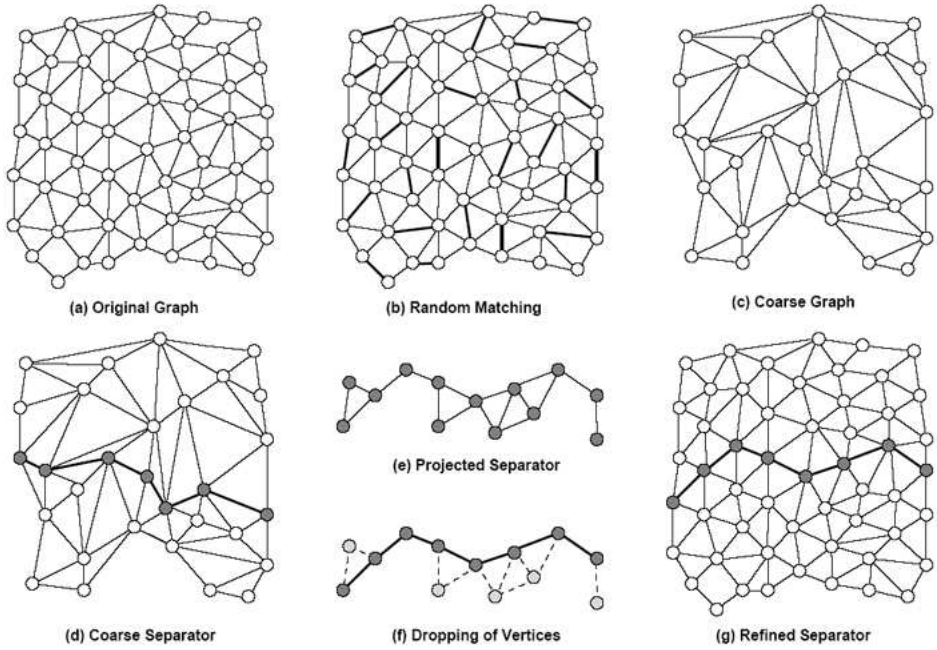

Figure 13: Example of MeTiS Algorithm: The sequence of one level coarsening, finding a separator for the coarse graph, projecting the separator to the original graph, and refining the separator by dropping vertices[10]

In order to achieve this kind of data structure within unstructured grids, researchers from a wide range of disciplines (i.e. image compression [53], vision sensing, ground mapping for GPS, motion picture [54], CAD [55], CFD[56]) recently have adopted the idea of a space-filling curve(SFC).

A SFC is an one dimensional curve that fills every node of a multidimensional space while preserving the nodal locality. Therefore, 2D or 3D spatial data can be stored in a single dimensional array and domain decomposition is easily achieved by chopping this array into even pieces. Also the curve itself can be decomposed into higher refinement levels so it is quite suitable for adaptive grids as shown in the figure 14. SPCs were first described by the Italian mathematician, Giuseppe Peano [57]. A year later David Hilbert [58] published a description of another such curve, perhaps the simplest to describe among all other SFCs. Several other versions were described by other mathematicians, such as Jordan, Morton, and Moore. While the Hilbert and

Morton curves are most suitable for cubic shaped spatial data, the Hilbert curve has been chosen for the present work. It is known that Hilbert outperforms Morton in preserving locality [59] [11] [56] because the Hilbert curves always connect the closest two nodes but Morton does not in some cases.

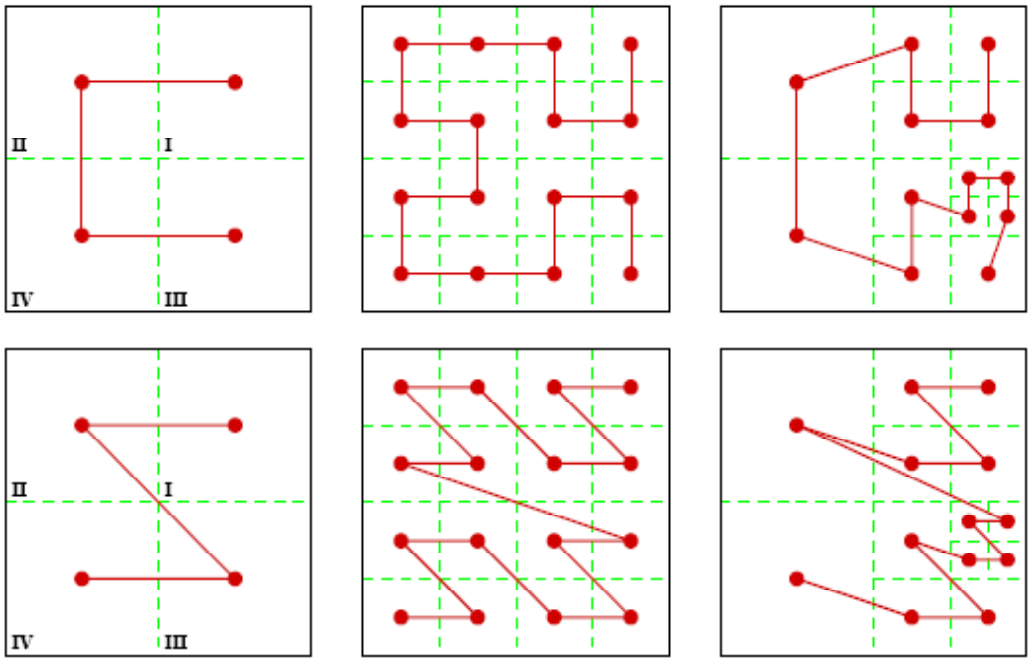

Figure 14: 2D Hilbert(Top) and Morton(Botton) Space Filling Curve[11]

Therefore, grids constructed by the SFC for parallel environment promise short inter-CPU communication time by maintaining cells in contiguous blocks and also it is extremely simple to achieve a good load balancing between CPUs because the SFC arranges the three dimensional data to linear data format.

CHAPTER II

CHEMICAL NON-EQUILIBRIUM FORMULATION

The high flight Mach number associates with the ballute application requires consideration of non-ideal gas effects. These include chemical reactions and excitation of additional thermal energy modes such as vibrational and electronic excitation. In the present chapter, the methodology for predicting chemical non-equilibrium effects is provided, and the next chapter discusses thermochemical nonequilibrium. As is often done, the term chemical nonequilibrium used here refers to inclusion of finite chemical reactions but thermal equilibrium. In a thermal equilibrium state, all energy modes can be described by the Maxwell-Boltzmann distribution. In other words, all the energy modes (translation, rotation, vibration, electronic energy) are described by a single temperature. This model is typically useful for hypersonic flow where the ambient pressure or density is lower than the equilibrium flow regime but higher than the vibrational non-equilibrium flow regime. For example, a chemical nonequilibrium model is usually valid at an altitude of 50km to 90km in the Earth's atmosphere for 30cm radius vehicles. In the altitude of 90km or higher, the thermochemical nonequilibrium model is required. In altitudes lower than 50km, equilibrium solver is usually sufficient. This model requires the species conservation equations in addition to mass, momentum, and energy equations. Also, the thermodynamic properties of the gas mixture are determined in terms of the individual species properties and their creation or destruction. Therefore, temperature dependant thermodynamic properties of each species and their reaction rates with other species are needed for input data.

2.1 Governing Equations

The conservation form of the mass, momentum, energy, and species equations governing an inviscid chemical non-equilibrium flow is

$$\frac{\partial \vec{U}}{\partial t} + \frac{\partial \vec{F}}{\partial x} + \frac{\partial \vec{G}}{\partial y} + \frac{\partial \vec{H}}{\partial z} = \vec{S} \tag{3}$$

where $\vec{U}$ is the conservative state vector, $\vec{F}$,$\vec{G}$,$\vec{H}$ are the flux vectors in cartesian coordinates, and $\vec{S}$ is the source term vector due to chemical reactions.

$$\vec{U} = \begin{pmatrix} \rho^* \\ \rho^* u^* \\ \rho^* v^* \\ \rho^* w^* \\ E_t^* \\ \rho_1^* \\ \vdots \\ \rho_{N_s-1}^* \end{pmatrix}, \quad \vec{F} = \begin{pmatrix} \rho^* u^* \\ \rho^* u^{*2} + P^* \\ \rho^* u^* v^* \\ \rho^* u^* w^* \\ u^*(E_t^* + p^*) \\ \rho_1^* u^* \\ \vdots \\ \rho_{N_s-1}^* u^* \end{pmatrix}, \quad \vec{G} = \begin{pmatrix} \rho^* v^* \\ \rho^* u^* v^* \\ \rho^* v^{*2} + p^* \\ \rho^* v^* w^* \\ v^*(E_t^* + p^*) \\ \rho_1^* v^* \\ \vdots \\ \rho_{N_s-1}^* v^* \end{pmatrix},$$

$$\vec{H} = \begin{pmatrix} \rho^* w^* \\ \rho^* u^* w^* \\ \rho^* v^* w^* \\ \rho^* w^{*2} + P* \\ w^*(E_t^* + p^*) \\ \rho_1^* w^* \\ \vdots \\ \rho_{N_s-1}^* w^* \end{pmatrix}, \quad \vec{S} = \begin{pmatrix} 0 \\ 0 \\ 0 \\ 0 \\ 0 \\ \omega_1^* \\ \vdots \\ \omega_{N_s-1}^* \\ \omega_{ve}^* \end{pmatrix} \tag{4}$$

where the asterisk superscripts denote the non-dimensional value, which will be dropped in the following sections.

2.2 Thermodynamic Models

The conservative total energy is described as

$$E_t = \sum_{i=1}^{N_s} \rho_i \int_0^T c_{vi}(T)dt + \sum_{i=1}^{N_s} \rho_i h_{0i} + \frac{1}{2}\rho(u^2 + v^2 + w^2) \tag{5}$$

where h_{0i} is the heat of formation of the species i at 0K reference temperature. The thermodynamic properties of each species are modeled by empirical results based polynomial curve fits as functions of temperatures. These data sets are taken from reference [5] for air and [60] for all other species. These curve fits are valid in the temperature range of 300 to 30,000K for air and 200 to 20,000K for other species. Other authors [9] [61] have used partition-function based formulations to model simple-harmonic vibrational energies instead of using the polynomial curve fits. These methods are more general and fundamental in the sense that the energies are calculated from quantum mechanics, but less comprehensive in the aspect of neglecting detailed physics in the vibrational and electronic modes. Either method is a reasonable way of representing a thermally perfect gas and it is only a matter of preference while developing a chemical nonequilibrium solver.

Since the specific heat is a function of temperature, it is computed iteratively from equation 5. It usually takes two or three Newton iterations with an initial guessed temperature:

$$T^0 = \frac{E_t - \sum_{i=1}^{N_s} \rho_i h_{0i} - \frac{1}{2}\rho(u^2+v^2+w^2)}{\sum_{i=1}^{N_s} \rho_i c_v(T=298k)} \tag{6}$$

Density and pressure are related to the species partial density by

$$\rho = \sum_{i=1}^{N_s} \rho_i \tag{7}$$

$$P = \sum_{i=1}^{N_s} \rho_i R_i T \tag{8}$$

where $R_i = \frac{\Re}{MW_i}$ is the specific gas constant of species i.

2.3 Chemical Non-Equilibrium

In a hypersonic flow, a huge amount of the bulk kinetic energy of the flow transforms into microscopic random motion of the gas molecules as a form of internal energy when it goes through compression waves. The energized random motion induces

forceful molecular collisions and hence dissociation of diatomic molecules occur. These chemical reactions occur at finite rates. Therefore, a set of species conservation equations has to be solved simultaneously with the flow equation to resolve chemical nonequilibrium effects.

2.3.1 Chemistry Model

The computation of the chemical source term starts with solving the elementary reactions. An elementary reaction is composed of reactants and products,

$$\sum_{i=1}^{N_s} \nu_i^{'} X_i \underset{k_b}{\overset{k_f}{\rightleftharpoons}} \sum_{i=1}^{N_s} \nu_i^{"} X_i \tag{9}$$

where the symbol X_i indicates the species i participating in the reaction, $\nu^{'}$ and $\nu^{"}$ are the stoichiometric coefficients of the reactants and the products respectively and N_s is the total number of species. An elementary reaction can occur in both the forward and backward directions.

$$\text{Forward Rate} \qquad \frac{d[X_i]}{dt} = (\nu_i^{"} - \nu_i^{'}) k_f \prod_i [X_i]^{\nu_i^{'}} \tag{10}$$

$$\text{Backward Rate} \qquad \frac{d[X_i]}{dt} = -(\nu_i^{"} - \nu_i^{'}) k_b \prod_i [X_i]^{\nu_i^{"}} \tag{11}$$

where k_f and k_b denote the forward and backward rate constants respectively. The state where equations 10 and 11 are equal is said to be in chemical equilibrium. In the chemical equilibrium state, the production rate is equal to the destruction rate, hence species concentrations do not change any more. Otherwise, the net rate of production in terms of molar concentration becomes:

$$\frac{d[X_i]}{dt} = (\nu_i^{"} - \nu_i^{'}) \left\{ k_f \prod_i [X_i]^{\nu_i^{'}} - k_b \prod_i [X_i]^{\nu_i^{"}} \right\} \tag{12}$$

The chemical source term in terms of the mass concentration is calculated by collecting all the elementary reactions and multiplying them by the molecular weight

of species i.

$$\omega_i = MW_i \sum_{j=1}^{N_R} (\nu_{i,j}^{"} - \nu_{i,j}^{'}) \left\{ k_{f_j} \prod_i [X_i]^{\nu_{i,j}^{'}} - k_{b_j} \prod_i [X_i]^{\nu_{i,j}^{"}} \right\} \tag{13}$$

The backward reaction rate coefficient k_b is computed from the equilibrium constant K_c.

$$k_b = \frac{k_f}{K_c} \tag{14}$$

where K_c can be computed from the standard state Gibb's free energy per unit mole $\hat{g}_i^{P_{1atm}}$.

$$K_c(T) = exp\left[- \sum_{i=1}^{N_s} \frac{(\nu_i^{"} - \nu_i^{'}) \hat{g}_i(T)}{\Re T} - ln(\frac{\Re T}{P_{1atm}}) \sum_{i=1}^{N_s} (\nu_i^{"} - \nu_i^{'}) \right] \tag{15}$$

$$\hat{g}_i^{P_{1atm}}(T) = \Re T \left[A_1[1 - ln(T)] - \frac{A_2 T}{2} - \frac{A_3 T^2}{6} - \frac{A_4 T^3}{12} - \frac{A_5 T^4}{20} + \frac{A_6}{T} - A_7 \right] \tag{16}$$

where the coefficients in equation 16 are taken from Ref. [5].

2.4 Five Species Air Chemical Kinetics Model

At ambient temperature, air is mostly composed of molecular nitrogen (N_2), molecular oxygen (O_2), and some other minor species such as argon (Ar), carbon dioxide (CO_2), neon (Ne), etc. At high temperatures, products like NO, N, O, O_2^+, N_2^+, NO^+, O^+, N^+, and e^- are produced by thermal dissociation, exchange, and ionization reactions. For the present work, Dunn/Kang [62], Gupta [5], and Park [63] [64] [65] air models are implemented as input data. Table 1 shows the implemented list of elementary reactions and the associated forward reaction rate coefficients in Arrhenius form for the five-species (N_2, O_2, NO, N, O) air model, extracted from the detailed models in the above references. As can be seen from the table, all three models are different. Overall, the Dunn/Kang model is similar to the Gupta model but some reactions are an order of magnitude different. For example, O_2 colliding O_2 dissociation reaction for Dunn/Kang model is ten times faster than that for Gupta. Park's model can not be directly compared to the other two models as it is a totally different temperature

dependent function, but Park's model is usually shown to be more reactive according to current studies. Also, Park's 93 model is more reactive than Park's 87 model, and Park's 87 model is more reactive than Park's 85 model. For applications associated with higher temperature ranges, ionized species such as O_2^+, N_2^+, NO^+, O^+, N^+, and e^- should also be taken into consideration.

Table 1: Five species Air Models: Dunn/Kang, Gupta, Park93

Reaction	Model	Forward Reaction Rate Coefficients ($k_f[cm^3/mole-s]$)
$T_a = T$		
$T_b = (TT_{ve})^{0.5}$		
$O_2 + N \rightarrow 2O + N$	Dunn/Kang	$3.600 \cdot 10^{18} T_a^{-1.00} exp(-5.950e+04/T_a)$
	Gupta	$3.610 \cdot 10^{18} T_b^{-1.00} exp(-5.940e+04/T_b)$
	Park93	$1.000 \cdot 10^{22} T_b^{-1.50} exp(-5.950e+04/T_b)$
$O_2 + NO \rightarrow 2O + NO$	Dunn/Kang	$3.600 \cdot 10^{18} T_a^{-1.00} exp(-5.950e+04/T_a)$
	Gupta	$3.610 \cdot 10^{18} T_b^{-1.00} exp(-5.940e+04/T_b)$
	Park93	$2.000 \cdot 10^{21} T_b^{-1.50} exp(-5.950e+04/T_b)$
$O_2 + O \rightarrow 2O + O$	Dunn/Kang	$9.000 \cdot 10^{19} T_a^{-1.00} exp(-5.950e+04/T_a)$
	Gupta	$3.610 \cdot 10^{19} T_b^{-1.00} exp(-5.940e+04/T_b)$
	Park93	$1.000 \cdot 10^{22} T_b^{-1.50} exp(-5.950e+04/T_b)$
$O_2 + O_2 \rightarrow 2O + O_2$	Dunn/Kang	$3.240 \cdot 10^{19} T_a^{-1.00} exp(-5.950e+04/T_a)$
	Gupta	$3.610 \cdot 10^{18} T_b^{-1.00} exp(-5.940e+04/T_b)$
	Park93	$2.000 \cdot 10^{21} T_b^{-1.50} exp(-5.950e+04/T_b)$
$O_2 + N_2 \rightarrow 2O + N_2$	Dunn/Kang	$7.200e \cdot 10^{18} T_a^{-1.00} exp(-5.950e+04/T_a)$
	Gupta	$3.610e \cdot 10^{18} T_b^{-1.00} exp(-5.940e+04/T_b)$
	Park93	$2.000e \cdot 10^{21} T_b^{-1.50} exp(-5.950e+04/T_b)$
$N_2 + O \rightarrow 2N + O$	Dunn/Kang	$1.900 \cdot 10^{17} T_a^{-0.50} exp(-1.130e+05/T_a)$
	Gupta	$1.920 \cdot 10^{17} T_b^{-0.50} exp(-1.131e+05/T_b)$
	Park93	$3.000 \cdot 10^{22} T_b^{-1.60} exp(-1.132e+05/T_b)$
$N_2 + NO \rightarrow 2N + NO$	Dunn/Kang	$1.900 \cdot 10^{17} T_a^{-0.50} exp(-1.130e+05/T_a)$
	Gupta	$1.920 \cdot 10^{17} T_b^{-0.50} exp(-1.131e+05/T_b)$
	Park93	$7.000 \cdot 10^{21} T_b^{-1.60} exp(-1.132e+05/T_b)$
$N_2 + O_2 \rightarrow 2N + O_2$	Dunn/Kang	$1.900 \cdot 10^{17} T_a^{-0.50} exp(-1.130e+05/T_a)$
	Gupta	$1.920 \cdot 10^{17} T_b^{-0.50} exp(-1.131e+05/T_b)$
	Park93	$7.000 \cdot 10^{21} T_b^{-1.60} exp(-1.132e+05/T_b)$
$N_2 + N \rightarrow 2N + N$	Dunn/Kang	$4.085 \cdot 10^{22} T_a^{-1.50} exp(-1.130e+05/T_a)$
	Gupta	$4.150 \cdot 10^{22} T_b^{-1.50} exp(-1.131e+05/T_b)$
	Park93	$3.000 \cdot 10^{22} T_b^{-1.60} exp(-1.132e+05/T_b)$
$N_2 + N_2 \rightarrow 2N + N_2$	Dunn/Kang	$4.700 \cdot 10^{17} T_a^{-0.50} exp(-1.130e+05/T_a)$
	Gupta	$1.920 \cdot 10^{17} T_b^{-0.50} exp(-1.131e+05/T_b)$
	Park93	$7.000 \cdot 10^{21} T_b^{-1.60} exp(-1.132e+05/T_b)$

Table 1: Cont'd

Reaction	Model	Forward Reaction Rate Coefficients ($k_f[cm^3/mole-s]$)
$NO+O_2 \rightarrow N+O+O_2$	Dunn/Kang	$3.900 \cdot 10^{20} T_a^{-1.50} exp(-7.550e+04/T_a)$
	Gupta	$3.970 \cdot 10^{20} T_b^{-1.50} exp(-7.560e+04/T_b)$
	Park93	$5.000 \cdot 10^{15} T_b^{0.00} exp(-7.550e+04/T_b)$
$NO+N_2 \rightarrow N+O+N_2$	Dunn/Kang	$3.900 \cdot 10^{20} T_a^{-1.50} exp(-7.550e+04/T_a)$
	Gupta	$3.970 \cdot 10^{20} T_b^{-1.50} exp(-7.560e+04/T_b)$
	Park93	$5.000 \cdot 10^{15} T_b^{0.00} exp(-7.550e+04/T_b)$
$NO+O \rightarrow N+O+O$	Dunn/Kang	$7.800 \cdot 10^{20} T_a^{-1.50} exp(-7.550e+04/T_a)$
	Gupta	$3.970 \cdot 10^{20} T_b^{-1.50} exp(-7.560e+04/T_b)$
	Park93	$1.100 \cdot 10^{17} T_b^{0.00} exp(-7.550e+04/T_b)$
$NO+N \rightarrow N+O+N$	Dunn/Kang	$7.800 \cdot 10^{20} T_a^{-1.50} exp(-7.550e+04/T_a)$
	Gupta	$3.970 \cdot 10^{20} T_b^{-1.50} exp(-7.560e+04/T_b)$
	Park93	$1.100 \cdot 10^{17} T_b^{0.00} exp(-7.550e+04/T_b)$
$NO+NO \rightarrow N+O+NO$	Dunn/Kang	$7.800 \cdot 10^{20} T_a^{-1.50} exp(-7.550e+04/T_a)$
	Gupta	$3.970 \cdot 10^{20} T_b^{-1.50} exp(-7.560e+04/T_b)$
	Park93	$1.100 \cdot 10^{17} T_b^{0.00} exp(-7.550e+04/T_b)$
$NO+O \rightarrow O_2+N$	Dunn/Kang	$3.200 \cdot 10^{9} T_a^{1.00} exp(-1.970e+04/T_a)$
	Gupta	$3.180 \cdot 10^{9} T_b^{1.00} exp(-1.970e+04/T_b)$
	Park93	$8.400 \cdot 10^{9} T_a^{1.00} exp(-1.945e+04/T_a)$
$N_2+O \rightarrow NO+N$	Dunn/Kang	$7.000 \cdot 10^{13} T_a^{0.00} exp(-3.800e+04/T_a)$
	Gupta	$6.750 \cdot 10^{13} T_b^{0.00} exp(-3.750e+04/T_b)$
	Park93	$6.400 \cdot 10^{13} T_a^{-1.00} exp(-3.840e+04/T_a)$

2.5 Titan Chemical Kinetics Model

In this work, effort in developing the parallelized unstructured Cartesian grids based nonequilibrium flow solver will be used to perform hypersonic flow analysis on a clamped ballute in the continuum regime of Titan's atmosphere. Titan has a fully developed atmosphere. It's mean atmospheric density is $1.88kg/m^3$, which is about 1.6 times denser than the Earth's. It's atmospheric height is approximately 1,000km thick, which is about ten times that of Earth. Its chemical composition varies widely with altitude. The major species, molecular Nitrogen (N_2), composes approximately 80% to 95% of the atmosphere by volume and the lower altitudes usually have higher concentrations. Methane (CH_4) and Argon (Ar) constitute 10% to 1% and 9% to 2%, respectively. The presence of Methane produces many hydrocarbon radicals, which lead to rapid and complex chemical steps. At high temperatures, products like N, N_2^+, C, C^+, C_2, CH, CH_2, CH_3, H, H^+, H_2, CN, CN^+, NH, and e^- are produced. Especially, the production of the Cyano radical CN generates significantly high radiative emission within the shock layer which can dominate the heat transfer rate at the wall over convective heat transfer. For the present work, the 13 species Nelson 89 model [44] and Gökçen 2004 [66] model are implemented as the input data. As can be seen from Table 2, Gökçen's model is, in general, less sensitive to minor changes in temperature, resulting in more stable numerical calculation during the initial iterations.

Table 2: Nelson-89 and Gökçen-04 Chemical Reaction Rate Constants for Titan Atmosphere

Reaction	Model	Forward Reaction Rate Coefficients ($k_f[cm^3/mole-s]$)
Dissociation Reactions:		
$T_b = (TT_v)^{0.5}$		
$C_2 + M \rightarrow C + C + M$	Nelson	$9.86 \cdot 10^{22} T_b^{-2.0} exp(-71,000/T_b)$
	Gökçen	$1.50 \cdot 10^{16} T_b^{0.00} exp(-71,600/T_b)$
$CH + M \rightarrow C + H + M$	Nelson	$1.13 \cdot 10^{19} T_b^{-1.0} exp(-40,193/T_b)$
	Gökçen	$1.90 \cdot 10^{14} T_b^{0.00} exp(-33,700/T_b)$
$CN + M \rightarrow C + N + M$	Nelson	$1.00 \cdot 10^{23} T_b^{-2.0} exp(-90,000/T_b)$
	Gökçen	$2.53 \cdot 10^{14} T_b^{0.00} exp(-71,000/T_b)$
$CH_4 + M \rightarrow CH_3 + H + M$	Nelson	$2.25 \cdot 10^{27} T_b^{-1.87} exp(-52,900/T_b)$
	Gökçen	$4.70 \cdot 10^{47} T_b^{-8.20} exp(-52,900/T_b)$
$CH_3 + M \rightarrow CH_2 + H + M$	Nelson	$2.25 \cdot 10^{27} T_b^{-1.87} exp(-54,470/T_b)$
	Gökçen	$1.02 \cdot 10^{16} T_b^{0.00} exp(-45,600/T_b)$
$CH_2 + M \rightarrow CH + H + M$	Nelson	$2.25 \cdot 10^{27} T_b^{-1.87} exp(-50,590/T_b)$
	Gökçen	$4.00 \cdot 10^{15} T_b^{0.00} exp(-41,800/T_b)$
$NH + M \rightarrow N + H + M$	Nelson	$1.13 \cdot 10^{19} T_b^{-1.0} exp(-41,820/T_b)$
	Gökçen	$1.80 \cdot 10^{14} T_b^{0.00} exp(-37,600/T_b)$
$H_2 + M \rightarrow H + H + M$	Nelson	$1.47 \cdot 10^{19} T_b^{-1.23} exp(-51,950/T_b)$
	Gökçen	$2.23 \cdot 10^{14} T_b^{0.00} exp(-48,350/T_b)$
$N_2 + N_2 \rightarrow N + N + N_2$	Nelson	$7.0 \cdot 10^{21} T_b^{-1.6} exp(-113,200/T_b)$
	Gökçen	$7.0 \cdot 10^{21} T_b^{-1.6} exp(-113,200/T_b)$
$N_2 + N \rightarrow N + N + N$	Nelson	$3.0 \cdot 10^{22} T_b^{-1.6} exp(-113,200/T_b)$
	Gökçen	$3.0 \cdot 10^{21} T_b^{-1.6} exp(-113,200/T_b)$
Exchange Reactions:		
$T_a = T$		
$C + N_2 \rightarrow CN + N$	Nelson	$1.11 \cdot 10^{14} T_a^{-0.11} exp(-23,000/T_a)$
	Gökçen	$5.24 \cdot 10^{13} T_a^{0.00} exp(-22,600/T_a)$
$CN + C \rightarrow C_2 + N$	Nelson	$3.00 \cdot 10^{14} T_a^{0.0} exp(-18,120/T_a)$
	Gökçen	$5.00 \cdot 10^{14} T_a^{0.00} exp(-13,000/T_a)$
$C_2 + N_2 \rightarrow CN + CN$	Nelson	$7.10 \cdot 10^{13} T_a^{0.0} exp(-5,330/T_a)$
	Gökçen	$1.50 \cdot 10^{13} T_a^{0.0} exp(-21,000/T_a)$
$H + N_2 \rightarrow NH + N$	Nelson	$2.20 \cdot 10^{14} T_a^{0.0} exp(-71,370/T_a)$
	Gökçen	$3.00 \cdot 10^{12} T_a^{0.50} exp(-71,400/T_a)$
$H_2 + C \rightarrow CH + H$	Nelson	$1.80 \cdot 10^{14} T_a^{0.0} exp(-11,490/T_a)$
	Gökçen	$4.00 \cdot 10^{14} T_a^{0.00} exp(-11,700/T_a)$

CHAPTER III

THERMOCHEMICAL NON-EQUILIBRIUM FORMULATION

3.1 Governing Equations

This approach considers nonequilibrium in thermal energy modes with two different temperatures as well as finite rate chemistry. In addition to the chemical non-equilibrium system, the current thermochemical non-equilibrium system contains the combined energy term for vibrational and electronic modes. Therefore, the column vectors in equation 3 are

$$\vec{U} = \begin{pmatrix} \rho^* \\ \rho^* u^* \\ \rho^* v^* \\ \rho^* w^* \\ E_t^* \\ \rho_1^* \\ \vdots \\ \rho_{N_s-1}^* \\ E_{ve}^* \end{pmatrix}, \quad \vec{F} = \begin{pmatrix} \rho^* u^* \\ \rho^* u^{*2} + P^* \\ \rho^* u^* v^* \\ \rho^* u^* w^* \\ u^*(E_t^* + p^*) \\ \rho_1^* u^* \\ \vdots \\ \rho_{N_s-1}^* u^* \\ E_{ve}^* u^* \end{pmatrix}, \quad \vec{G} = \begin{pmatrix} \rho^* v^* \\ \rho^* u^* v^* \\ \rho^* v^{*2} + p^* \\ \rho^* v^* w^* \\ v^*(E_t^* + p^*) \\ \rho_1^* v^* \\ \vdots \\ \rho_{N_s-1}^* v^* \\ E_{ve}^* v^* \end{pmatrix}, \tag{17}$$

$$\vec{H} = \begin{pmatrix} \rho^* w^* \\ \rho^* u^* w^* \\ \rho^* v^* w^* \\ \rho^* w^{*2} + P* \\ w^*(E_t^* + p^*) \\ \rho_1^* w^* \\ \vdots \\ \rho_{N_s-1}^* w^* \\ E_{ve}^* w^* \end{pmatrix}, \quad \vec{S} = \begin{pmatrix} 0 \\ 0 \\ 0 \\ 0 \\ 0 \\ \omega_1^* \\ \vdots \\ \omega_{N_s-1}^* \\ \omega_{ve}^* \end{pmatrix}$$

where the asterisk superscripts denote the non-dimensional value, which will be dropped in the following sections.

3.2 Thermodynamic Models

The conservative total energy for a two-temperature model is described as

$$E_t(T, T_{ve}) = \sum_{i=1}^{N_s} \rho_i[(c_{vi})_{tr} + (c_{vi})_{rot}]T + \sum_{i=1}^{N_s} \rho_i h_{0i} + E_{ve}(T_{ve}) + \frac{1}{2}\rho(u^2 + v^2 + w^2) \quad (18)$$

where $(c_{vi})_{tr} and (c_{vi})_{rot}$ are the specific heats of fully excited translational and rotational modes respectively, T is the translational-rotational temperature, and T_{ve} is the vibrational-electronic temperature. The vibrational-electronic energy for the two-temperature model can be evaluated by subtracting the calorically linear translational-rotational modes and the heat of formation.

$$E_{ve} = \sum_{i=1}^{N_s} \rho_i (e_i)_{ve} \quad (19)$$

$$e_{ve}(T_{ve}) = e(T_{ve}) - (c_{v,tr} + c_{v,rot})T_{ve} - h_{0i} \quad (20)$$

Here, the internal energy $e(T_{ve})$ is described by a semi-empirical polynomial curve fit for thermodynamic properties for a function of vibrational-electronic temperature from reference [5] for air and [60] for other species.

In the thermal nonequilibrium model, the choice of reaction temperature becomes somewhat ambiguous due to the presence of more than one temperature. The chemical reaction rates, in general, are functions of collision frequency and the Boltzmann factor which gives the fraction of collisions above the activation energy. Although the collision frequency is only related to the translational temperature, it is known that highly vibrating molecules are more likely to dissociate. Therefore, Park [67] suggested the geometric average temperature for dissociating reactions.

$$T_d = \sqrt{T T_{ve}} \quad (21)$$

This reaction temperature model is assumed based on agreement with empirical results without any theoretical justification. However, this relation has been widely accepted and has produced many validated results.

Unlike chemical nonequilibrium, since the vibrational-electronic energy is computed as a conservative variable, the translational-rotational temperature can be computed directly from equation (18). The vibrational-electronic temperature is computed within two or three Newton iterations with an initially guessed vibrational temperature:

$$T_{ve}^{0} = \frac{\overline{\theta}_V}{ln[1 + (\overline{\theta}/E_v)\sum_{j=1}^{N_{sp}} \rho_j R_j]} \tag{22}$$

$$\overline{\theta}_V = \frac{\sum_{j=1}^{N_{sp}} \rho_j \theta_{vj}}{\sum_{j=1}^{N_{sp}} \rho_j} \tag{23}$$

where N_{sp} denotes the number of polyatomic species j.

3.2.1 Vibrational Source Term

The vibrational-electronic source term ω_{ve} in equation 17 is computed as

$$\omega_{ve} = \sum_{j=1}^{N_{sp}} \omega_{ve_j} \tag{24}$$

$$\omega_{ve_j} = \frac{E_{ve_j}(T) - E_{ve_j}(T_{ve})}{\tau_j} + \frac{\omega_j}{\rho_j} E_{ve_j}(T_{ve}) \tag{25}$$

where the second term on the RHS in equation (25) is the rate of vibrational energy production due to the creation and destruction of polyatomic species by chemical reactions.

The vibrational relaxation time τ_j is calculated using the molar averaged correlation developed by Millikan and White [68], which is based principally on the Landau-Teller model [69] [31]. This semi-empirical correlation between empirical vibrational relaxation times and the relevant molecular constants leads to estimating

the rates that are not measured yet. It is valid within a temperature range of 300 to 8000K. The correlation is expressed as

$$\tau_j^{MW} = \frac{\sum_{i=1}^{N_{sp}} X_i}{\sum_{i=1}^{N_{sp}} X_i/\tau_{i,j}} \tag{26}$$

$$\tau_{i,j} = \frac{exp[A_{i,j}(T^{-1/3} - 0.015\mu_{i,j}^{1/4}) - 18.42]}{p/101325} \tag{27}$$

$$A_{i,j} = 1.16E - 3\mu_{i,j}^{1/2}\theta_j^{4/3} \tag{28}$$

$$\mu_{i,j} = \frac{MW_i MW_j}{MW_i + MW_j} \tag{29}$$

For temperatures above 8000K, Park's [70] high temperature correction is adopted as

$$\tau_j^P = (\sigma_j \bar{c}_j n_j) \tag{30}$$

where n_j is the number density of species j, $\bar{c}_j$ is the average molecular velocity of species j, and σ_j is the effective cross-section. $\bar{c}_j$ and σ_j are respectively computed using

$$\bar{c}_j = \left(\frac{8kT}{\pi MW_j}\right) \tag{31}$$

$$\sigma_j = 10^{21}\left(\frac{50,000}{T^2}\right) \tag{32}$$

The above effective cross-section value is approximately taken from that originally developed from nitrogen. Therefore, the total relaxation time contributed by both τ_j^{MW} and τ_j^P is defined as

$$\tau_j = \tau_j^{MW} + \tau_j^P \tag{33}$$

Park's [67] second correction for higher temperatures suggests that the vibrational relaxation process obeys somewhat similarly to the diffusion equation with respect

to the vibrational energy level, rather than a linearly varying Landau-Teller model. Therefore, Park correlated the relaxation time with respect to the translational temperature and vibrational temperature at the shock wave, which is upstream of the computing point where the relaxation process is initiated. Therefore, the corrected vibrational source term is modified to

$$\omega_{ve_j} = \frac{E_{ve_j}(T) - E_{ve_j}(T_{ve})}{\tau_j} \left| \frac{T_{shock} - T_{ve}}{T_{shock} - T_{ve,shock}} \right|^{s-1} + \frac{\omega_j}{\rho_j} E_{ve_j}(T_{ve}) \tag{34}$$

where

$$s = 3.5exp\left(-5,000/T_{shock}\right) \tag{35}$$

In two or three dimensional flows, it is technically very difficult to trace the true upstream value. And it becomes even more difficult in unstructured grid solvers. Therefore, the values for T_{shock} and $T_{ve,shock}$ are usually approximated within a reasonable limit of the model. In the present work, these values are taken from the upstream shock wave of a stagnation point.

CHAPTER IV

NUMERICAL METHOD

4.1 Numerical Scheme

4.1.1 AUSMPW+ Scheme

Hypersonic flow generally introduces a strong shock wave, leading to extremely large gradients in the flow properties. In this stiff gradient region, even very small non-physical oscillations in the initial solution can lead to negative temperatures or pressures. During the initial stage of the present research, minor oscillatory behavior was observed with the Roe's approximated Riemann scheme in the regime where the Mach number is higher than 15. In order to avoid such non-physical oscillation, AUSMPW+ scheme[71] [72] was chosen for the inviscid flux calculation. Also according to the preceding researches, AUSMPW+ scheme has been known to be more stable and at the same time less dissipative in hypersonic flows than the Roe's scheme. AUSMPW+ scheme is a modified version of the AUSM(Advection Upstream Splitting Method) family schemes. In the present work, an AUSMPW+ scheme adapted for chemical reacting flows was incorporated into a Cartesian grid solver. Improved stability relative to Roe's scheme was observed. The scheme employed in this work is described below.

The AUSM concept is to use different splittings for the convective fluxes, with each splitting being some function of an intuitively defined interface Mach number. AUSMPW scheme with pressure based weight function was introduced to overcome the carbuncle phenomenon and the overshoot problems behind a strong shock in AUSM [73] or AUSMD [74] scheme. AUSMPW+ scheme is a more improved and simplified version of AUSMPW scheme [75] by introducing a new numerical speed of

sound. The numerical flux of the AUSMPW+ at a given cell interface is given by:

$$F_{\frac{1}{2}} = \bar{M}_L^+ c_{\frac{1}{2}}[\Phi_L] + \bar{M}_R^- c_{\frac{1}{2}}[\Phi_R] + (P_L^+|_\alpha[P_L] + P_R^-|_\alpha[P_R]) \tag{36}$$

where $[\Phi] = (\rho, \rho u, \rho v, \rho w, \rho h_t, \rho_i, \ldots, \rho_{N_s-1})^T$ and $[P] = (0, p, 0, 0, 0, 0, \ldots, 0)$ for the x-direction. The subscripts 1/2, L and R stand for the value at the cell interface, left, and right across the cell interface, respectively. where

$$for \quad m_{1/2} \geq 0, \begin{cases} \bar{M}_L^+ = M_L^+ + M_R^-[(1-\omega_p)(1+f_R) - f_L], \\ \bar{M}_R^- = M_R^- \omega_p (1+f_R), \end{cases} \tag{37}$$

$$for \quad m_{1/2} \leq 0, \begin{cases} \bar{M}_L^+ = M_L^+ \omega_p (1+f_L), \\ \bar{M}_R^- = M_R^- + M_L^+[(1-\omega_p)(1+f_L) - f_R], \end{cases} \tag{38}$$

with

$$\omega_p(p_L, p_r) = 1 - min(\frac{p_L}{p_R}, \frac{p_R}{p_L})^3 \tag{39}$$

And $f_{L,R}$ is simplified to

$$f_{L,R} = 1 \begin{cases} (\frac{p_{L,R}}{p_s} - 1) min(1, \frac{min(p1_L, p1_R, p2_L, p2_R)}{min(p_L, p_R)})^2, p_s \neq 0, \\ 0, elsewhere, \end{cases} \tag{40}$$

The split Mach number and the pressure splitting function for the ASUMPW+ scheme across cell interfaces are given as:

$$M^\pm = \begin{cases} \pm\frac{1}{4}(M \pm 1)^2, & |M| \leq 1, \\ \frac{1}{2}(M \pm |M|), & |M| > 1, \end{cases} \tag{41}$$

$$P^\pm|_\alpha = \begin{cases} \frac{1}{4}(M \pm 1)^2(2 \mp M) \pm \alpha M(M^2-1)^2, & |M| \leq 1, \\ \frac{1}{2}(1 \pm sign(M)), & |M| > 1, \end{cases} \tag{42}$$

where α ranges from 0 to 3/16. When $\alpha = 0$, then the scheme becomes more stable since the pressure splitting function becomes more diffusive. When $\alpha = 3/16$, then

the scheme becomes more accurate. The Mach number on each side is:

$$M_{L,R} = \frac{U_{L,R}}{c_{\frac{1}{2}}} \tag{43}$$

The critical speed of sound at the cell interface in equation 43 has been carefully chosen by the following expressions.

$$c_{\frac{1}{2}} = \begin{cases} \frac{c_s^2}{max(|u_L|,c_s)}, \ if \ \frac{1}{2}(u_L + u_R) > 0 \\ \frac{c_s^2}{max(|u_R|,c_s)}, \ if \ \frac{1}{2}(u_L + u_R) < 0 \end{cases} \tag{44}$$

$$c_s = \left(2H_{normal} \frac{(\widetilde{\gamma}_L - 1)/(\widetilde{\gamma}_L u_R) - (\widetilde{\gamma}_R - 1)/(\widetilde{\gamma}_R u_L)}{(\widetilde{\gamma}_R + 1)/(\widetilde{\gamma}_R u_R) - (\widetilde{\gamma}_L + 1)/(\widetilde{\gamma}_L u_R)} \right)^{0.5} \tag{45}$$

where $\widetilde{\gamma}$, left and right of a cell interface, are

$$\text{For Chemical Non-equilibrium, } \widetilde{\gamma} = \frac{\sum_{i=1}^{N_s} c_i c_p(t)_i}{\sum_{i=1}^{N_s} c_i c_v(t)_i}. \tag{46}$$

$$\text{For Thermochemical Non-equilibrium, } \widetilde{\gamma} = 1 + \frac{P}{\rho e}. \tag{47}$$

Here, it should be pointed out that the ratio of the specific heat capacities for chemical nonequilibrium is modeled based on the frozen specific heats at a given composition and temperature. This expression, in Equation 46, is not appropriate in thermal nonequilibrium because the specific heats are no longer only functions of translational temperature. Therefore, the ratio of specific heats for thermochemical nonequilibrium is modeled as equation 47.

The H_{normal} is the averaged sensible total enthalpy that includes the normal component of kinetic energy.

$$H_{normal} = 0.5 \cdot (h_{sensible,L} + \frac{1}{2}u_L^2 + h_{sensible,R} + \frac{1}{2}u_R^2) \tag{48}$$

4.1.2 Point Implicit Method

In chemically reacting flows, chemical characteristic times can be an order of magnitude smaller than the flow characteristic times. Therefore, an explicit treatment

of the source term, in general, produces a stiffness problem if the time step is taken based on the flow time. In order to avoid such CFL constraints, the chemical source term is computed by a point implicit manner incurring an expense of a $N_s \times N_s$ matrix inversion for each cell, while everything else is computed in an explicit manner. In the present work, a direct method is adopted for the matrix inversion because the number of species is relatively small. However, the cost of matrix inversion with a direct method increases with order of N_s^3. So if a large number of species is computed, then iterative methods for matrix inversion or even explicit methods with proper relaxation models are recommended.

Consider the set of species conservation equations discretized for a grid cell of volume V, noting $\mathbf{R}$ as the summation of the species fluxes:

$$\frac{\partial[\vec{U}]}{\partial t}V + \mathbf{R}(\vec{U}^n) = \vec{\omega}^{n+1}V \tag{49}$$

Using a Taylor expansion of the source term:

$$\vec{\omega}^{n+1} \approx \ \vec{\omega}^n + \frac{\partial\vec{\omega}^n}{\partial[\vec{U}^n]}\frac{d\vec{U}}{dt}\Delta t \tag{50}$$

where $\frac{\partial\vec{\omega}^n}{\partial[\vec{U}]}$ term for each species is expressed as:

$$\frac{\partial\omega_i^n}{\partial U_i^n} = \frac{MW_i}{\rho_i^n}\sum_{j=1}^{N_R}(\nu_{i,j}^{"} - \nu_{i,j}^{'})\left\{k_{f_j}\nu_{i,j}^{'}\prod_i[X_i^n]^{\nu_{i,j}^{'}} - k_{b_j}\nu_{i,j}^{"}\prod_i[X_i^n]^{\nu_{i,j}^{"}}\right\} \tag{51}$$

Substituting equation 49 into equation 50 yields the following equation:

$$\frac{d\vec{U}}{dt}V + \mathbf{R}(\vec{U}^n) = \vec{\omega}^n V + \frac{\partial\vec{\omega}^n}{\partial[\vec{U}^n]}\frac{d\vec{U}}{dt}\Delta t V \tag{52}$$

Rearranging equation 52 into a matrix form:

$$\left[I - \Delta t\frac{\partial\vec{\omega}^n}{\partial[\vec{U}]}\right]\frac{d[\vec{U}]}{dt}V + \mathbf{R}(\vec{U}^n) = \vec{\omega}^n V \tag{53}$$

By inverting the matrix by LU decomposition in equation 53 and by multiplying it to both sides, the final equation is described as:

$$\frac{d[\vec{U}]}{dt}V = \left[I - \Delta t\frac{\partial\vec{\omega}^n}{\partial\vec{U}^n}\right]^{-1}[\vec{\omega}^n V - \mathbf{R}(\vec{U}^n)] \tag{54}$$

Remarks: This method is slightly different from the preceding work done by Tu [9] and Yahia [61] in the sense that the flux terms are also treated point implicitly. The currently method is mathematically consistent with the first order Taylor expansion.

4.1.3 MUSCL Data Reconstruction

In the present work, MUSCL (Monotone Upstream-Centered Scheme for Conservation Laws) data reconstruction is plugged into the AUSMPW+ scheme. The idea behind the MUSCL approach, developed by Van Leer, was to linearly reconstruct piece-wise spatial data instead of a constant reconstruction used in the Gudunov scheme. The expression for the right and left interpolations in general grid spacing are:

$$\begin{aligned} W_{L_{i+1/2},j,k} &= W_{i,j,k} + \frac{\varepsilon_{i,j,k}\Delta x_{i,j,k}}{2} \\ &\quad \left[(1-k)\frac{W_{i,j,k}-W_{i-1,j,k}}{\Delta x_{i,j,k}+\Delta x_{i-1,j,k}} + (1+k)\frac{W_{i+1,j,k}-W_{i,j,k}}{\Delta x_{i+1,j,k}+\Delta x_{i,j,k}}\right] \\ W_{R_{i+1/2},j,k} &= W_{i+1,j,k} - \frac{\varepsilon_{i,j,k}\Delta x_{i+1,j,k}}{2} \\ &\quad \left[(1+k)\frac{W_{i+1,j,k}-W_{i,j,k}}{\Delta x_{i+1,j,k}+\Delta x_{i,j,k}} + (1-k)\frac{W_{i+2,j,k}-W_{i+1,j,k}}{\Delta x_{i+2,j,k}+\Delta x_{i+1,j,k}}\right] \end{aligned} \tag{55}$$

where

$$W = \begin{bmatrix} \rho \\ u \\ v \\ w \\ H \\ c_i \\ \vdots \\ c_{N_s-1} \\ e_{ve} \end{bmatrix} \tag{56}$$

In the early stage of this work, translational temperature and vibrational temperature were used as the state variables for the computation of total energy and vibrational energy. The computation of translational temperature takes an iterative process in the chemical nonequilibrium formulation, and that of vibrational temperature takes an iterative process in the thermochemical nonequilibrium formulation. These iterative processes take up significant amount of CPU time. Therefore, H and e_{ve} are used for the current work.

The different choices of $\varepsilon_{i,j,k}$ and κ for the MUSCL interpolation yields various choices of spatial order of accuracies and types. The following table shows different types of inviscid flux schemes with the corresponding values of $\varepsilon_{i,j,k}$ and κ.

Table 3: Types of inviscid flux schemes by $\varepsilon_{i,j,k}$ and κ

ϵ	κ	Types of Inviscid Flux Scheme
$\varepsilon_{i,j,k}$=0.0	κ=N/A	First Order Accurate Inviscid Fluxes
$\varepsilon_{i,j,k}$=1.0	κ=-1.0	Second Order Fully Upwind Inviscid Fluxes
$\varepsilon_{i,j,k}$=1.0	κ=0.0	Third Order Upwind Biased Inviscid Fluxes
$\varepsilon_{i,j,k}$=1.0	κ=1/3	Third Order Upwind Biased Inviscid Fluxes
$\varepsilon_{i,j,k}$=1.0	κ=1.0	Second Order Centrally-Differenced Inviscid Fluxes

4.1.4 Grid Refinement Based on Solution Adaption

The solution adaption methodology based on velocity divergence, discussed by Tu [9] and Marshall [26], provides adequate grid refinement along the shock waves and in rapid expansion regions, where the velocity divergence is scaled by a characteristic length of the control volume to obtain a measure of the changing flow properties from one cell to another.

$$\tau_d = |\nabla \cdot \vec{V}| \, l^{3/2} \tag{57}$$

where l is the cube-root of the cell volume and the power $\frac{3}{2}$ is to ensure that the adaption criteria's sensitivity diminishes with increasing refinement.

In this work, it was found that adaption to velocity divergence alone sometimes, but not always, caused stability problems for reacting flow cases. The problems were caused during the early stages of solution adaption, when unrefined Cartesian cells induced step-like shock structures, as shown on the left in Figure 15. Such non-physical shock shapes could result in excessive dissociation of chemical species or create energy imbalances between surrounding cells. These kinds of problems, during the intermediate calculations, sometimes cause instabilities, that could lead to solution divergence.

Therefore, in the present, the solution adaption methodology based on velocity divergence has been expanded to species concentration gradients, in order to avoid the instability problem and also increase the accuracy of solution in the downstream region of the shock, where the finite-rate chemical reactions happen. The validity of the numerical simulation of chemical nonequilibrium flows depends critically on species concentrations at a given state, which govern the energy transfer between chemistry and other internal energy modes. Therefore, resolving composition gradients along the flow streamline is necessary to obtain accurate flow solutions. The stable and accurate solution obtained from species based solution adaption is shown on the right in Figure 15. Figure 16 shows the evidence of grid adaption based on species gradient.

The formulation for the species gradient solution adaption is described as:

$$\tau_c = \underset{i}{\overset{N_s}{Max}} |\nabla c_i| \; l^{3/2} \tag{58}$$

where c_i and N_s are the mass concentration of species i and the total number of species, respectively.

The local species gradient τ_c is then compared to the root mean square value of the species gradient of the entire set of computational cells, σ_c.

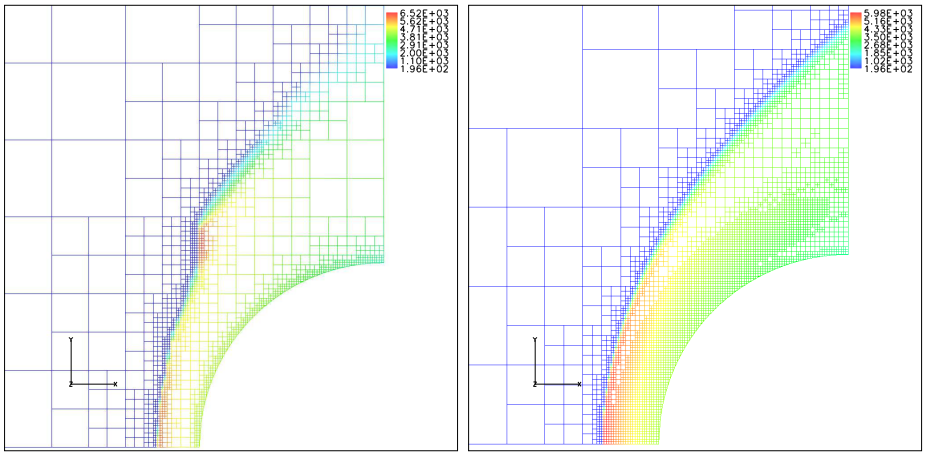

Figure 15: Temperature contours of step-like shock formation during early stage of solution adaption(Left) vs. Enhanced solution with species gradient based solution adaption(Right)

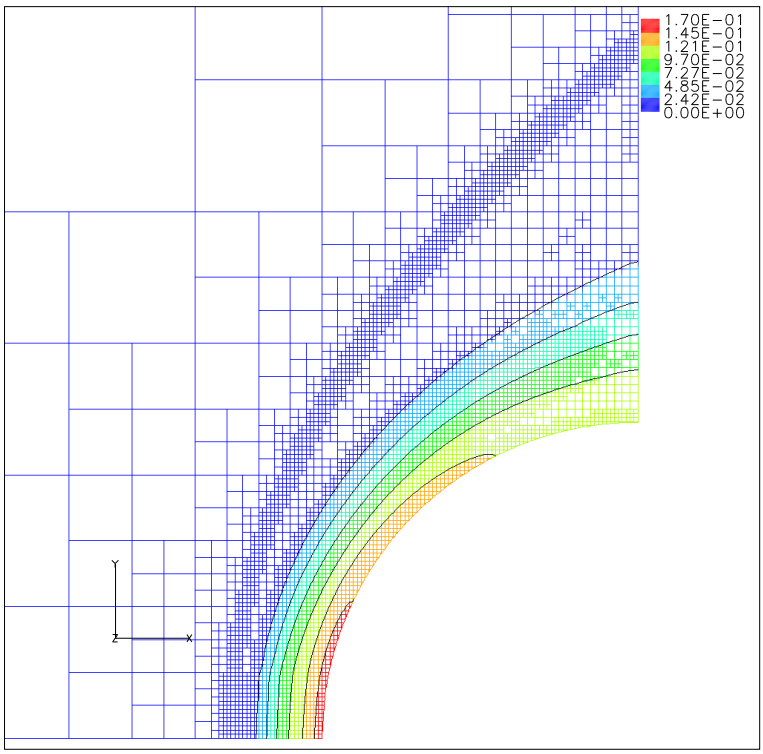

Figure 16: Velocity divergence and Species gradient based grid adaption and Molar concentration of Oxygen atom contour lines

$$\sigma_c = \sqrt{\frac{1}{N}\sum_{n=1}^{N}\tau_c^2} \tag{59}$$

where N is the total number of computational cells. Finally cells are flagged for refinement and coarsening with adaption parameters $\alpha_{c,min}$ and $\alpha_{c,max}$.

$$\begin{cases} \text{Refine}, & \text{if } \tau_c > \alpha_{c,min} \\ \text{Coarsen}, & \text{if } \tau_c < \alpha_{c,max} \end{cases} \tag{60}$$

Although the selection of the adaption criteria can be different for different cases, based on sensitivity tests for the adaption parameters, $\alpha_{c,min} = 0.1$ and $\alpha_{c,max} = 1.0$ are recommended to adapt most of the cells inside the shock layer and $\alpha_{c,min} = 0.4$ and $\alpha_{c,max} = 1.0$ are recommended to adapt all the cells near the stagnation region.

4.1.5 Efficiency of the solver

The presented numerical methods were implemented to an existing unstructured Cartesian grid flow solver, NASCART-GT, by adding thermochemical nonequilibrium capability to the perfect gas solver. The amount of CPU time per iteration per cell while running NASCART-GT in the perfect gas mode is about $35\mu sec$ in a modern Pentium-4 3.0Ghz machine. The code requires additional CPU time to run in chemically reacting nonequilibrium mode and this depends on the number of species and complexity of the reaction steps. For two-temperature, five-species air model with 17 reaction steps, the amount of CPU time per iteration per cell is approximately $117\mu sec$. This increase in the CPU time per iteration per cell is attributed to the computation of the following addition terms:

1. Species fluxes and source terms
2. Vibrational energy fluxes and source term

3. Representation of total energy by summation individual species

4. Iterative processes for primitive variables (Temperature for chemical nonequilibrium, Vibrational-electronic temperature for thermochemical nonequilibrium)

The CPU time per iteration per cell required by a structured grid nonequilibrium solver (DPLR) for the same two-temperature, five-species air model with 17 reaction steps is $46\mu sec$. Unstructured grid solvers generally take a considerable amount of additional CPU time when compared to structured grid solvers because of the need to manage extra memory and also in arranging numerical stencils by interpolations. However, this drawback of unstructured grid solvers is dwarfed by the significant reduction in the man-hours that would be required otherwise in generating a structured grid around complex geometries.

CHAPTER V

REACTING GAS VALIDATION RESULTS

5.1 Chemical Non-Equilibrium Results

A test case for hypersonic flow around a circular cylinder(R=0.5m) was numerically calculated to validate the present chemical nonequilibrium solver. The freestream Mach number, angle of attack, temperature and density were $M_\infty = 12.2, \alpha = 0, T_\infty = 266K, P_\infty = 43Pa, \rho_\infty = 5.6227E-4kg/m^3$, respectively. The concentrations of N_2 and O_2 were assumed to be 79% and 21% by volume respectively. The total number of flow cells was 9832 and solution adaption was performed after every 100 iterations based on velocity divergence and species gradients. The top grid shown in Figure 21 confirm good solution adaption along the shock wave and the species gradients in the post shock region.

Figures 17, 18, and 19 show the distribution of temperature, density, and pressure respectably, along the stagnation stream line. The results indicate that the ASUMPW+ scheme with MUSCL data reconstruction resolves the stiff gradients across the shock without any oscillation and shows promising agreement with the validation data. The overshoot shown in the temperature plot is due to the nonequilibrium effect between the translation temperature and the finite rate chemical reactions. For comparison, the calorically perfect gas results from NASCART-GT are also shown in the same figures. The nonequilibrium results predict, as expected, a smaller shock stand-off distance, higher density, and lower temperature than for the calorically perfect gas. The pressure difference between the calorically perfect gas and the chemically reacting thermally perfect gas is supposed be to very small across a normal shock. However, they will be very different across an oblique shock because

the shock angles are quite different due to the dominating density effects. Figure 20 shows the chemical composition along the stagnation streamline. As can be seen, N_2 and O_2 begin to dissociate right behind the shock wave and the unstable N atoms immediately react with the O atoms to form NO. The activation energy of O_2 is much lower than that of N_2. Therefore, not only is nearly 90% of O_2 dissociated, but it also absorbs so much of the internal energy of the gas that the backward rate of N_2 dissociation becomes more dominant after $X = -0.08$.

This case has been compared to DPLR's(NASA Ames' structured grid code) and also with data taken from Barbante's thesis [76]. They are both inviscid calculations and use the 5-species Air model. The reaction rate constant used in Barbante's thesis is unknown, and Park's 1990 model has been used in DPLR. Park's 1990 model is identical to Park's 1993 model in terms of the non-ionized species and ionization is not considered in this validation test. The stagnation line data taken from Barbante's and DPLR are compared in Figures 17 to 20. The figures indicate that Barbante's method predicts slightly higher temperature and lower density when compared to the current and DPLR's results. This is because Barbante used a partition function to calculate the equilibrium vibrational temperature, and DPLR uses the NASA Lewis thermodynamic curvefit to model it similar to the present approach. Figures 22 to 29 show the contour plots of the flow properties over a 2D cylinder in comparison to DPLR. The plot on the top in each figure is the result from the present work, and the ones below are the results from DPLR. For DPLR, 60 x 40 grids were generated using GRIDGEN software. As can be seen from the figures, the results from the present work, in overall, compare well with the DPLR results. Since the current work uses Cartesian grids, which inherently can not offer shock aligned cell faces, there are some step-like gradient profiles at the shock front. The slight discrepancies in chemical compositions near the mid shock layer region are observed in Figures 26 and 29. The present solver predicts a higher dissociation of O_2 molecules and lesser

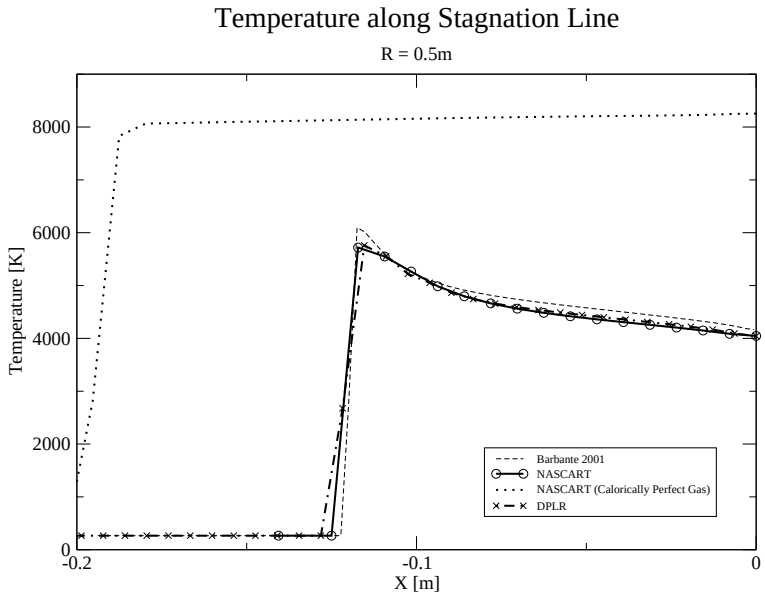

Figure 17: Temperature Distribution along Stagnation Line

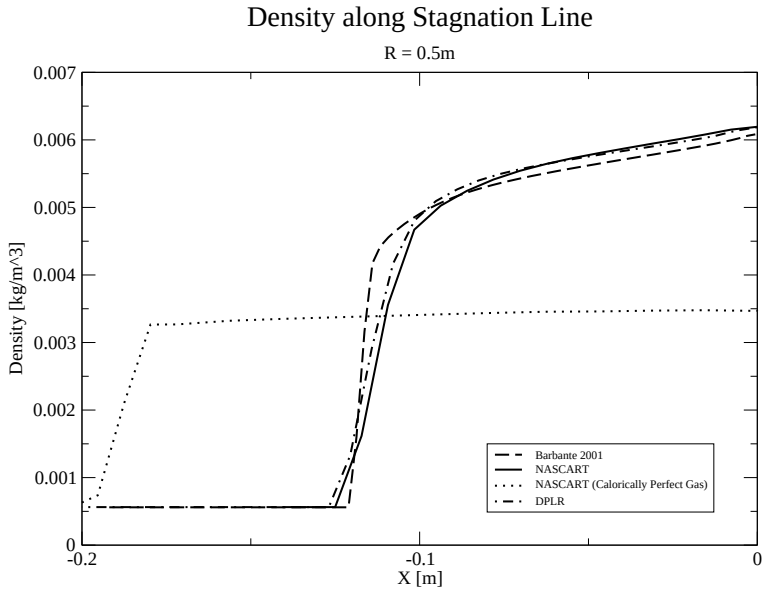

Figure 18: Density Distribution along Stagnation Line

dissociation of N_2 molecules when compared to DPLR in this region. This results in a more smeared out distribution of the high NO concentration band as shown in Figure 27.

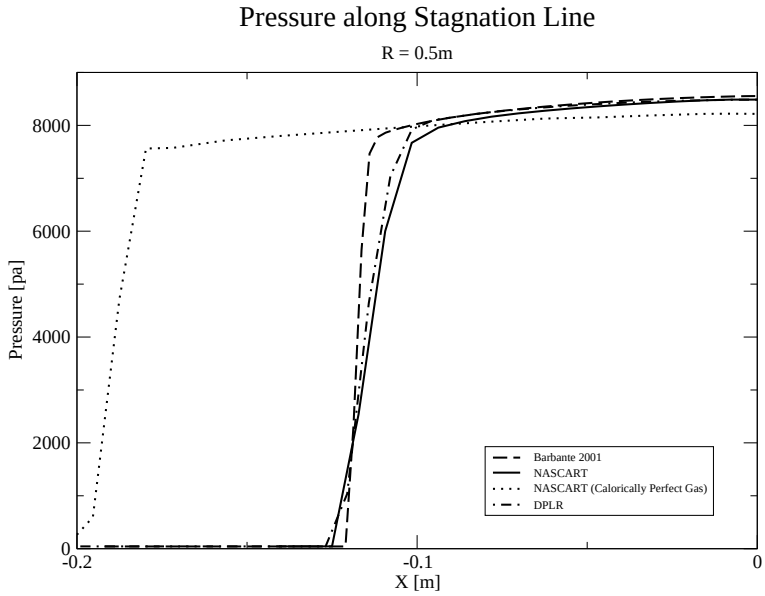

Figure 19: Pressure Distribution along Stagnation Line

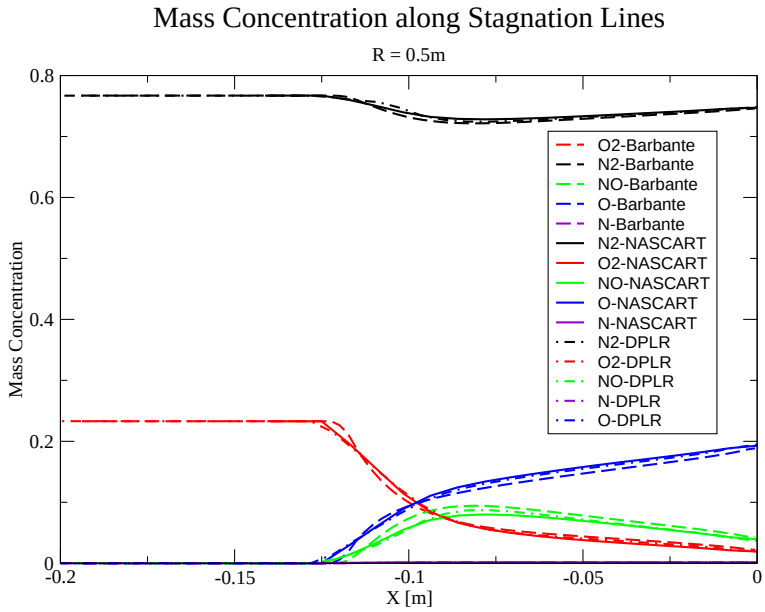

Figure 20: Mass Concentration Distribution along Stagnation Line

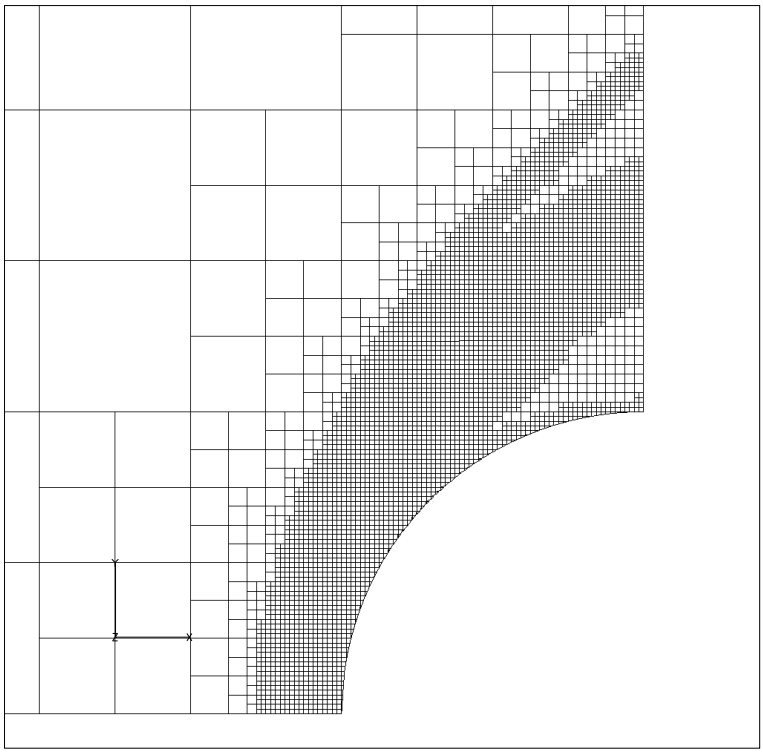

(a) NASCART-GT

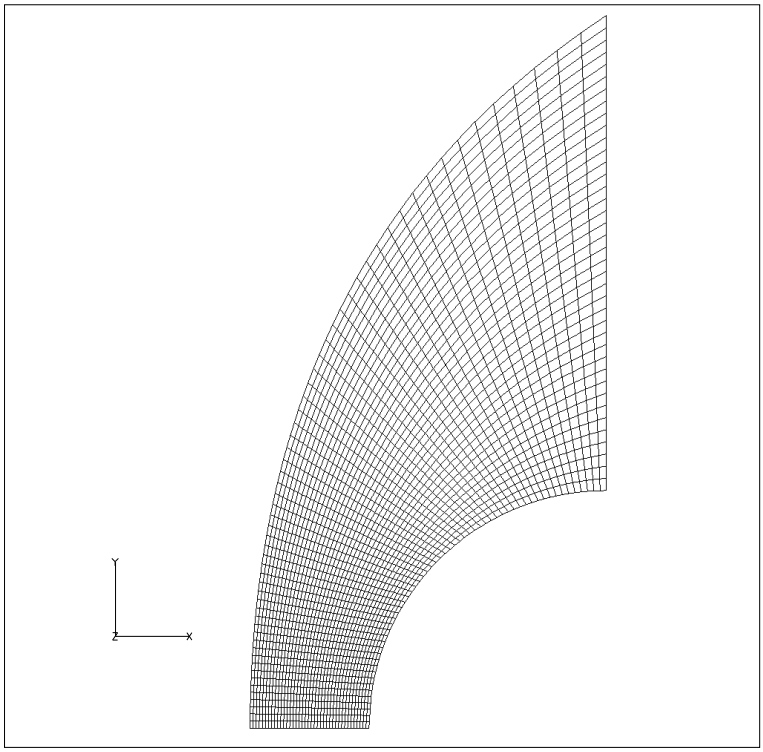

(b) DPLR

Figure 21: Grid over 0.5m Cylinder

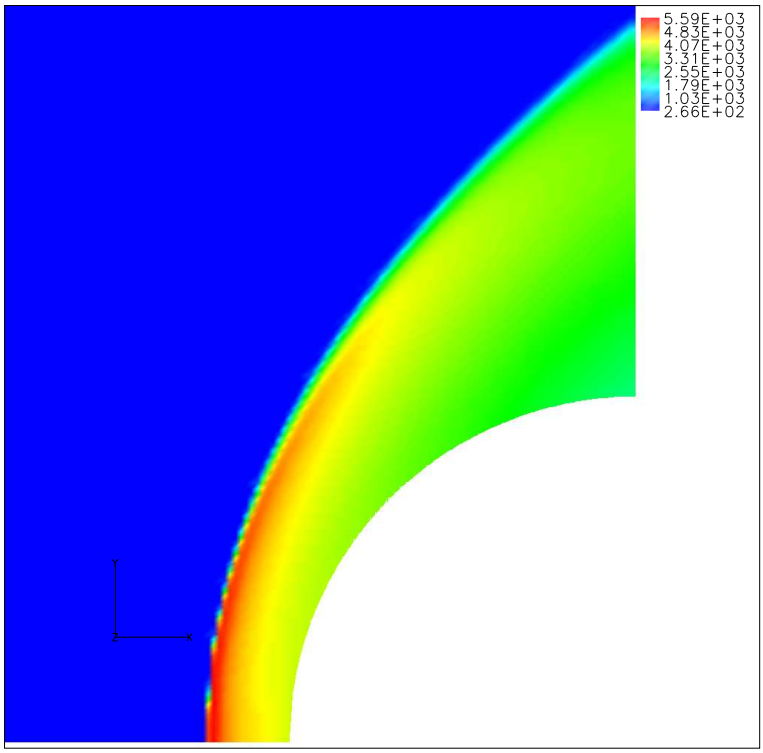

(a) NASCART-GT

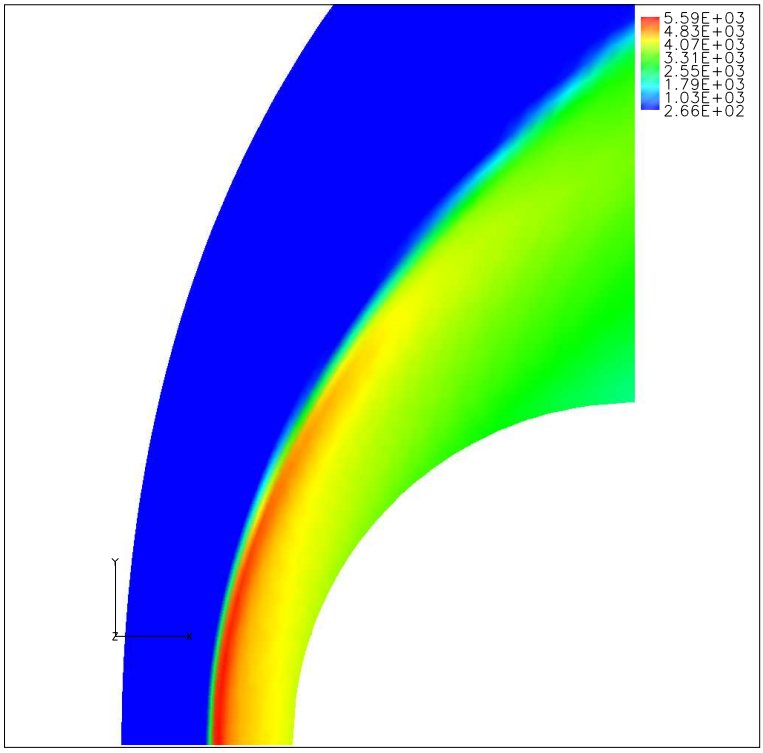

(b) DPLR

Figure 22: Temperature Contours

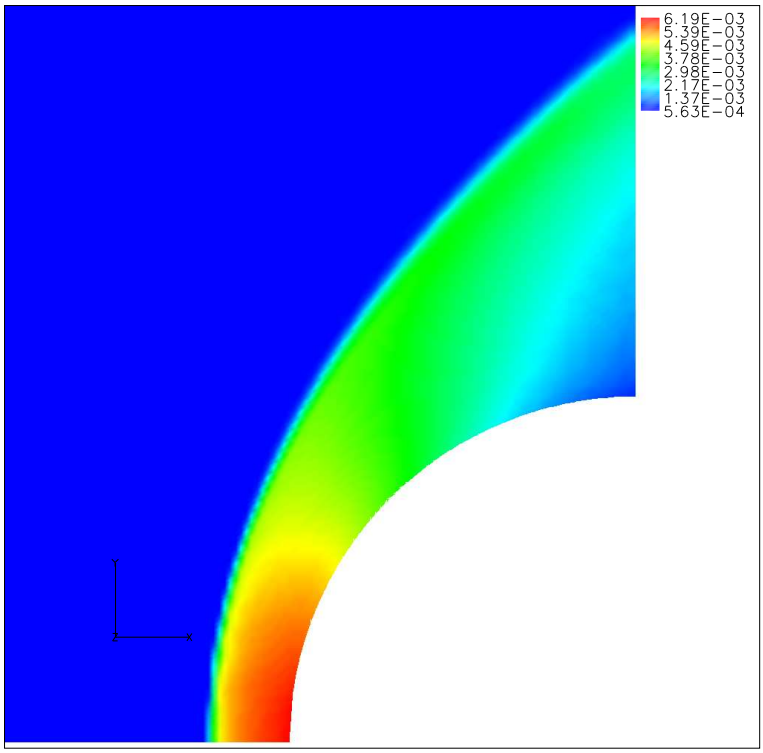

(a) NASCART-GT

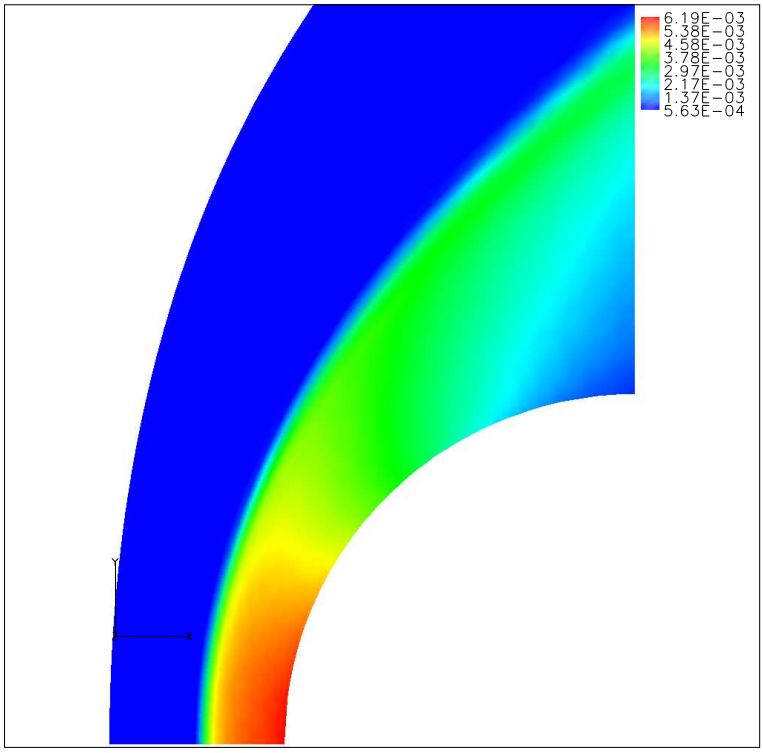

(b) DPLR

Figure 23: Density Contours

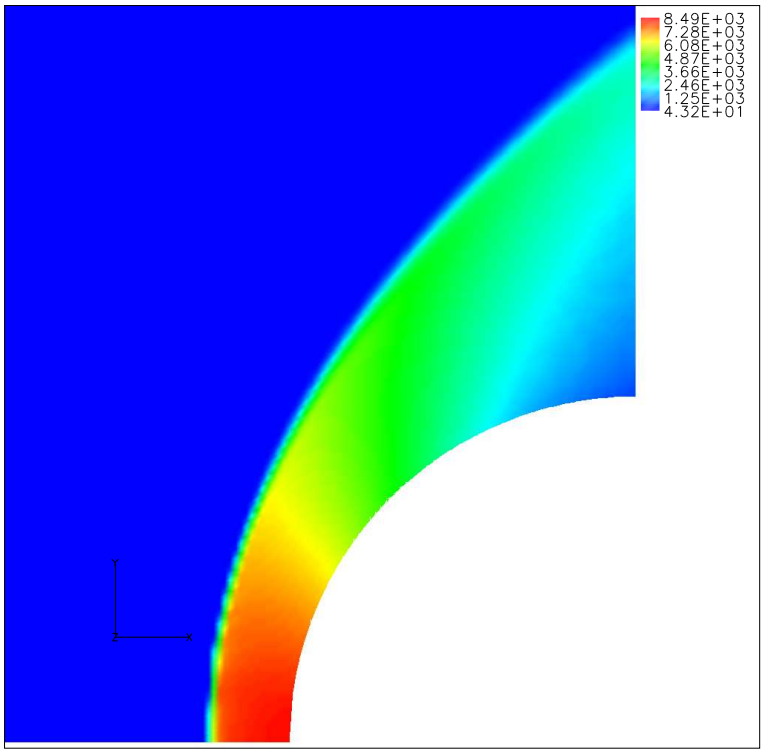

(a) NASCART-GT

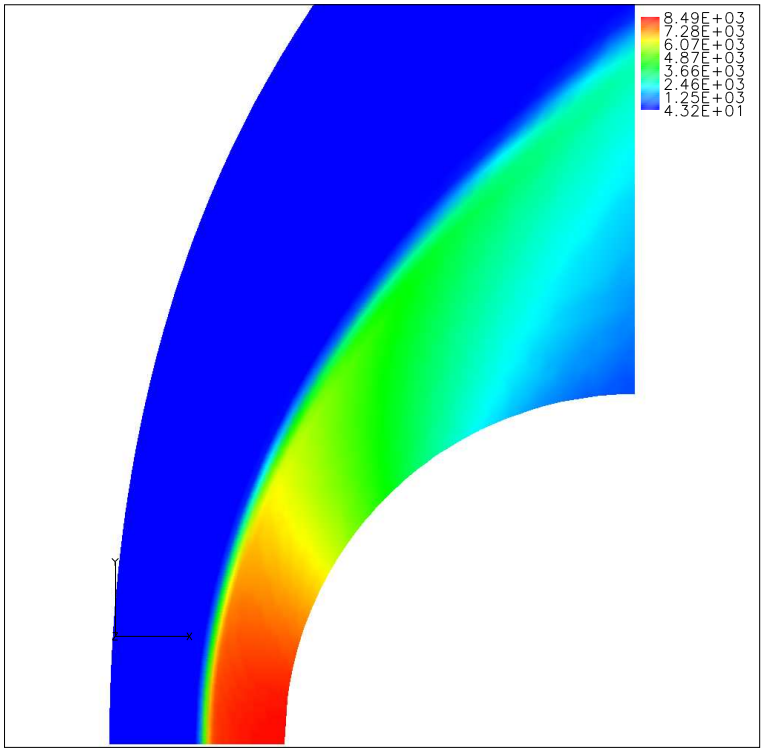

(b) DPLR

Figure 24: Pressure Contours

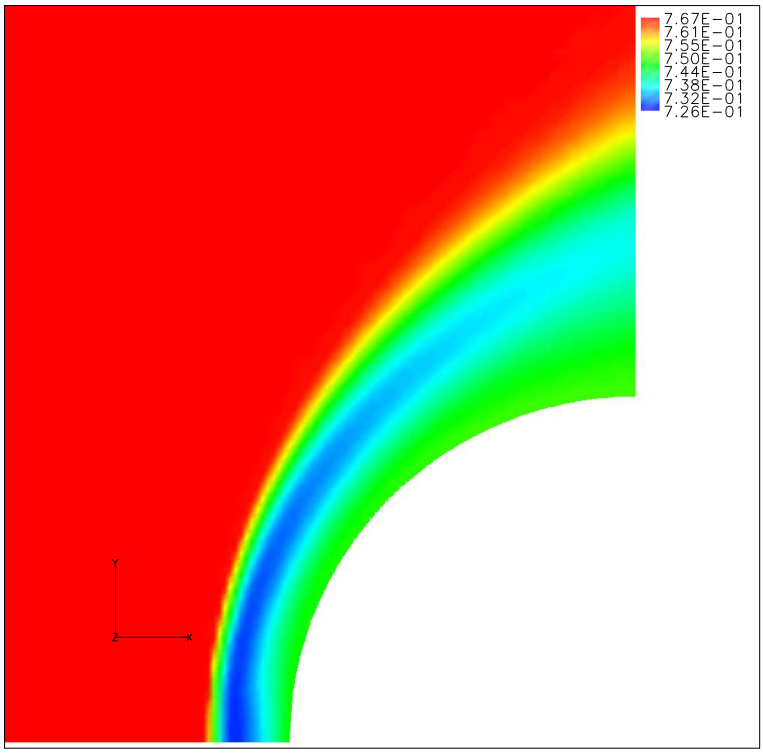

(a) NASCART-GT

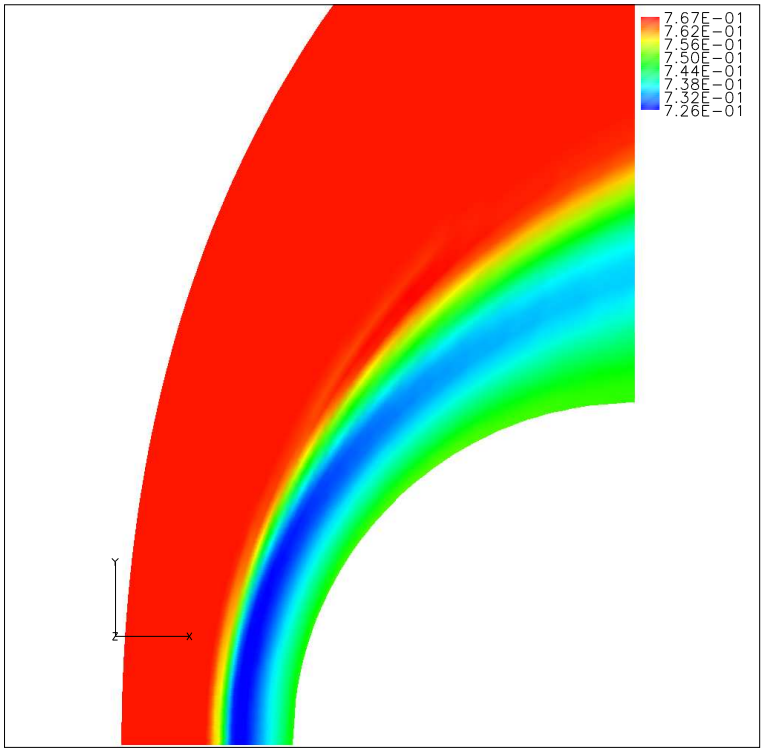

(b) DPLR

Figure 25: N2 mass concentration Contours

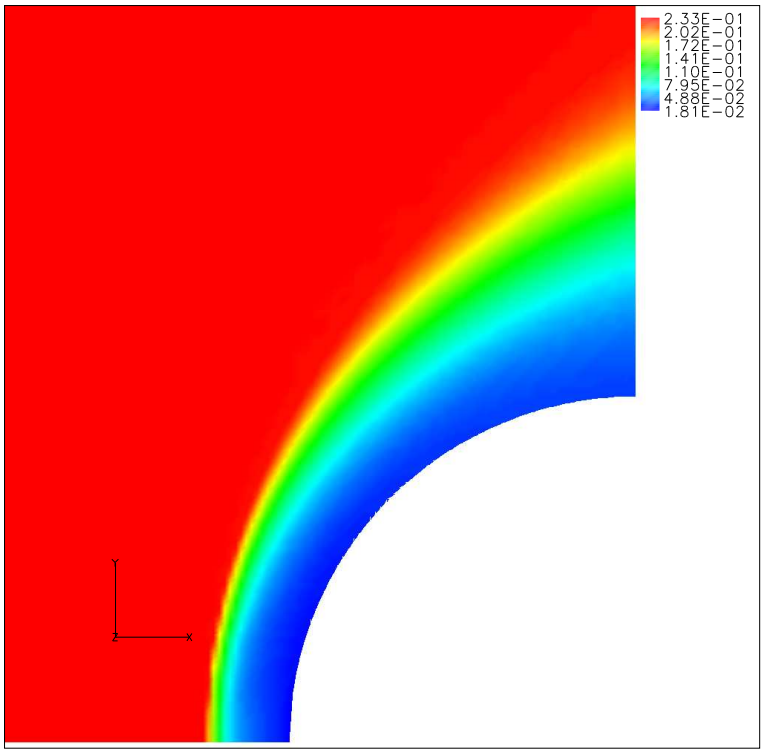

(a) NASCART-GT

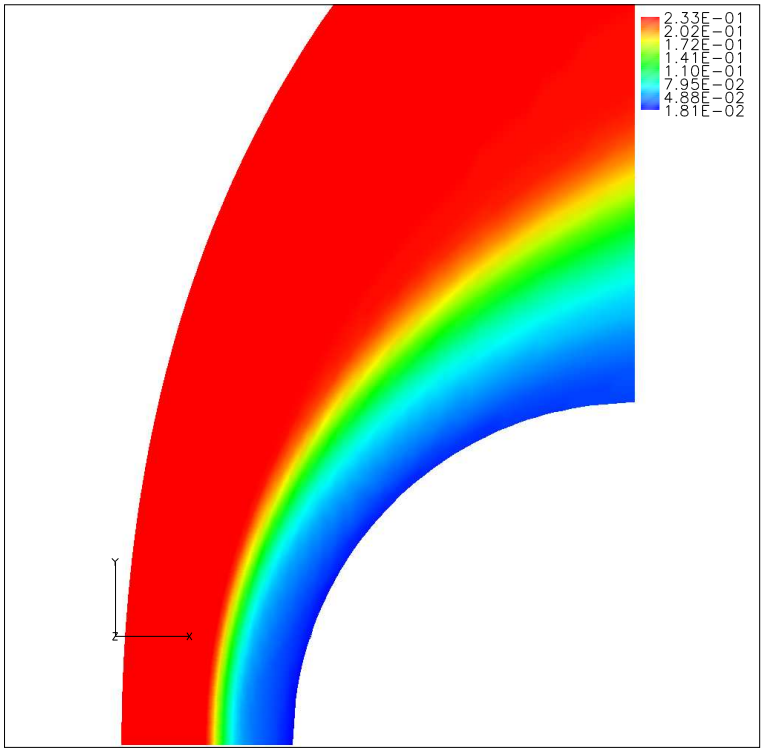

(b) DPLR

Figure 26: O2 mass concentration Contours

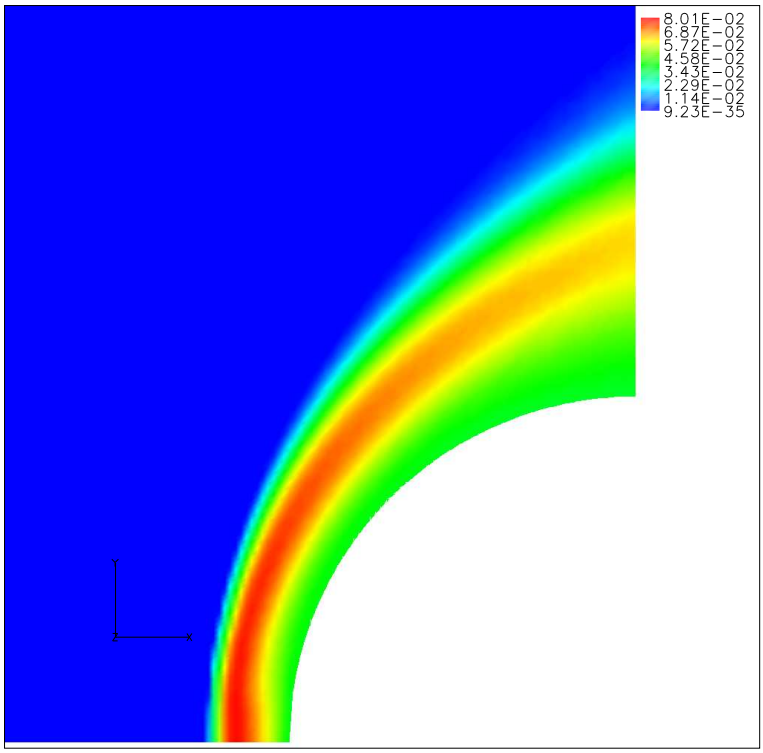

(a) NASCART-GT

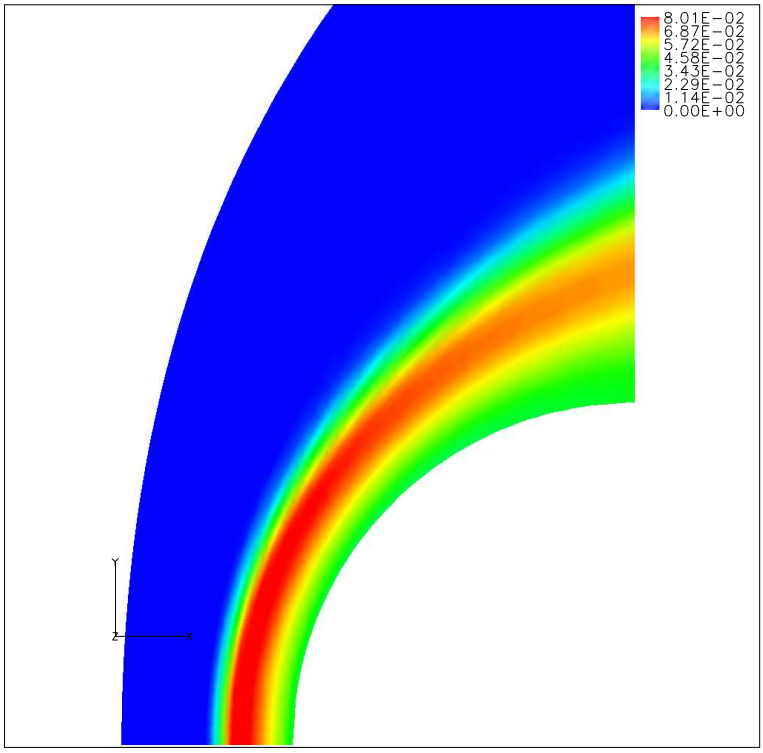

(b) DPLR

Figure 27: NO mass concentration Contours

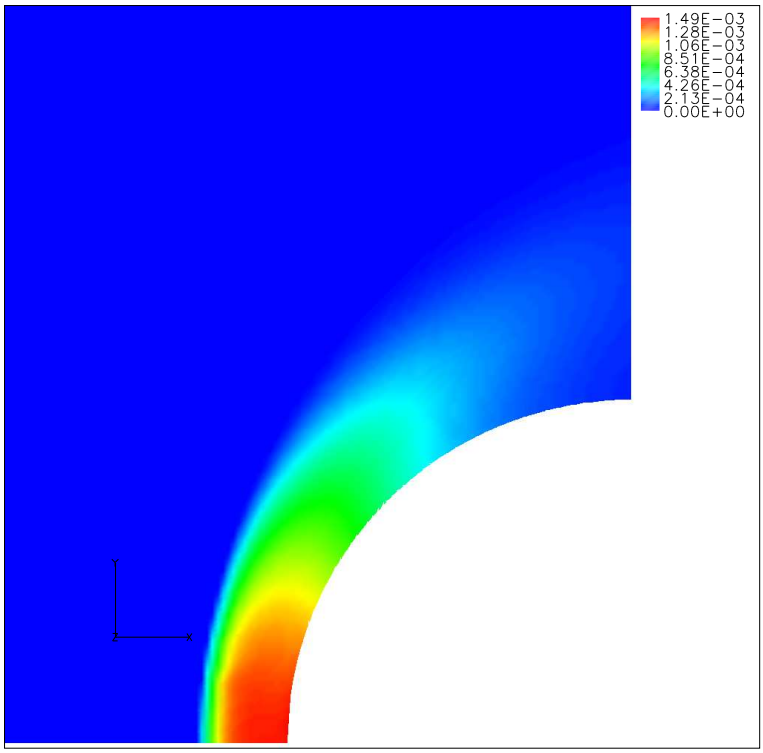

(a) NASCART-GT

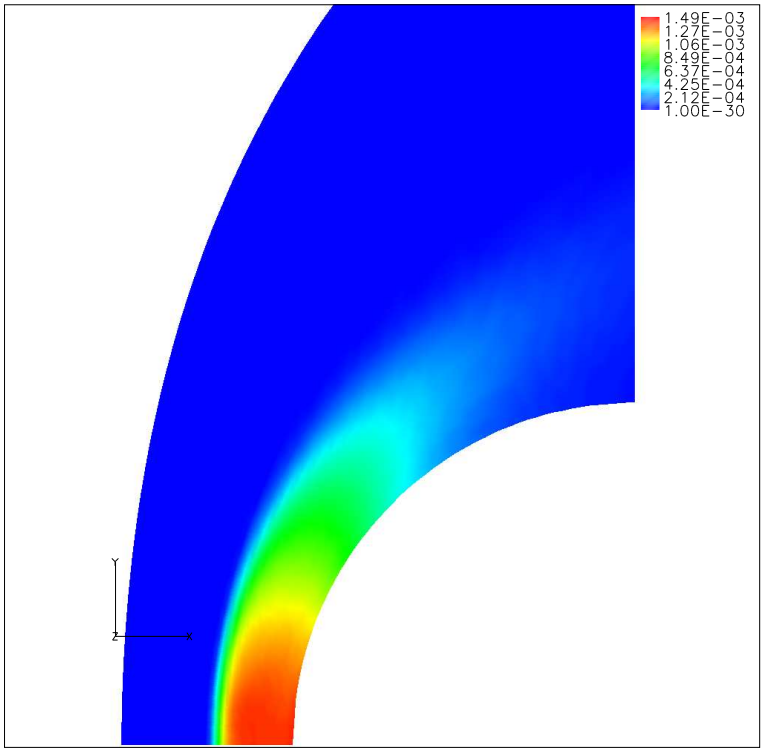

(b) DPLR

Figure 28: N mass concentration Contours

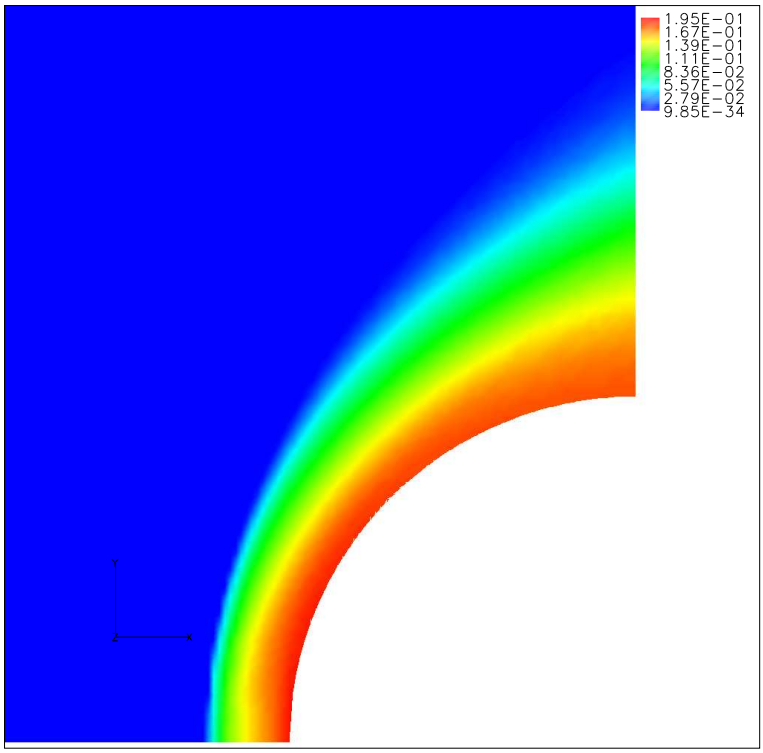

(a) NASCART-GT

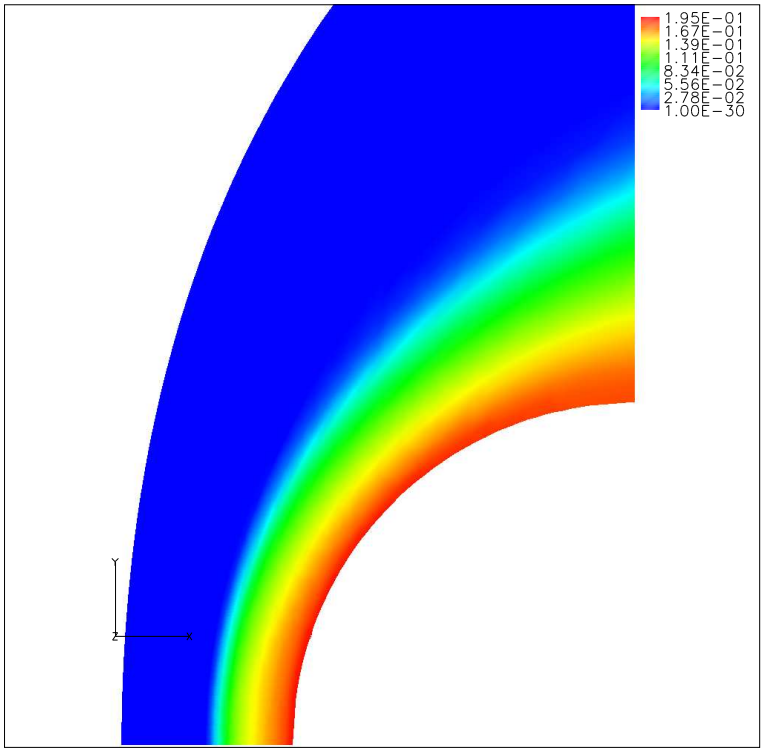

(b) DPLR

Figure 29: O mass concentration Contours

5.2 Thermochemical Non-Equilibrium Results

5.2.1 Results for Five Species Air Model

A test case for hypersonic flow around a circular cylinder(R=0.05m) was numerically simulated to test the present thermochemical nonequilibrium solver. Nonequilibrium effects are more apparent in this case than with the chemical nonequilibrium verification case described in the earlier section because the radius of the cylinder here is a tenth of the previous case. Therefore, this would be a good test case for verifying the implemented vibrational nonequilibrium model in addition to the chemical nonequilibrium model. The freestream Mach number, angle of attack, pressure and density are $M_\infty = 12.7, \alpha = 0, P_\infty = 90Pa, \rho_\infty = 0.0016kg/m^3$, respectively. A total of five species with 17 reaction steps have been used. The forward reaction rate model has been taken from Park's 1993 model. The total number of flow cells was 7352 and the solution adaption was performed after every 100 iterations based on the velocity divergence and species gradients. The grids shown in figure 30 confirms a good solution adaption along the shock wave and the species gradients in the post shock region.

Figures 31 to 39 show the flow properties around the hypersonic cylinder. As expected, the chemical composition contours indicate that the flow exhibits further nonequilibrium behavior than the results of the previous chapter. A steep rate of change of the chemical composition is present very close to the wall, and not much evidence of chemical reactions is found near the shock wave. This chemical nonequilibrium effect makes for a gradual density rise across the shock layers. On the other hand, the vibrational-electronic relaxation process responds rapidly from the shock front and becomes equilibrated with the translational mode from the mid shock layer region. This case has also been compared to DPLR's inviscid mode solution. The plots on the top in each figure are the results from present work, and ones below are the results from DPLR. Overall, flow properties within the shock layer show good agreement with DPLR, except that the chemical recombination rates of the present

work are a bit higher around the top surface of the cylinder as shown in Figure 35 and 36.

Figures 40 to 43 show the distribution of the flow properties along the stagnation line. The pressure curves show some noticeable under-prediction at the shock front when compared to DPLR. The agreement becomes better closer to the surface and finally disagrees by only 0.45% at the surface. The vibrational-electronic temperature of the current work shows a different relaxation slope compared to the vibrational temperature of DPLR. This discrepancy is expected because the present work uses a translational-rotational vs. vibrational-electronic temperature system, and DPLR uses a translational-rotational vs. vibrational temperature system. Hence, the temperature response to different heat capacities is somewhat different. Strictly speaking, both the system do not describe the actual physics of the gas molecules. This difference is also shown in a comparison between DPLR and LAURA in a recent publication [37], where LAURA also uses the same convention as the present work. The chemical compositions along the stagnation line coincide very well with DPLR.

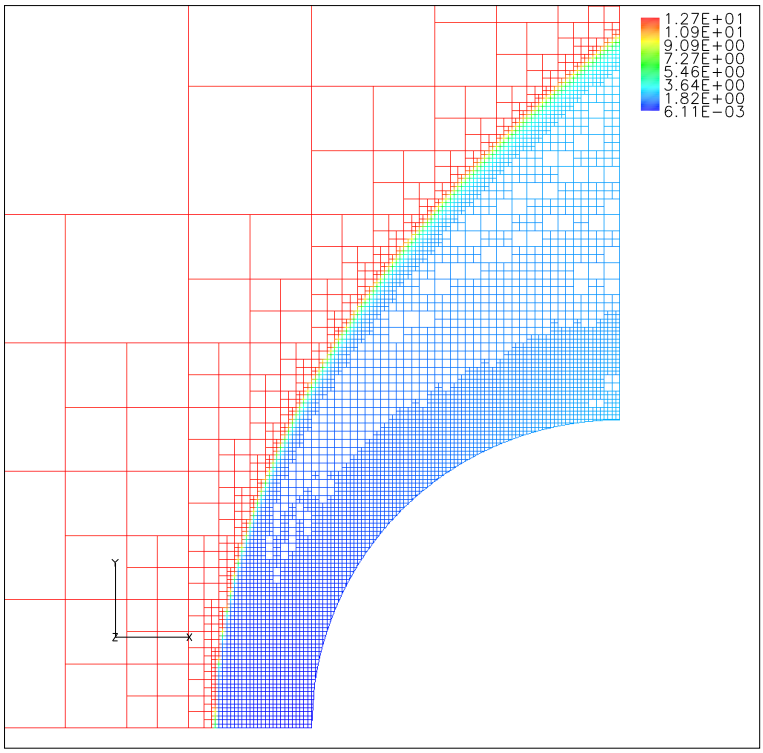

(a) NASCART-GT

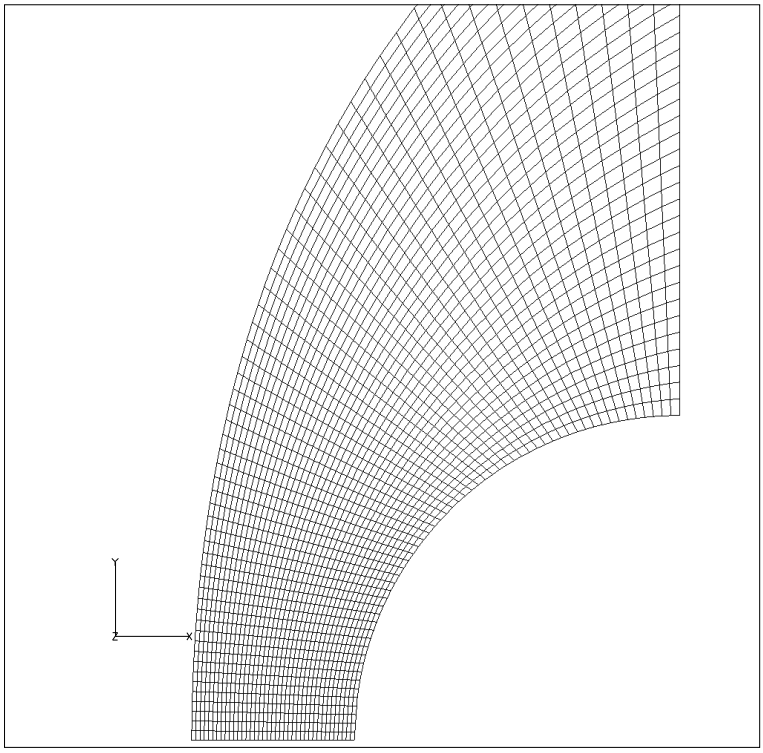

(b) DPLR

Figure 30: Grid over 0.5m Cylinder, Top:NASCART-GT, Bottom:DPLR

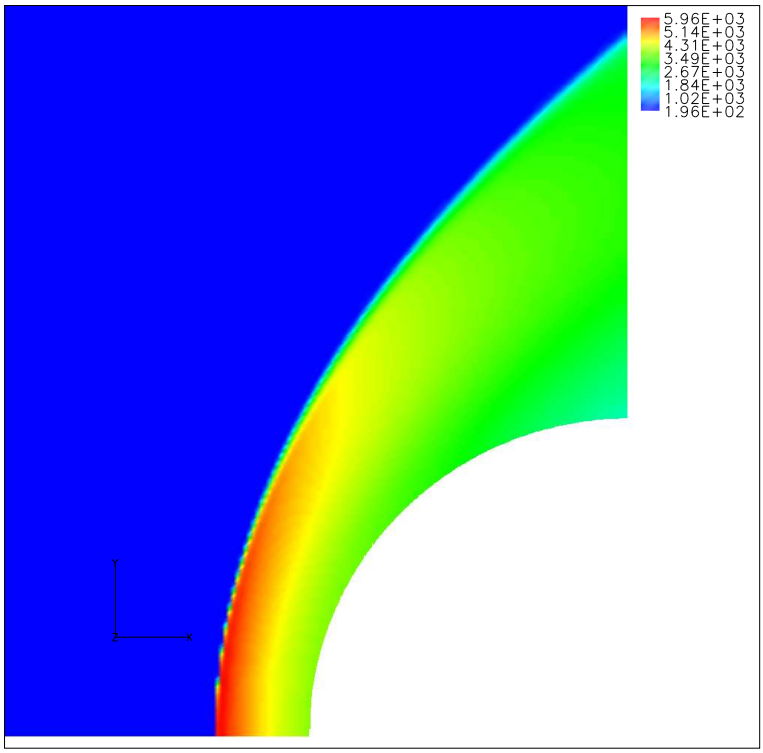

(a) NASCART-GT

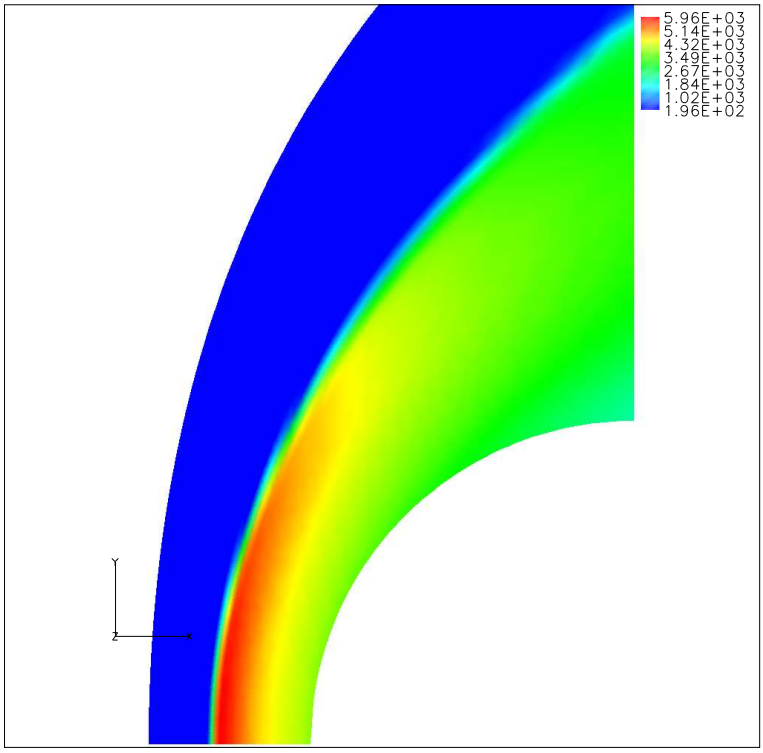

(b) DPLR

Figure 31: Temperature Contours with Shock Layer

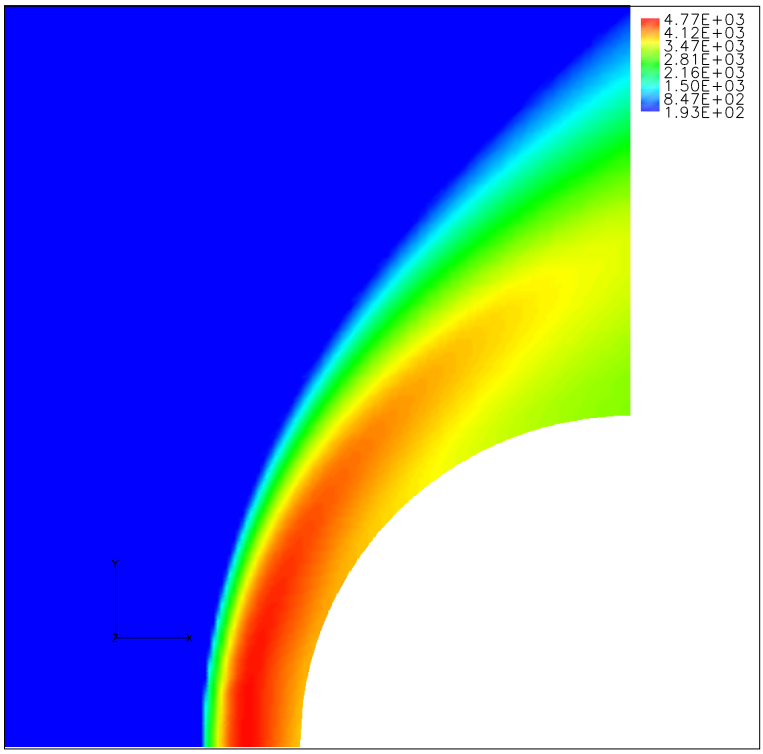

(a) NASCART-GT

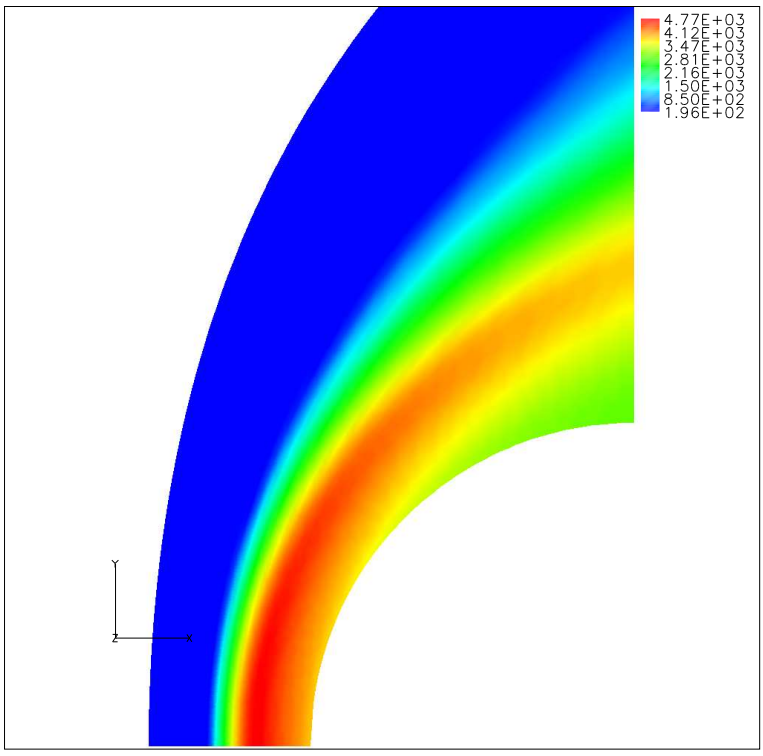

(b) DPLR

Figure 32: Vibrational-Electronic vs. Vibrational Temperature Contours with Shock Layer

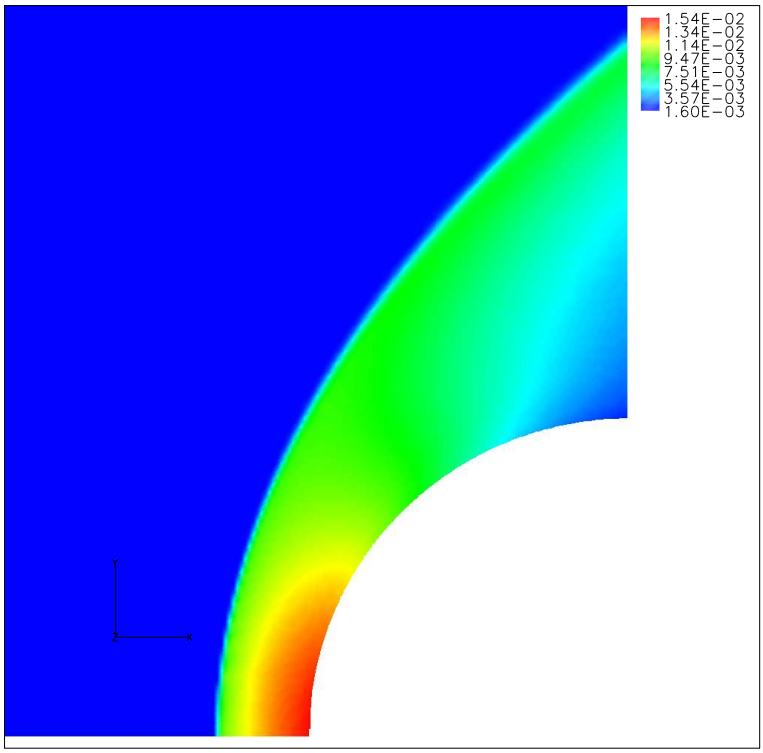

(a) NASCART-GT

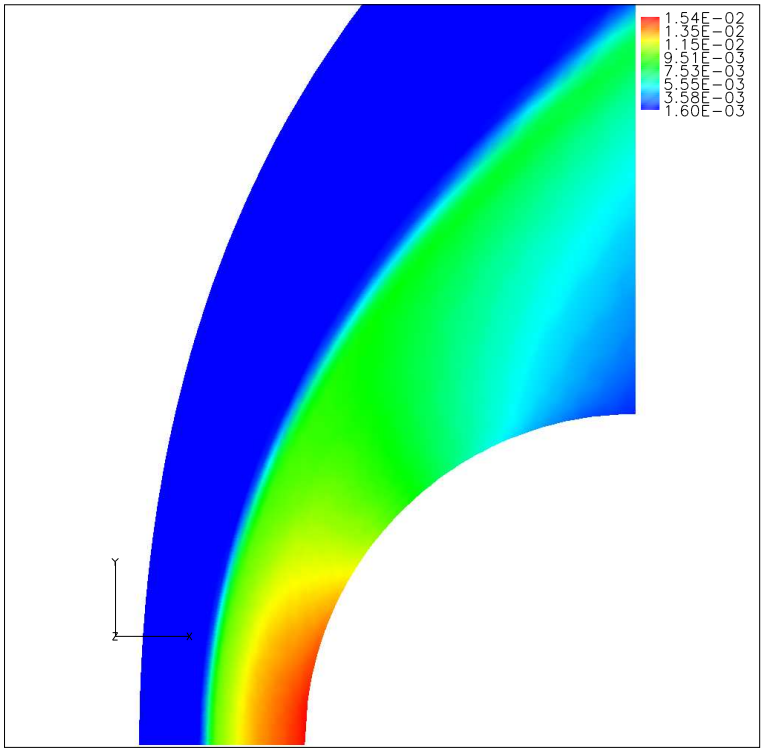

(b) DPLR

Figure 33: Density Contours

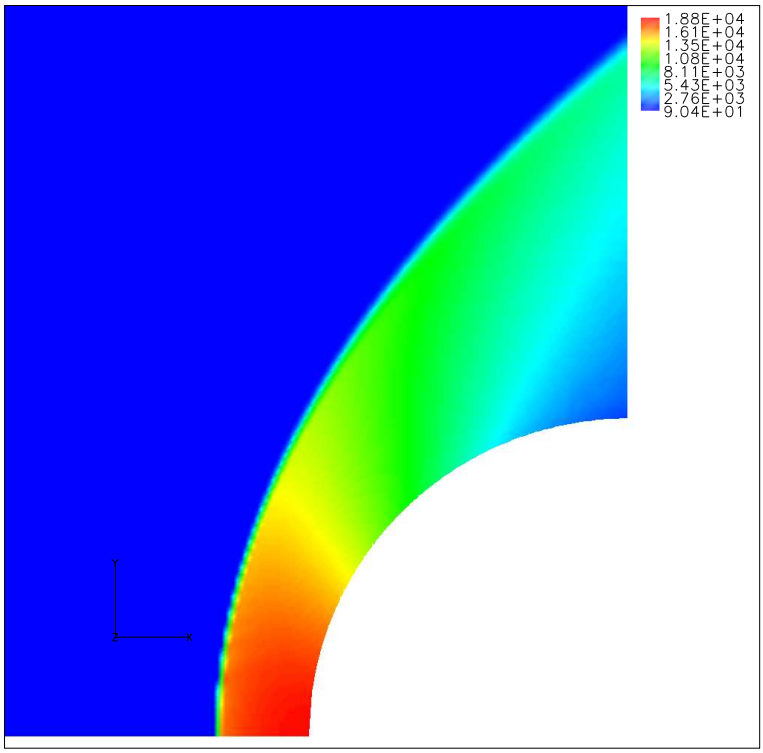

(a) NASCART-GT

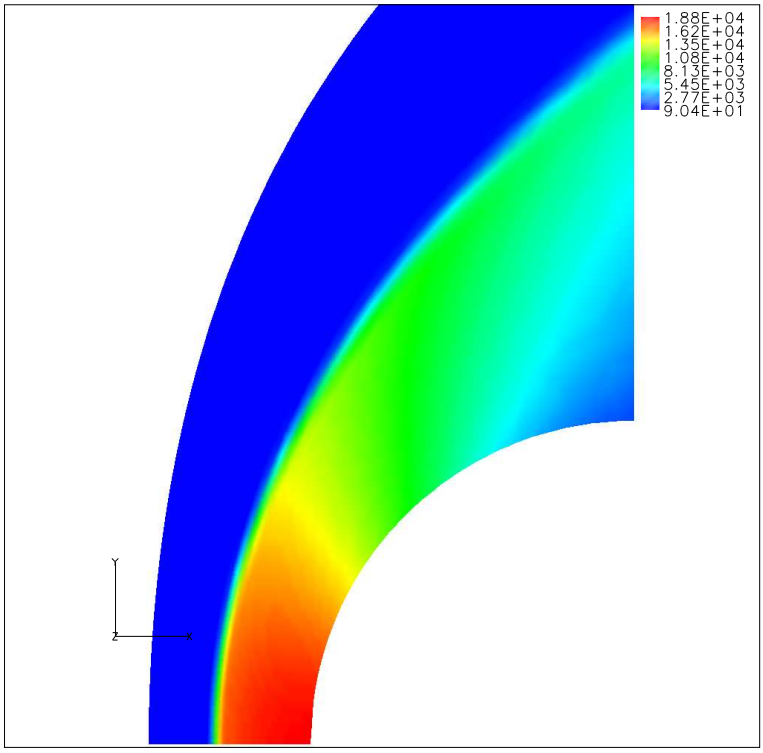

(b) DPLR

Figure 34: Pressure Contours

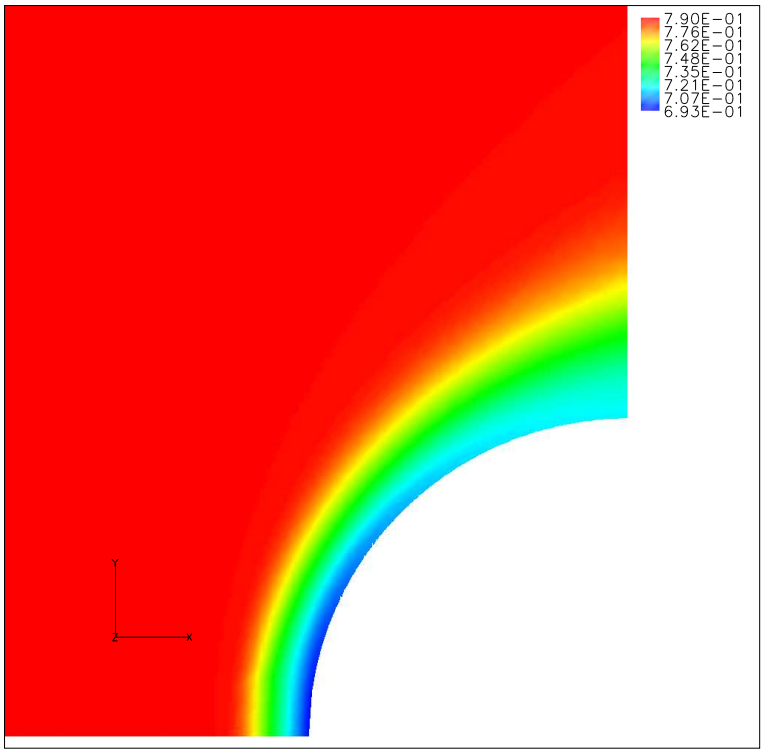

(a) NASCART-GT

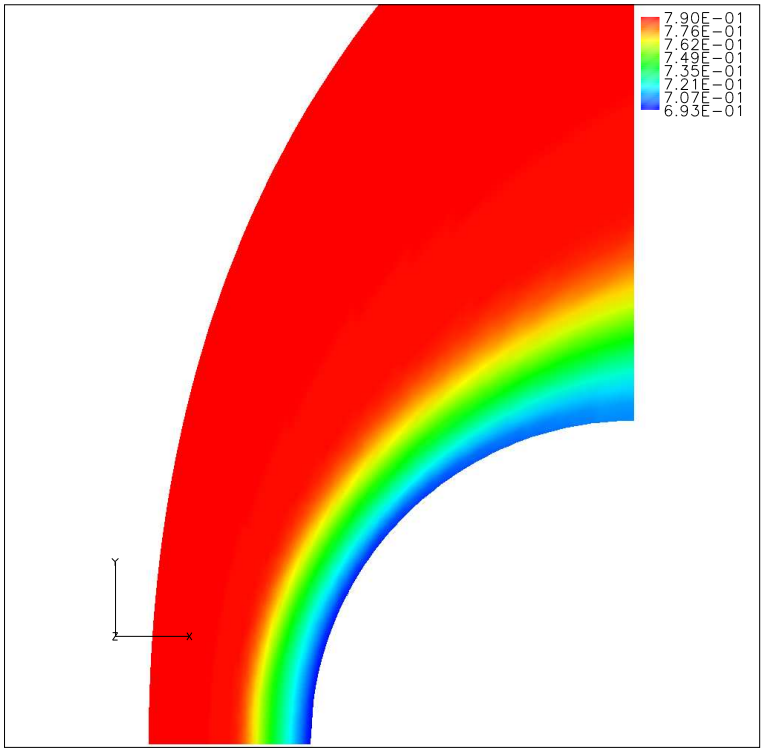

(b) DPLR

Figure 35: N2 mass concentration Contours

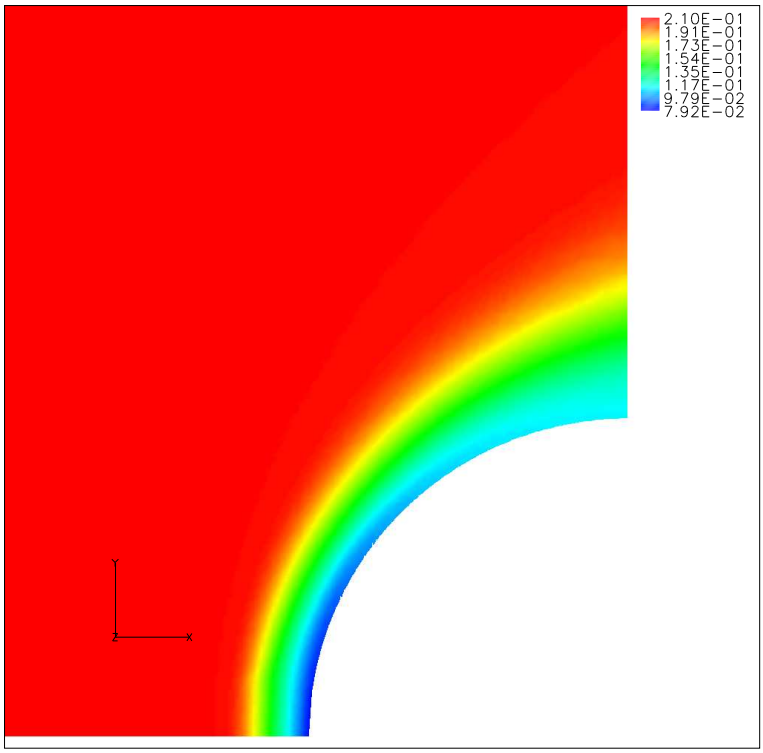

(a) NASCART-GT

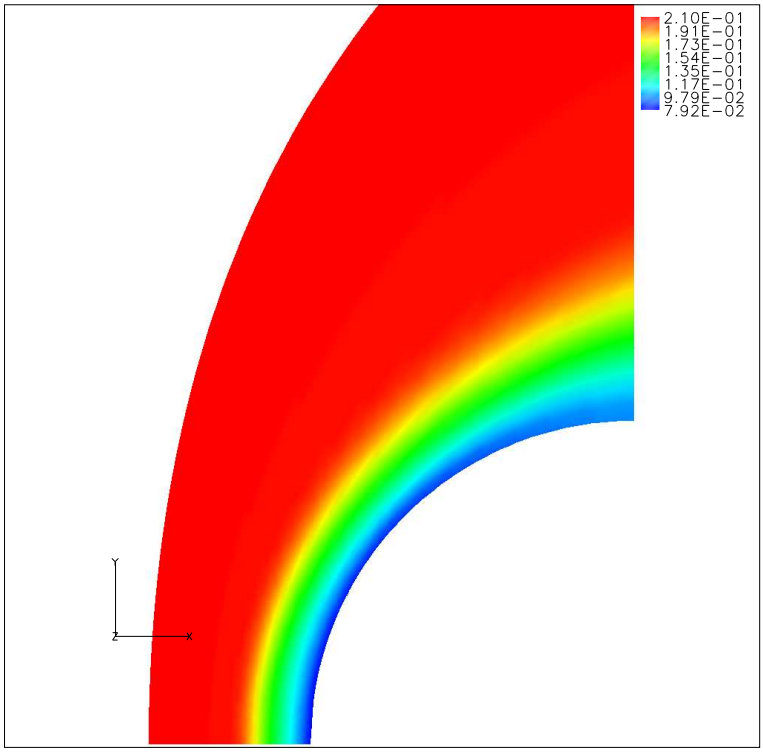

(b) DPLR

Figure 36: O2 mass concentration Contours

(a) NASCART-GT

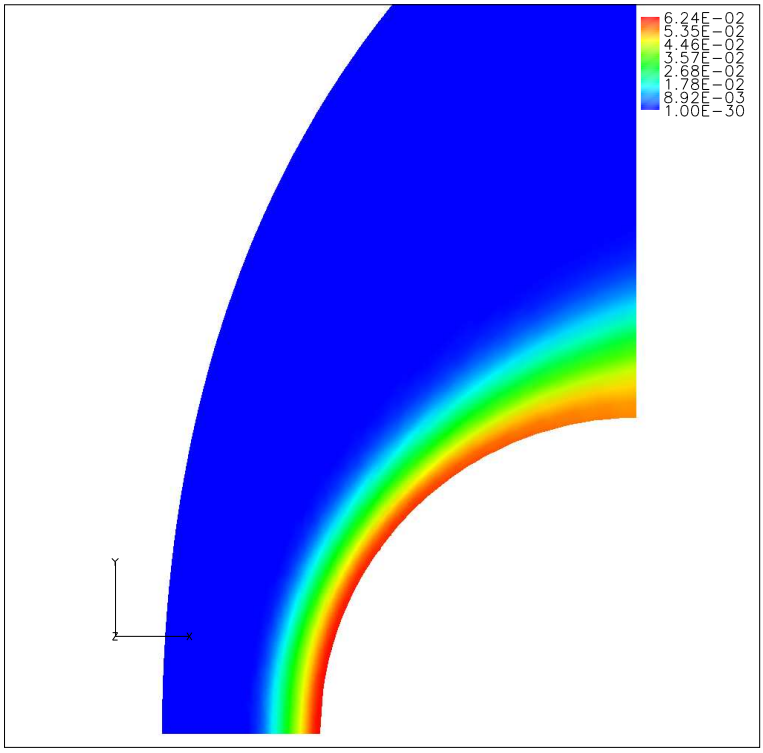

(b) DPLR

Figure 37: NO mass concentration Contours

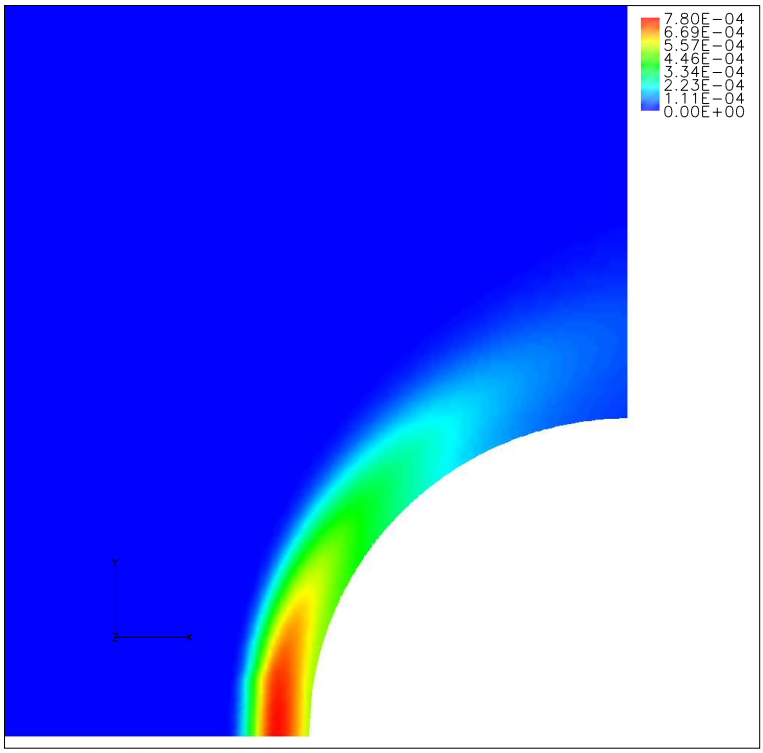

(a) NASCART-GT

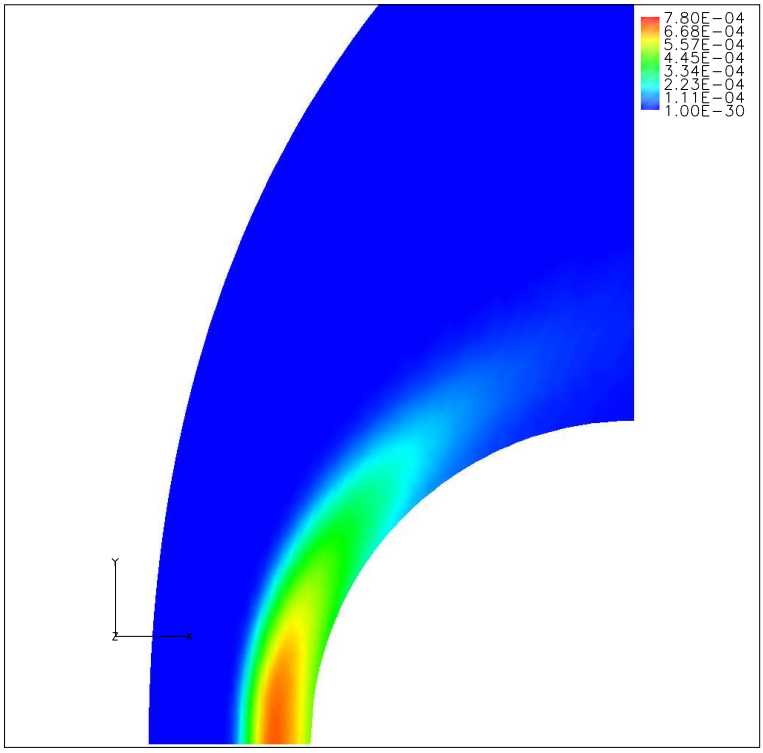

(b) DPLR

Figure 38: N mass concentration Contours

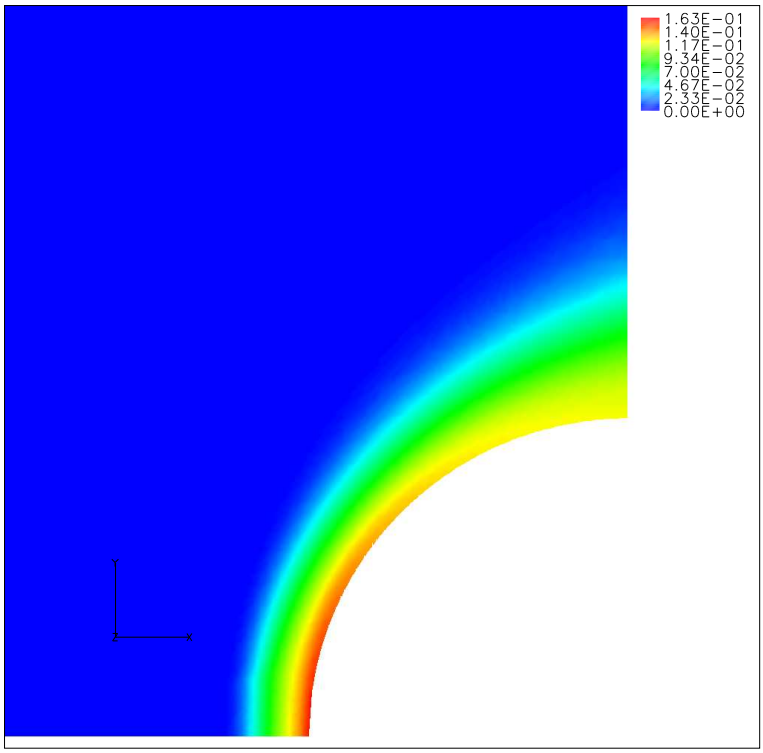

(a) NASCART-GT

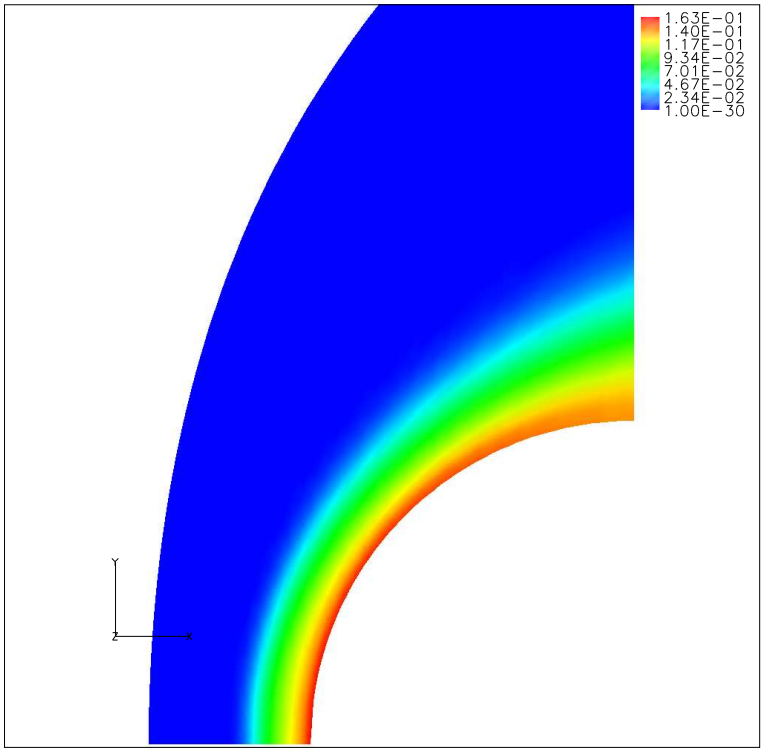

(b) DPLR

Figure 39: O mass concentration Contours

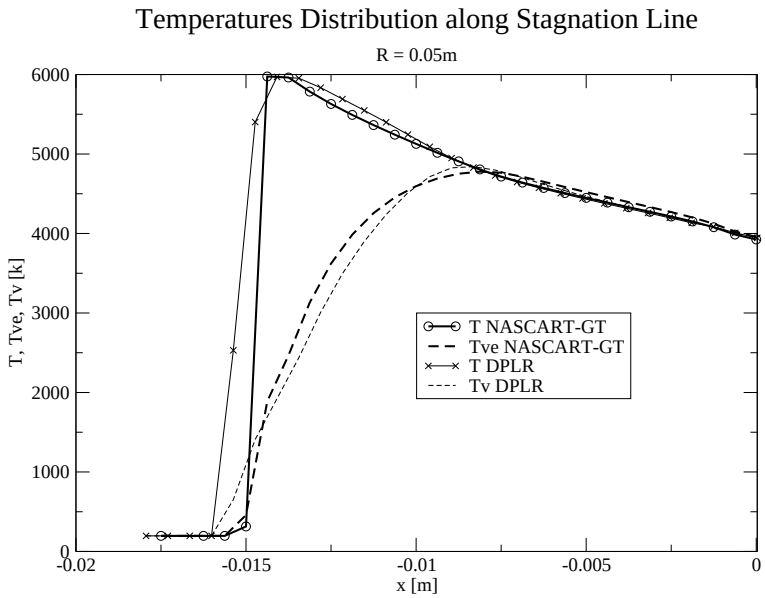

Figure 40: Temperature Distribution along Stagnation Line

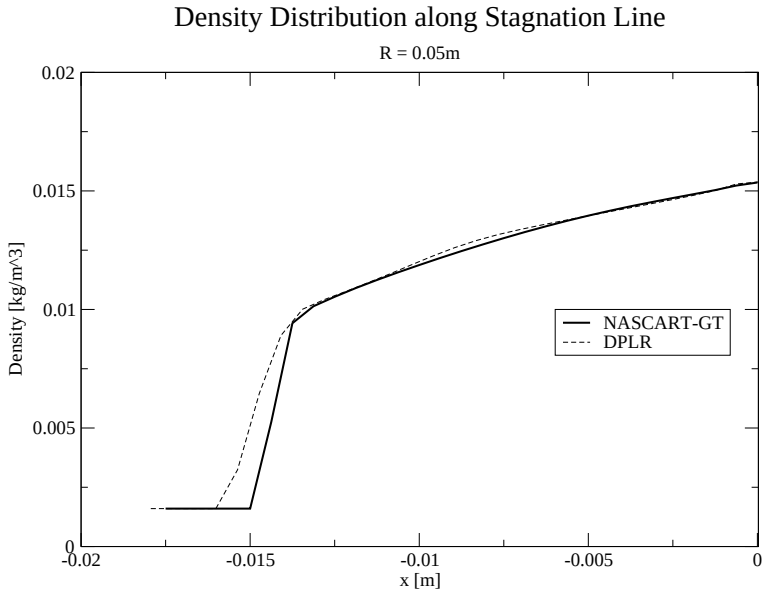

Figure 41: Density Distribution along Stagnation Line

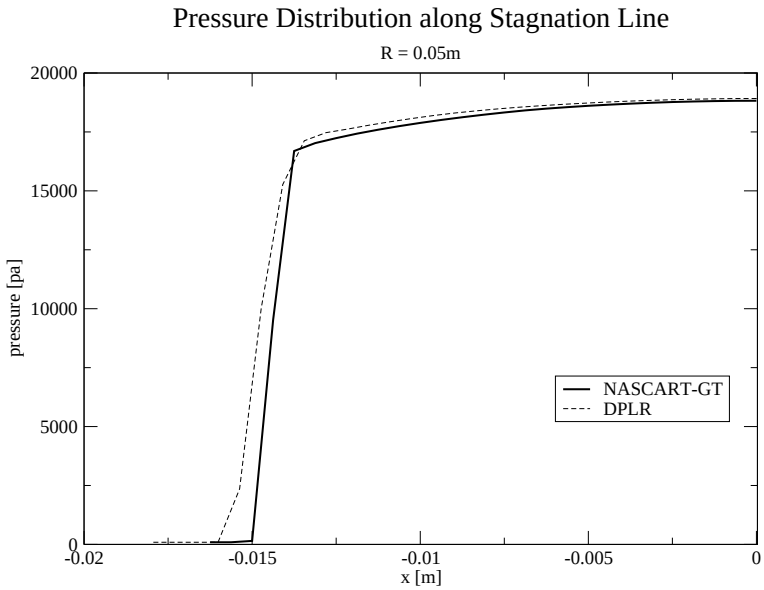

Figure 42: Pressure Distribution along Stagnation Line

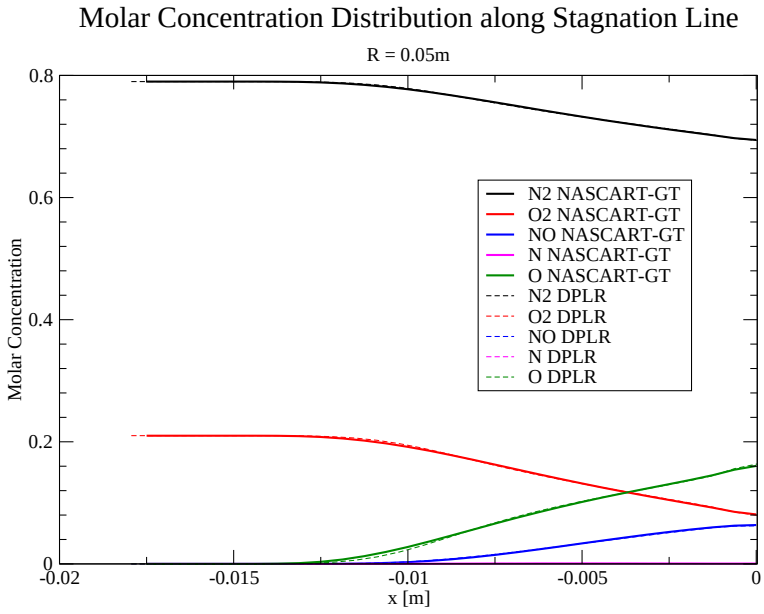

Figure 43: Mass Concentration Distribution along Stagnation Line

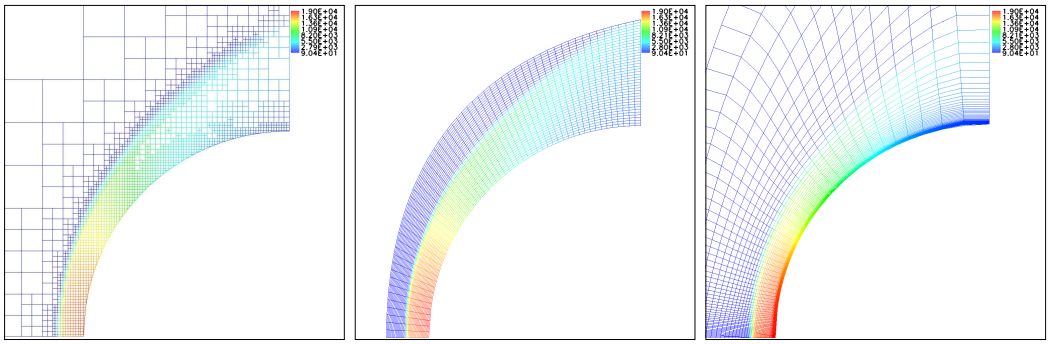

(a) NASCART-GT(Inviscid) (b) DPLR(Inviscid) (c) DPLR(Viscous)

Figure 44: Pressure contours over Sphere

5.2.2 Validation against experimental data

A test case for hypersonic flow around a sphere (R=0.05m) was numerically simulated to validate against experimental data. The freestream Mach number, angle of attack, pressure and density are $M_\infty = 12.7, \alpha = 0, P_\infty = 90Pa, \rho_\infty = 0.0016kg/m^3$, respectively, which are identical to the previous thermochemical verification case over a 2D cylinder. The physical modeling and numerical methods are also identical to the previous case. Figure 44 shows the pressure contours over the sphere. The 3D relieving effect generated a more oblique shock when compared to the pressure contour of the cylinder, Figure 34, at same freestream conditions. Figure 45 shows the surface pressures compared to the experimental data [77]. The present surface pressure results agree well with the experimental data and also with the well-validated DPLR code. A viscous case was also simulated using DPLR with isothermal wall boundary condition at $290K$ to investigate non-adiabatic viscous effects on the wall pressure. As shown in Figure 45, the viscous effect has no impact on the surface pressure.

5.2.3 Results for 13 species Titan Model

The peak dynamic pressure point of the Huygens Probe for Titan's mission was simulated as a test case to check the present thermochemical nonequilibrium solver under a N2-CH4-AR system. The Huygens probe [12], shown schematically in Figure

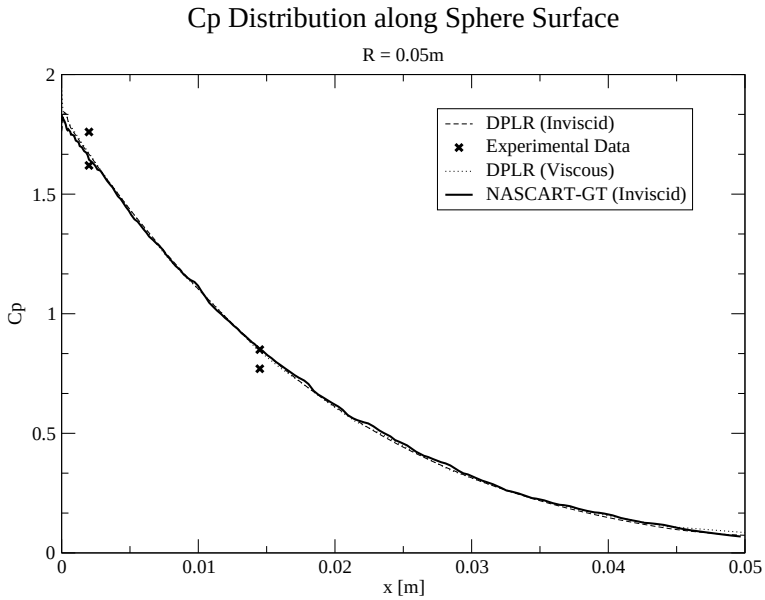

Figure 45: Pressure coefficient distribution along sphere surface

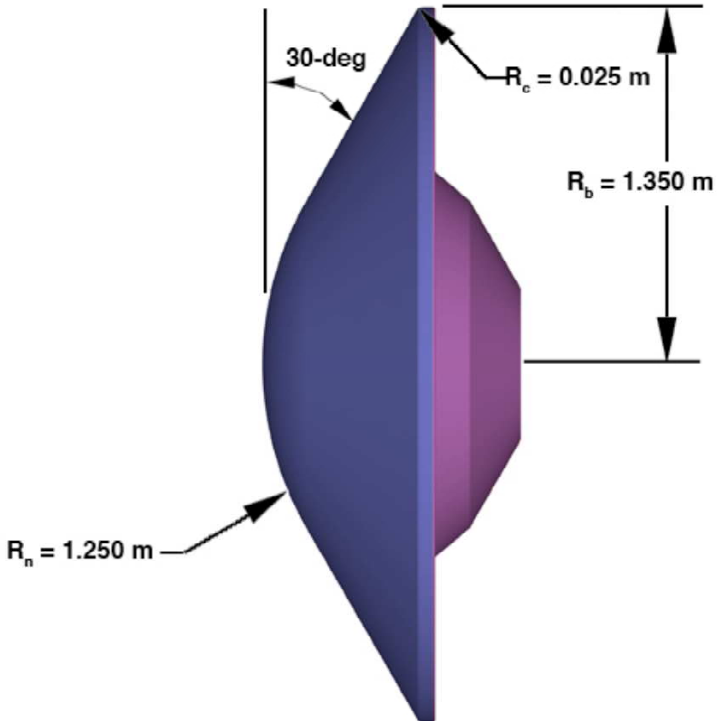

Figure 46: Schematic diagram of Huygens entry probe [12]

46, is a 60 degree half-angle sphere-cone with a diameter of 2.7 m and a nose radius of 1.25 m.

The free stream Mach number, angle of attack, pressure and density were $M_\infty = 18.8585, \alpha = 0, P_\infty = 15.621pa, \rho_\infty = 0.000296kg/m^3$, respectively. A total of thirteen species with 24 reaction steps were used. The forward reaction rate model was taken from Gökçen model. The total number of flow cells was 11224 with an nbmin selection of 512 and solution adaption being performed after every 100 iterations, based on velocity divergence and species gradients. The input parameter, nbmin, is the minimum number of surface grid points in the longest direction on the body.

This case was also compared to DPLR's inviscid mode solution. Figure 47 shows the NASCART grid and the structured grids for DPLR. A 60 x 40 grid was used for DPLR. The top section in each figure of 48 to 56 is the result of the present work, and the bottom section is the results from DPLR. Despite the complexity of the chemical systems, the value and distribution of flow properties, overall, match well with the verification data except for some minor discrepancies. The temperature contours agree pretty well in general and show 2% difference at the stagnation point. The present work has a better resolved shock wave as discussed in the earlier cylinder cases. For the density contours, it is interesting to note that both the solvers predict the location of the highest density point at about +0.07m away from the stagnation point in the radial direction. The density value of the current work at this point is about 2% less than that of the verification data. Also, the density and the pressure contours show that the present work has a slightly higher magnitude in the shock layers near the mid span. In terms of the chemical compositions, DPLR shows a bit more reactive than the current work but the distribution of species show similar patterns.

Figures 57 to 60 show the flow property distribution along the stagnation line. They also agree well with the verification data except that, again, the present work shows a more discrete shock front.

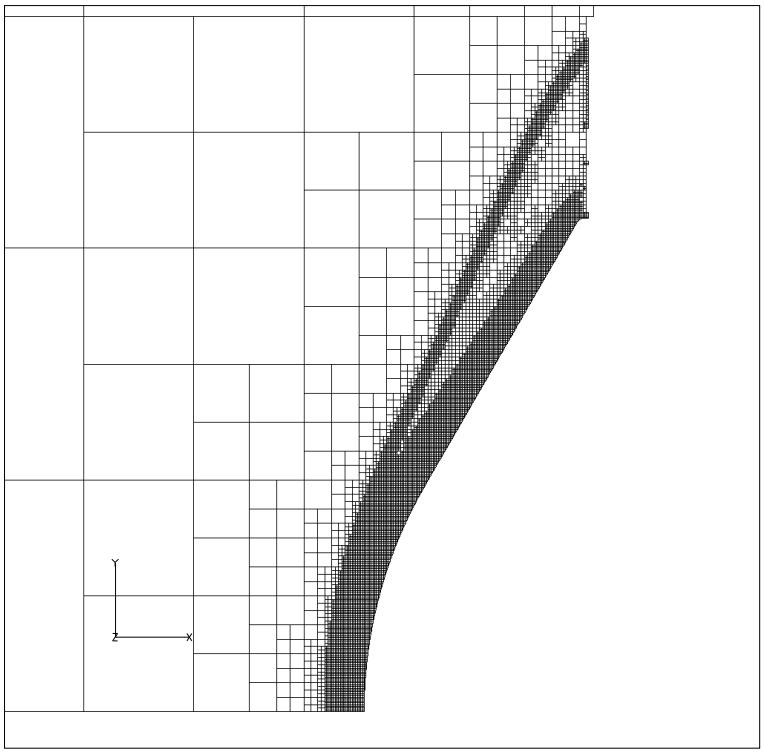

(a) NASCART-GT

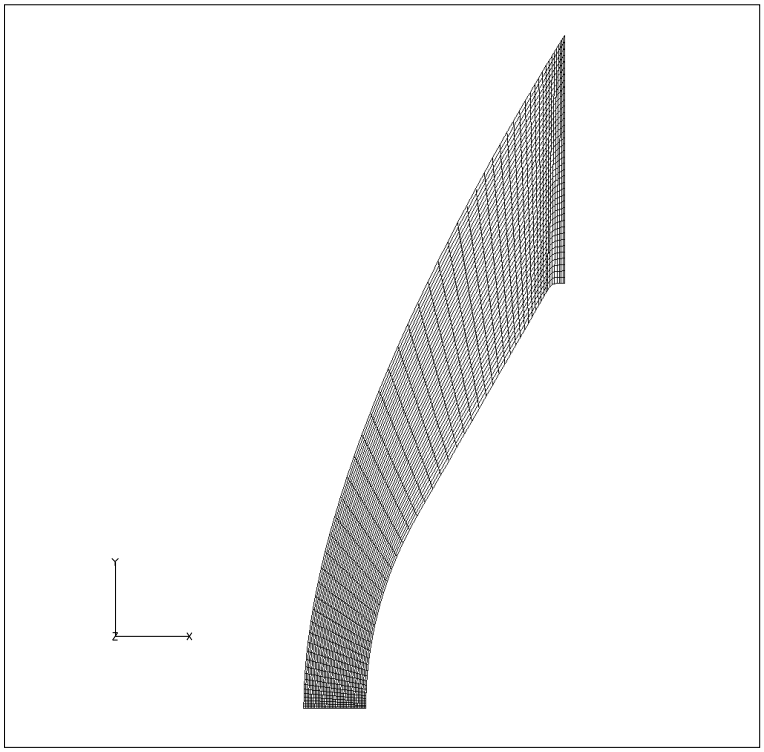

(b) DPLR

Figure 47: Grid over Hugens Probe

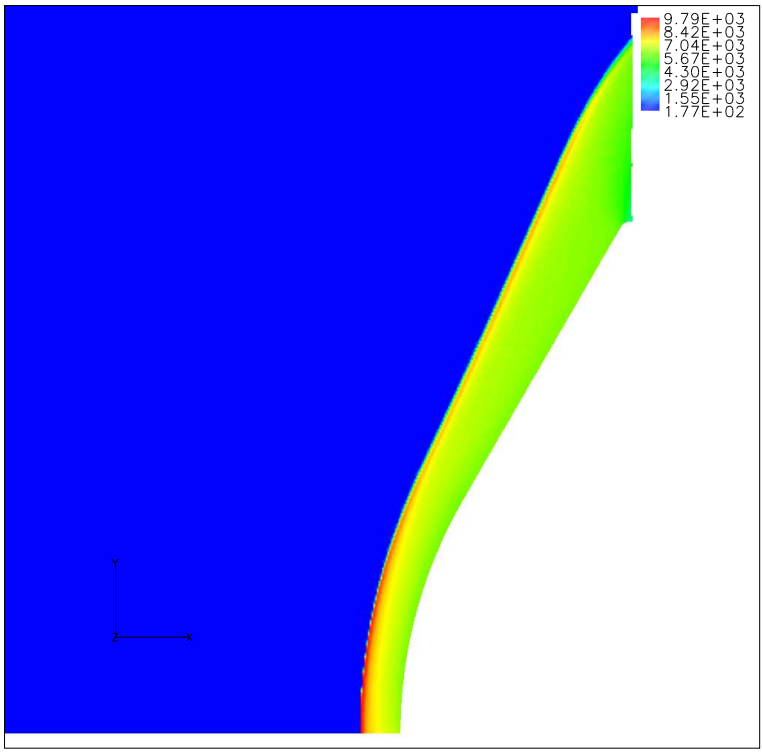

(a) NASCART-GT

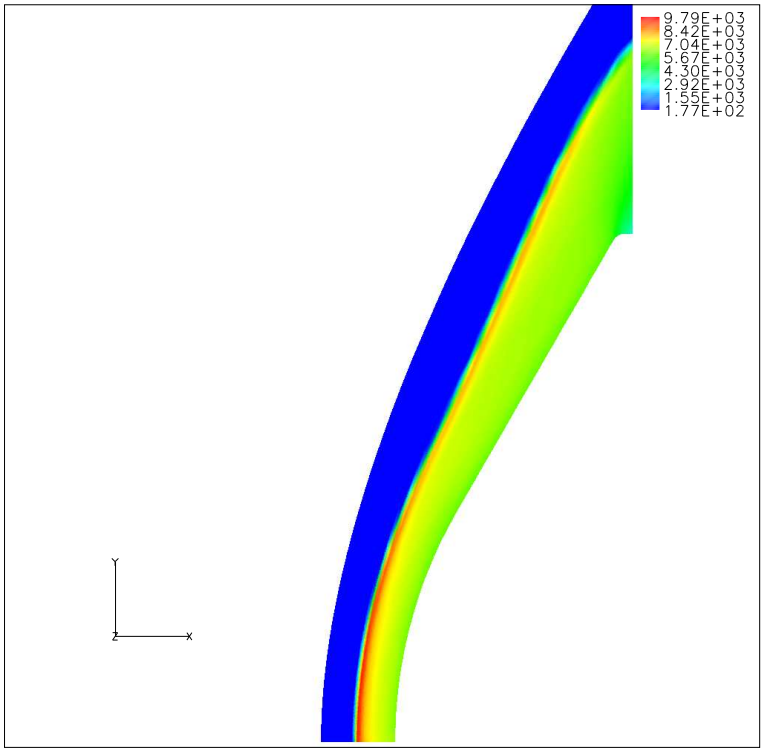

(b) DPLR

Figure 48: Temperature Contours

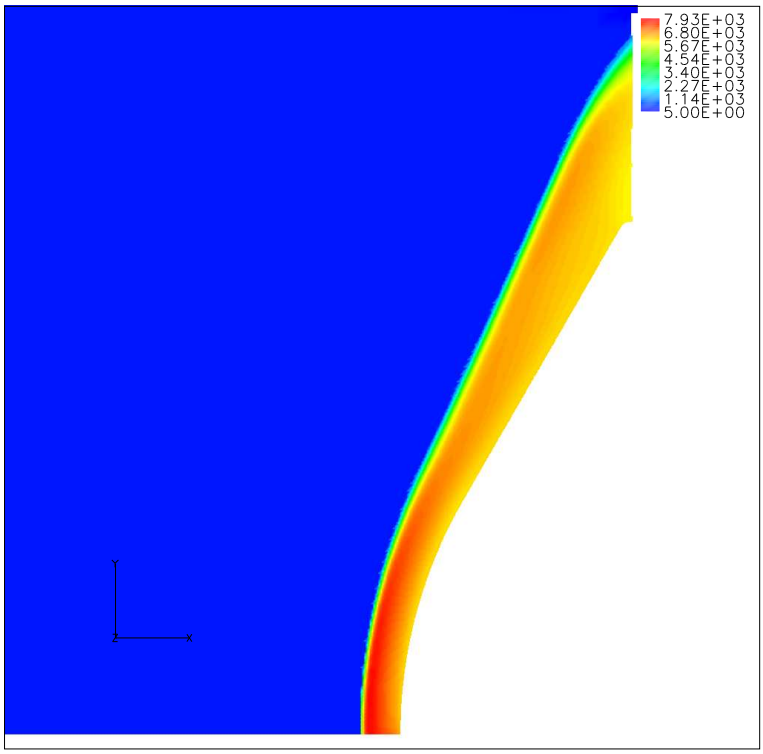

(a) NASCART-GT

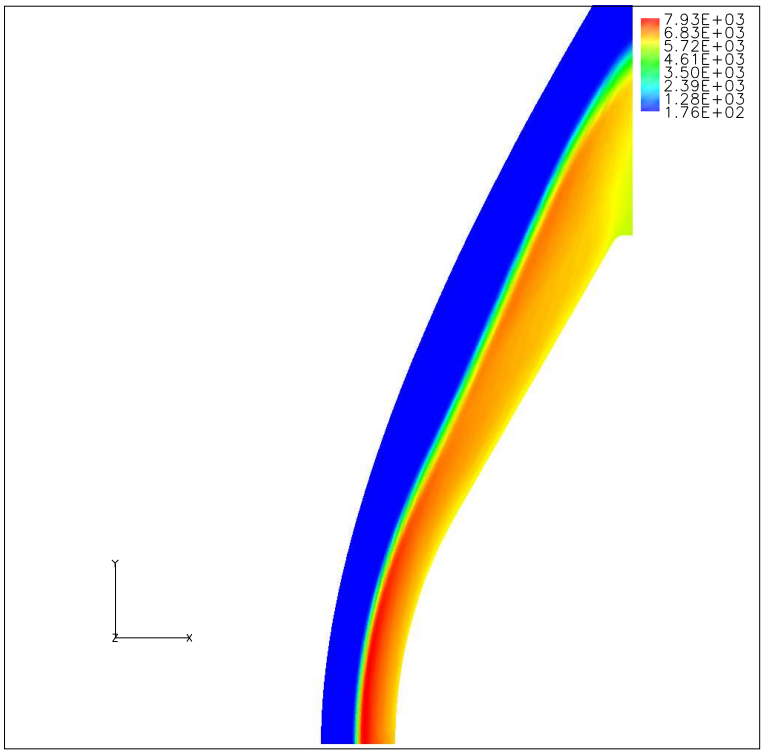

(b) DPLR

Figure 49: Vibrational-Electronic vs. Vibrational Temperature Contours

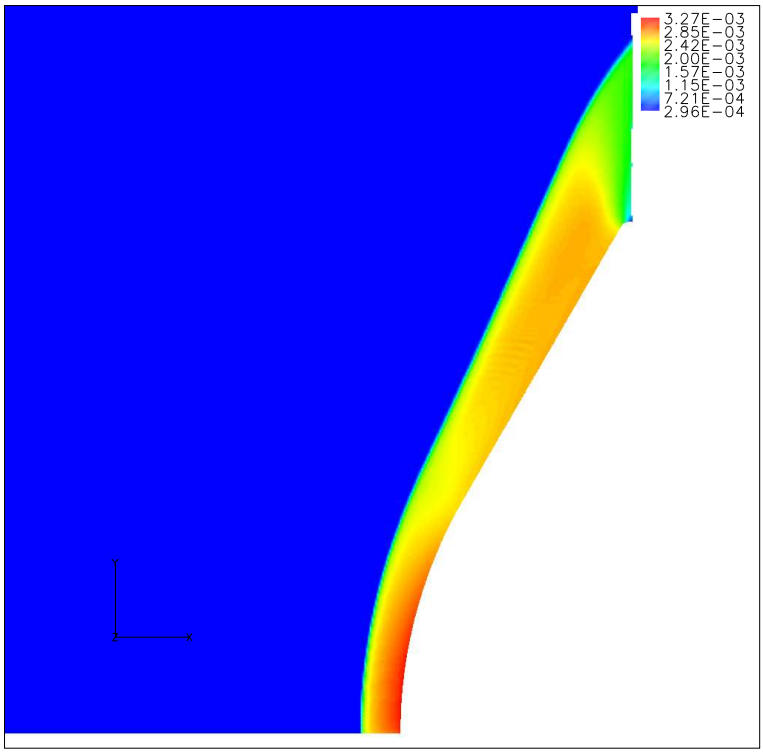

(a) NASCART-GT

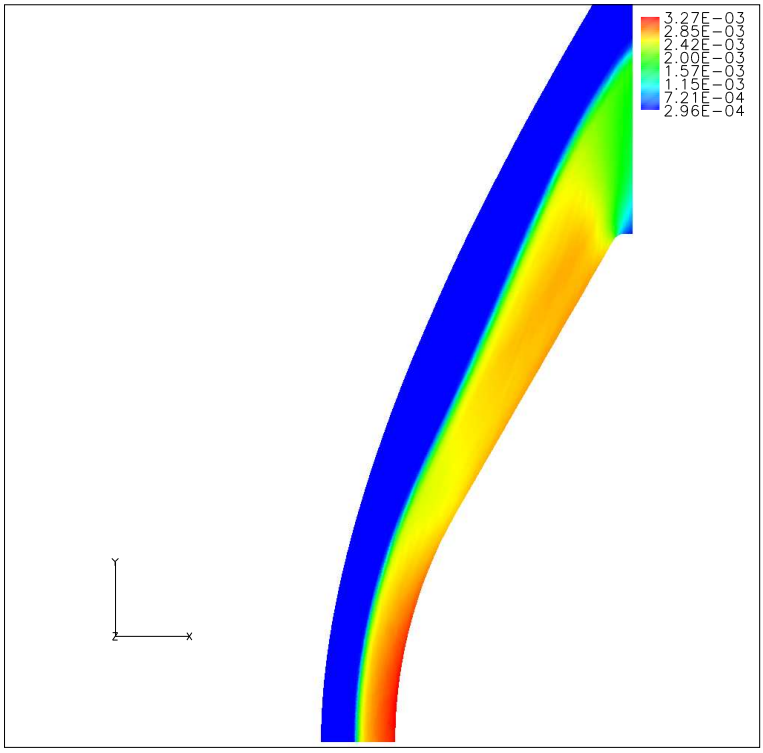

(b) DPLR

Figure 50: Density Contours

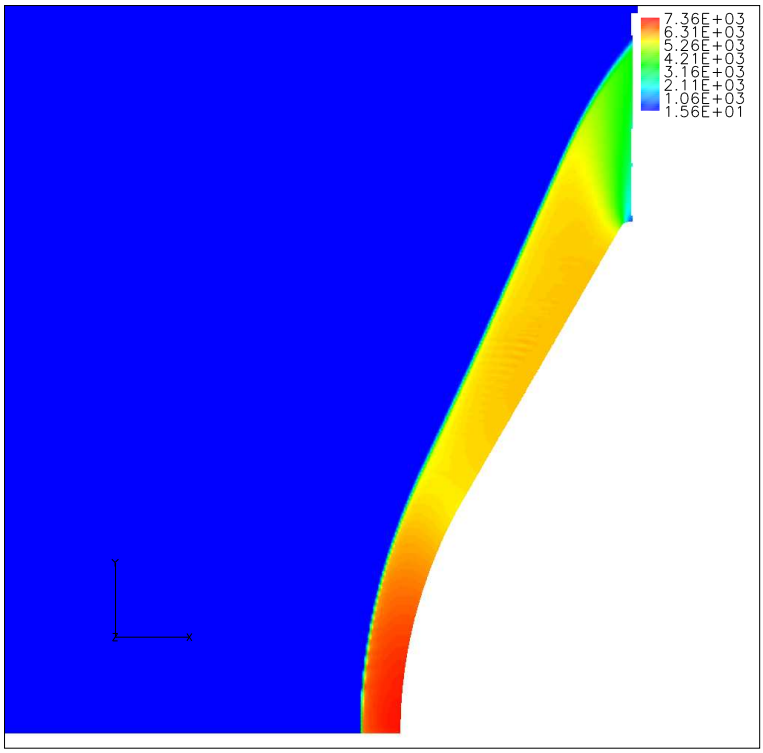

(a) NASCART-GT

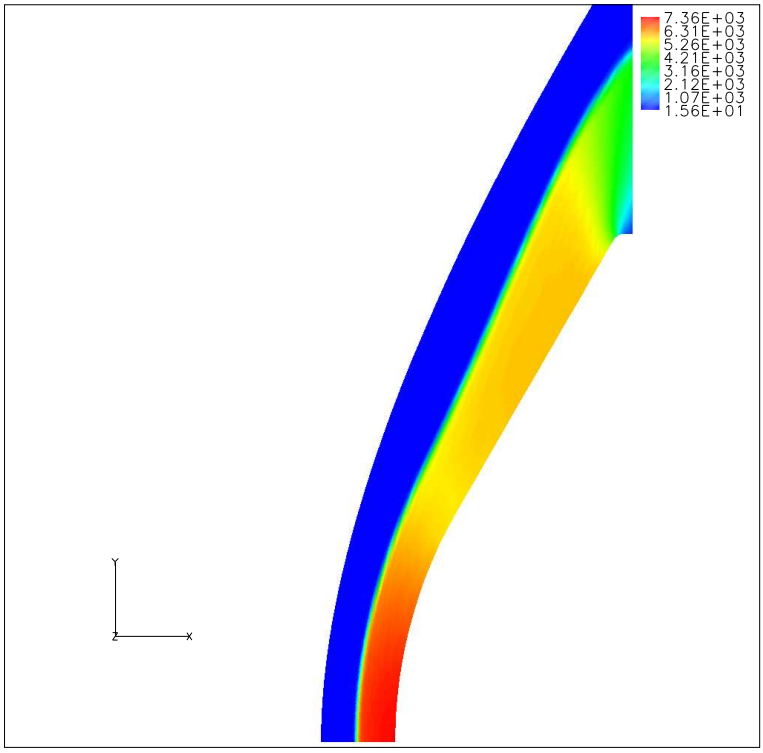

(b) DPLR

Figure 51: Pressure Contours

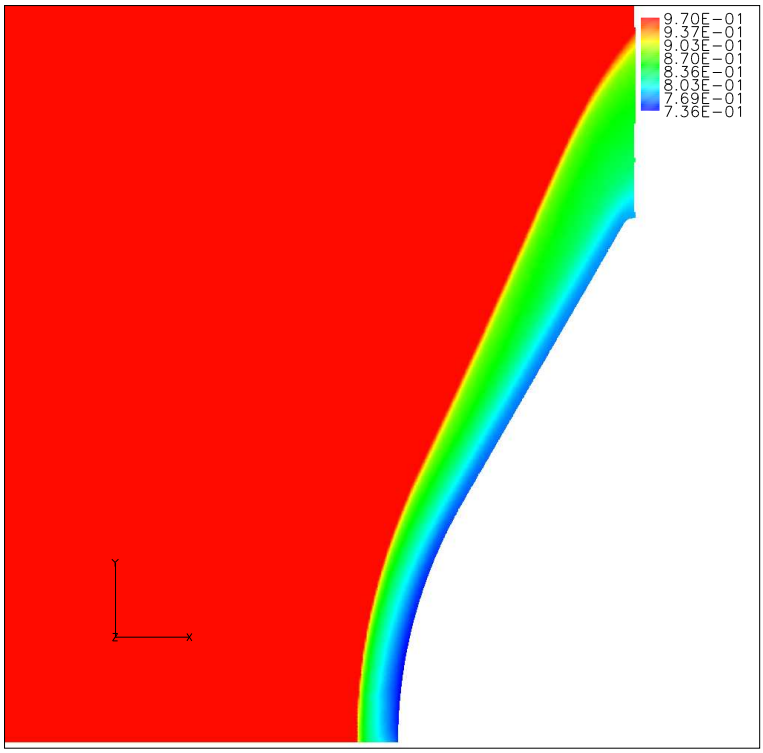

(a) NASCART-GT

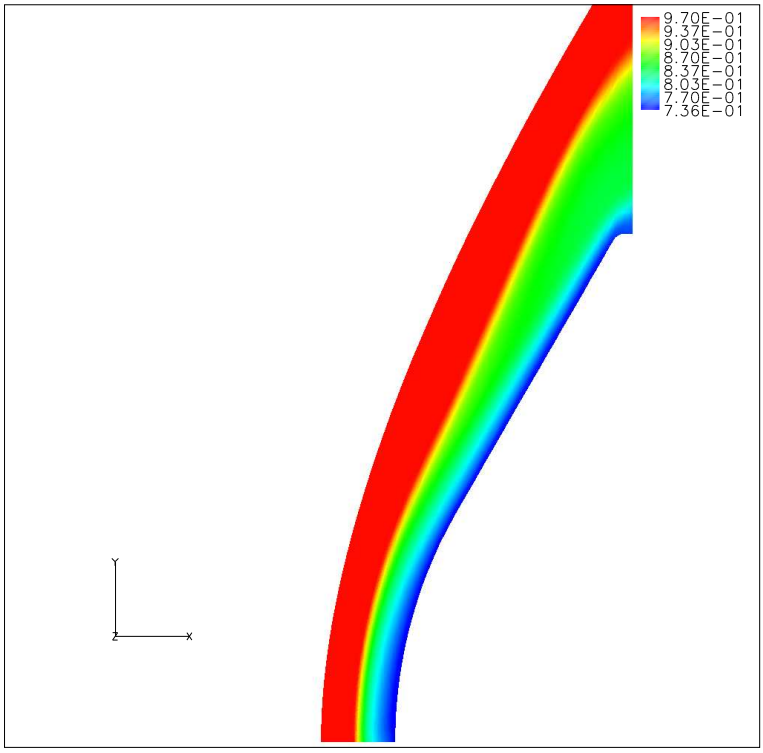

(b) DPLR

Figure 52: N2 mass concentration Contours

(a) NASCART-GT

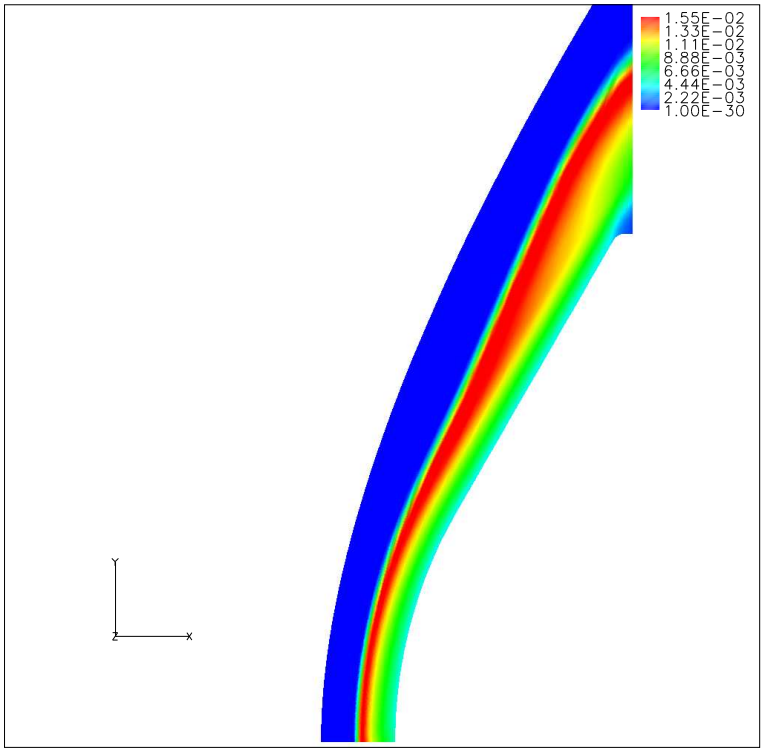

(b) DPLR

Figure 53: CN mass concentration Contours

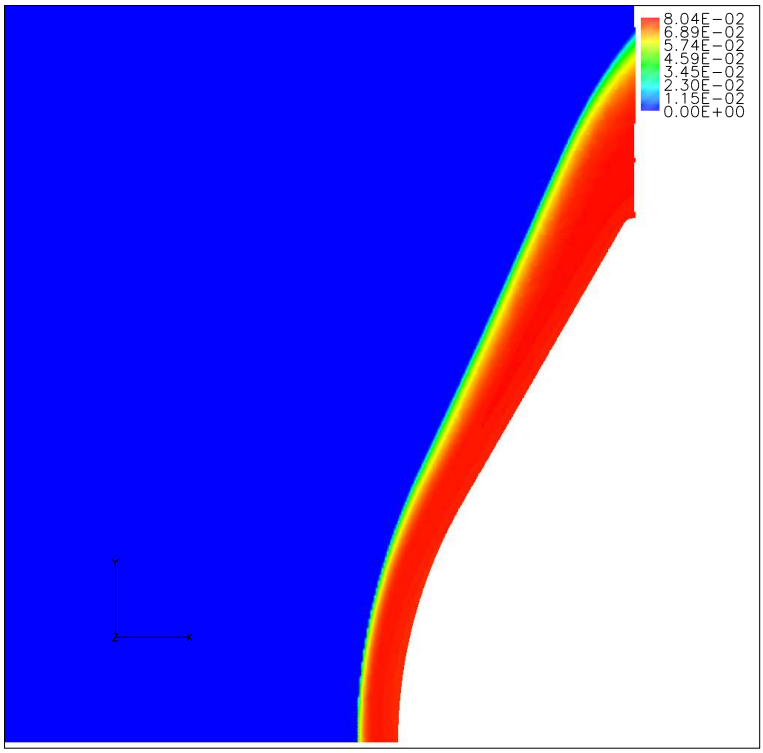

(a) NASCART-GT

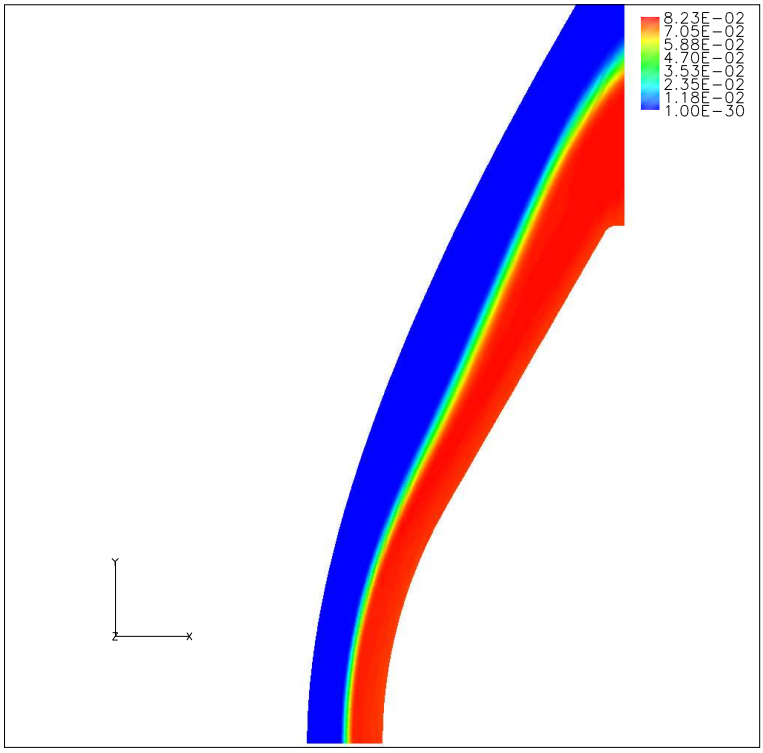

(b) DPLR

Figure 54: H mass concentration Contours

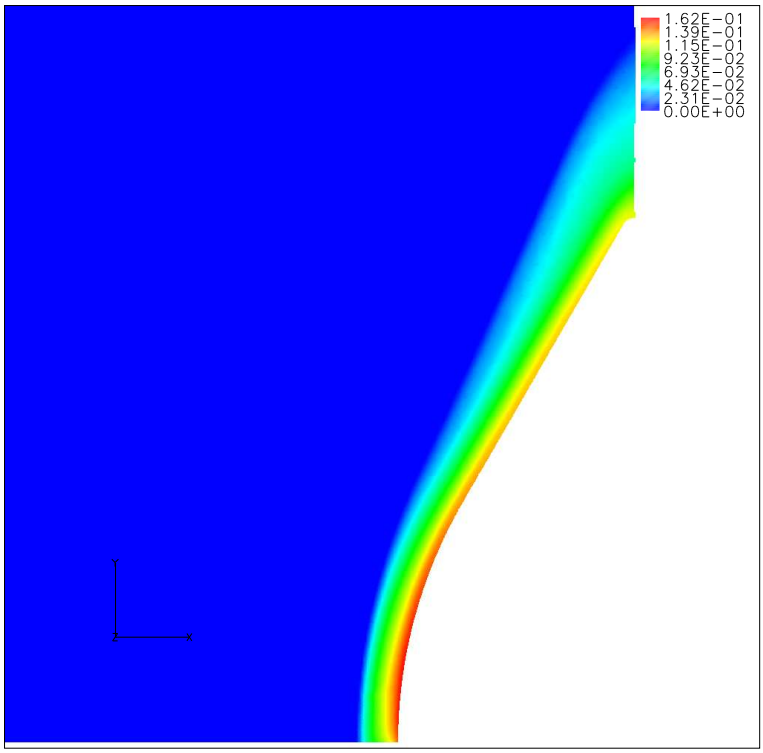

(a) NASCART-GT

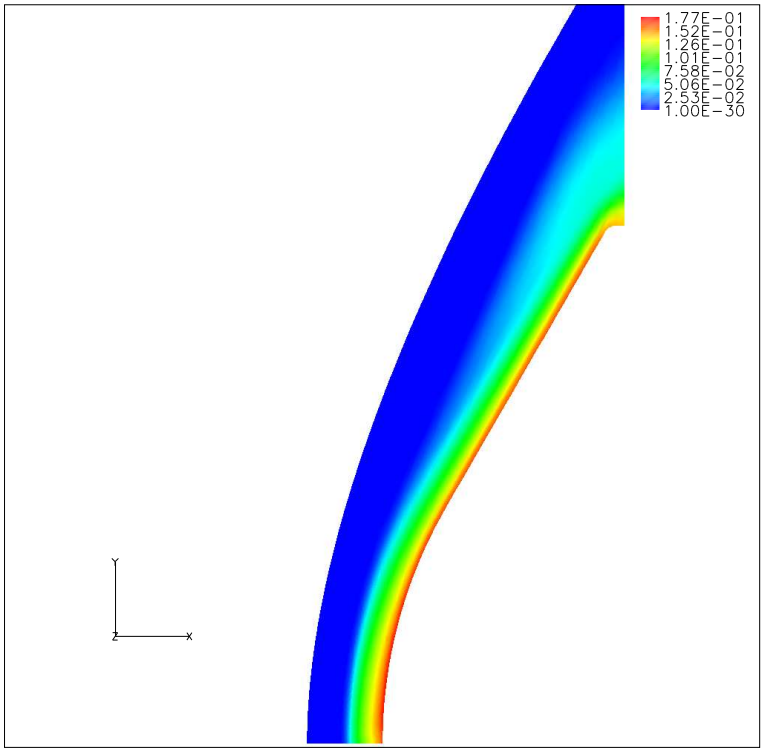

(b) DPLR

Figure 55: N mass concentration Contours

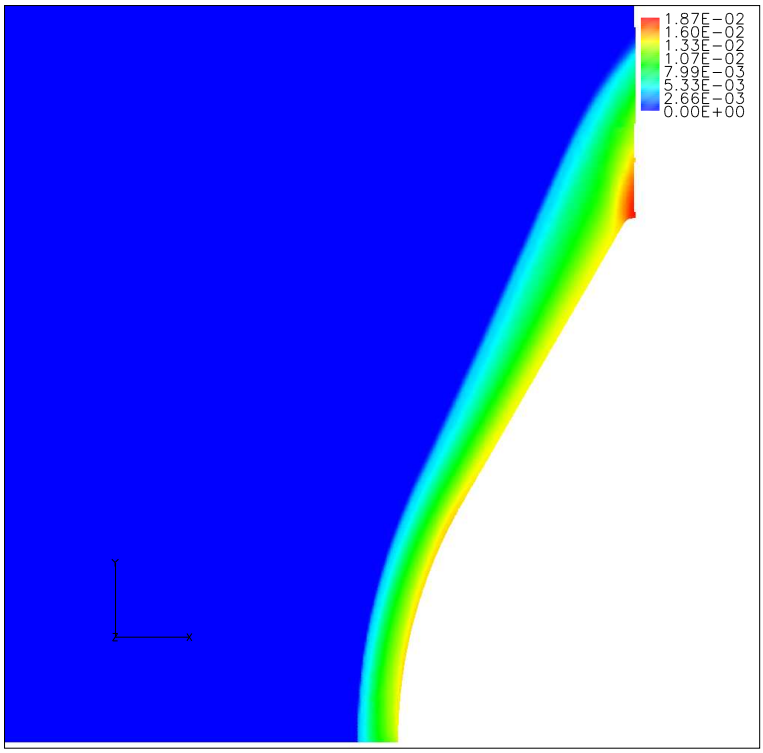

(a) NASCART-GT

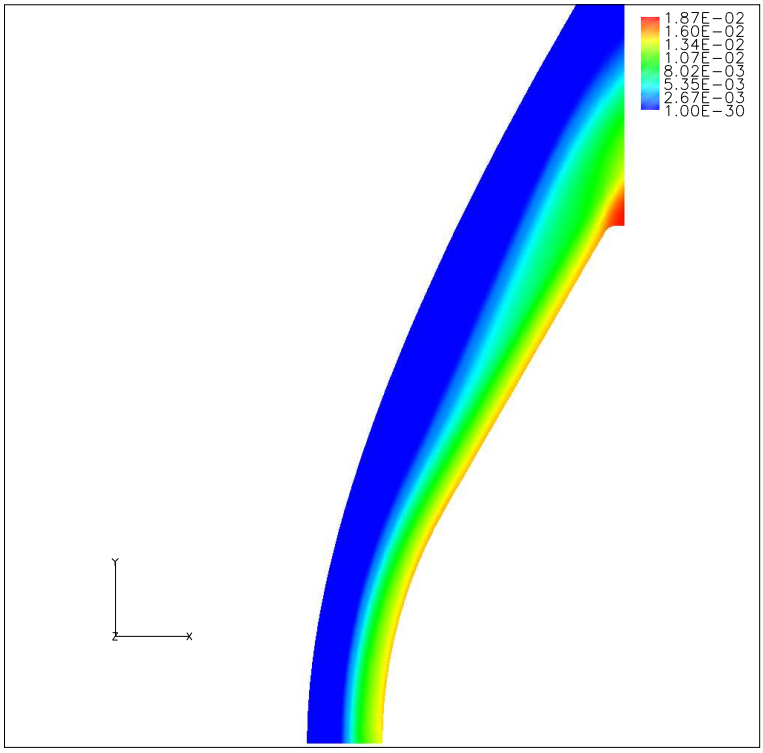

(b) DPLR

Figure 56: C mass concentration Contours

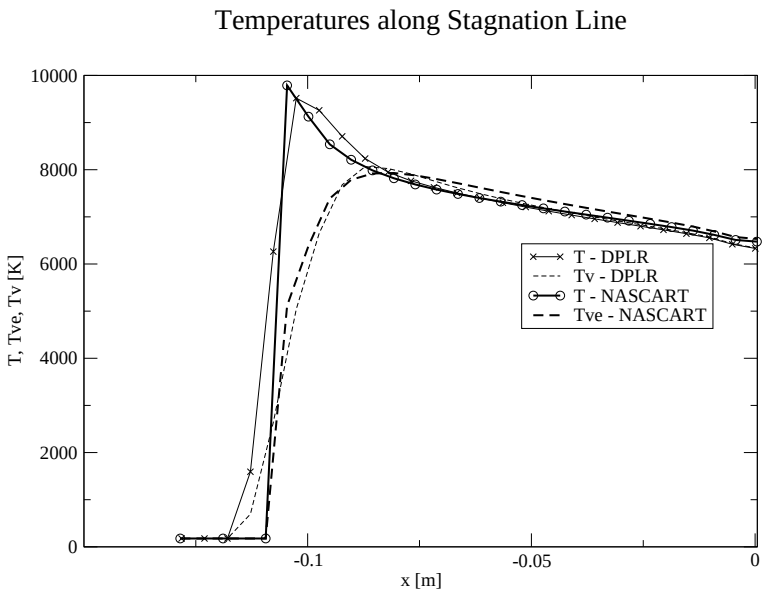

Figure 57: Temperature Distribution along Stagnation Line

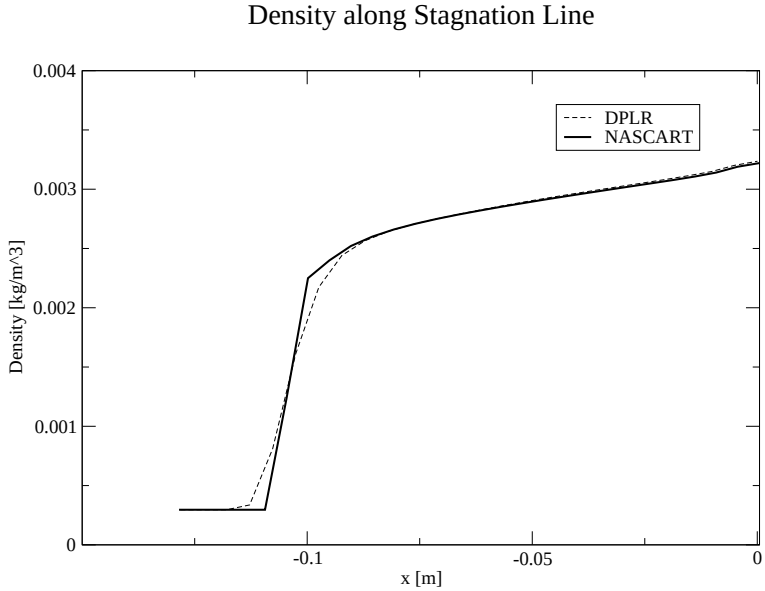

Figure 58: Density Distribution along Stagnation Line

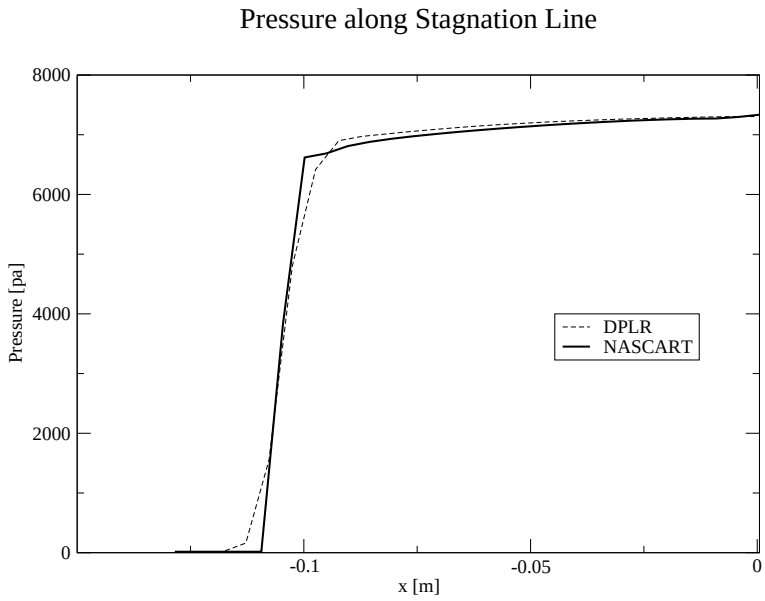

Figure 59: Pressure Distribution along Stagnation Line

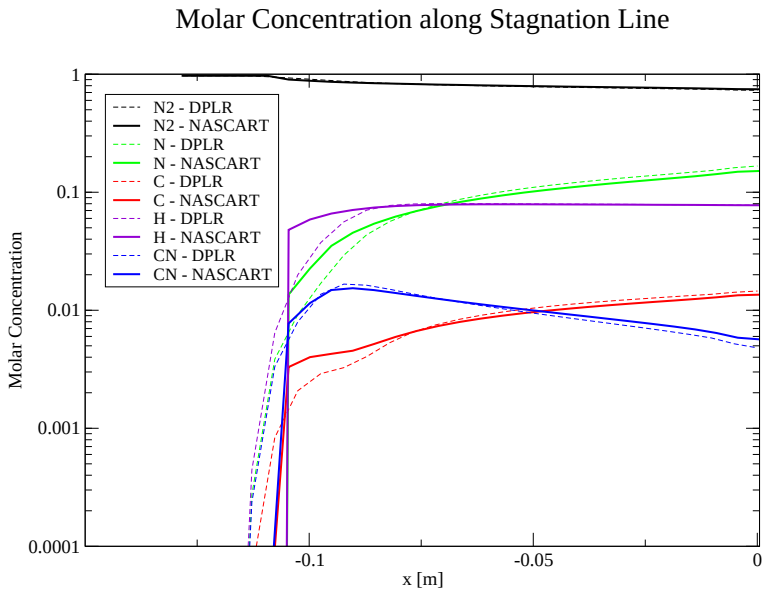

Figure 60: Mass Concentration Distribution along Stagnation Line

5.3 Rapid method for surface heating prediction

A conventional way to predict the heat transfer rate is to fully simulate the viscous region with the Navier-Stokes equations. However, in the conceptual and, perhaps, preliminary design phase, it may be helpful to have a faster (even if more approximate) prediction tool. The present work focuses almost exclusively on inclusion of 3-D inviscid gas dynamics and reacting flow physics necessary for accurate predictions of surface pressure and aerodynamic forces for hypersonic bodies. In this section, an approximate method involving coupling of the inviscid flow analysis with an integral boundary layer method is presented to provide reasonable prediction, including 3-D reacting flow effects in shorter time than a more accurate Navier-Stokes predection.

This method uses the Thwaites laminar integral boundary layer equation [78] corrected for compressible flow to calculate the skin friction using the flow variables at the inviscid wall. The obtained skin friction value is related to the convective heat transfer rate by the Reynolds analogy. Once the convective heat transfer rate is obtained, radiative equilibrium boundary condition is applied to calculate a new convective heat transfer rate and the wall temperature. This rapid analysis method can not include any catalytic response of the wall or the complex nature three dimensional boundary layer flows.

A surface heating prediction was performed on the Huygens probe to demonstrate the present method. The inviscid solution for this case is taken from the 2D axisymmetric Huygens Probe case described in section 5.2.3. Figure 61 and 62 show the convective heat transfer rate and wall temperature comparison with a Navier-Stokes simulation of DPLR. A non-catalytic boundary condition is selected for DPLR. An emissivity value of $\epsilon = 0.85$ is used for the radiative equilibirum boundary condition for both simulations. As can be seen in the figures, the rapid, approximated method gives qualitatively and quantitatively reasonable predictions relative to the verification data. The surface temperature predictions are within roughly 10% of the DPLR

Navier-Stokes results over most of the body. Modification of the procedure would be needed to provide accurate prediction at the stagnation point since the integral boundary layer method is not well defined at such a point.

The very preliminary results shown in Figure 61 and 62 demonstrates that the proposed rapid heat transfer prediction method may be a very useful approach for those seeking rapid aerothermodynamic prediction. More validation and calibration is need for the proposed tool, but such future study is warranted. The skin friction obtained from the integral boundary equation is a function of streamwise velocity gradient. Figure 61 indicates that the rapid heat transfer method is over-sensitive to the streamwise velocity gradient obtained from inviscid solution. The source of this discrepancy is believed to come from the coefficients defined in incompressible Thwaites method, which are needed to be modified to cover highly compressible boundary layer of hypersonic flow.

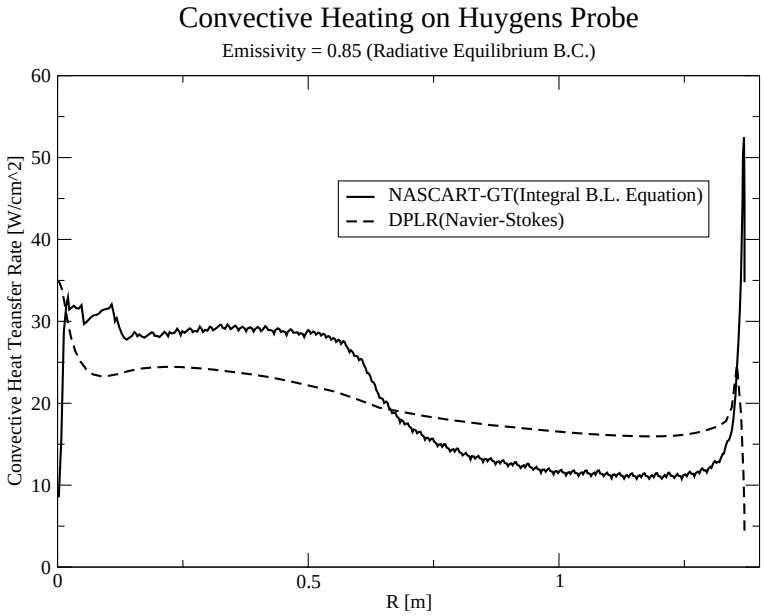

Figure 61: Convective Heating on Huygens Probe

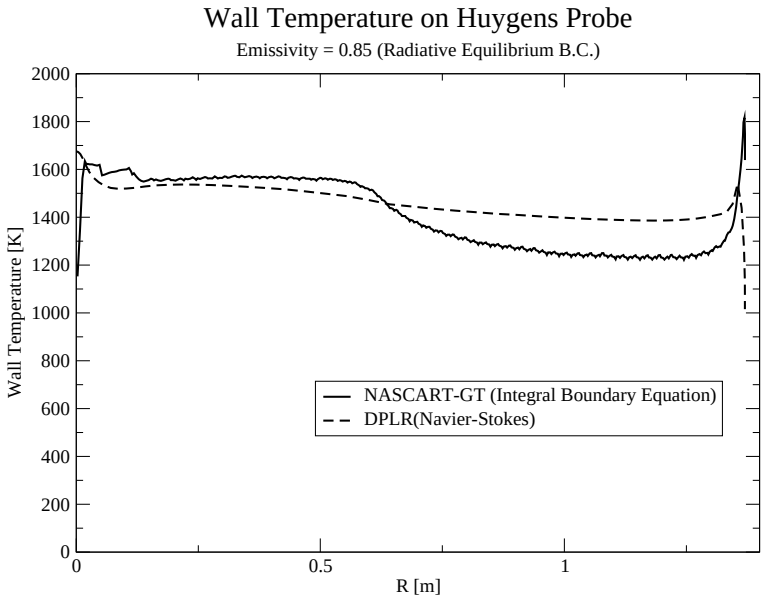

Figure 62: Wall Temperature on Huygens Probe

CHAPTER VI

DOMAIN DECOMPOSITION WITH 3D HILBERT SFC

6.1 Structure of Space Filling Curve

For efficient parallel computing in distributed memory systems, load balancing between different CPUs and minimization of communication time have to be achieved. However, unlike a structured grid, efficient distribution of grids to each CPU is not trivial in the case of an adaptive unstructured grid in a shared memory parallel computing environment. This is because locally clustered cells can be unevenly distributed in the computational domain and the cell numbers are randomly assigned. Therefore, a special consideration is needed to reorganize or precondition the unstructured spatial data prior to parallel computing. In order to achieve the above criteria for efficient parallel computing, 3D Hilbert Space Filling Curve(SFC) is implemented in the current work. This chapter describes the internal structure of the three dimensional Hilbert SFC and how the computational domain is decomposed using the SFC. The Hilbert SFC has a very unique and organized internal structure. The SFC visiting millions of points in 3D space with non-uniform refinement levels might look somewhat complicated but the 3D Hilbert SFC actually has only twenty four base elements (only four for 2D), regardless of how complex the curve is. Each of these twenty four elements has eight nodal points at every turning location of the curve and any of these nodal points can decompose into higher refinement levels. Each nodal point corresponds to a cell center of the Cartesian grid. An important character of this curve is that each of these elements is always refined into the same combinations of sub-elements in the same order. In Figure 64, the basic twenty four elements are shown. The numbers labeled for each element has benn arbitrarily assigned by the

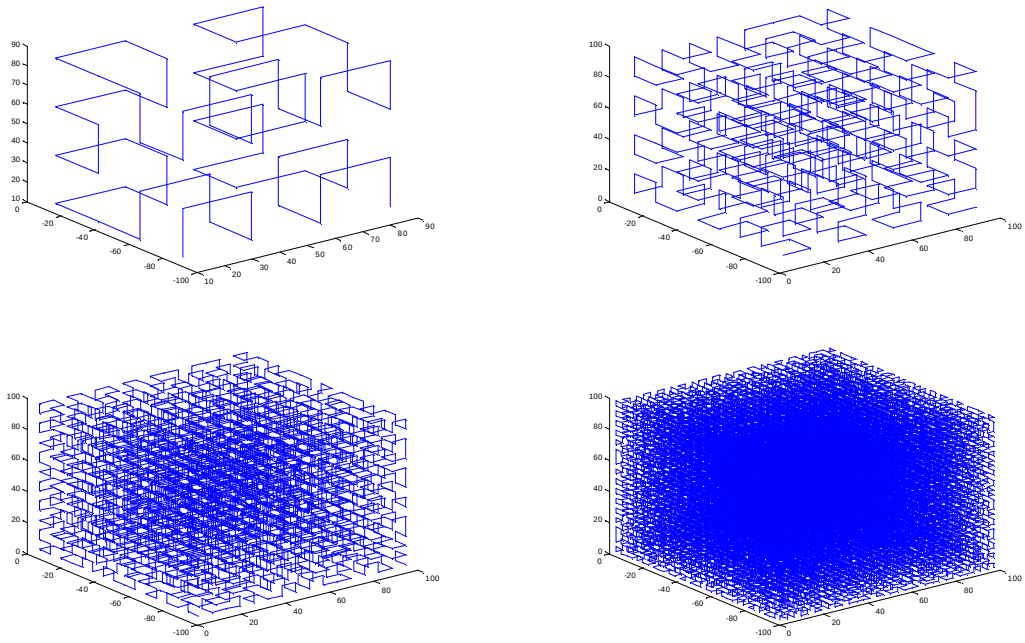

Figure 63: 3D Space-Filling-Curve in Level 2 to 5

author and they may be differently represented in other sources. All elements have the exact same shape and are oriented in four directions for all six faces. The curve within each element has a direction and this direction has to be consistent because the cell numbers are assigned in that order. Table 4 shows its refinement combination and the number corresponding to each element number in figure 64. Using these elements and the refinement order, the 3D SFC can be constructed at multiple levels, as shown in Figure 63.

Once the SFC fills the space, domain decomposition can be performed by simply chopping the curve into even array pieces. The implementing code, NASCART-GT, contains some inactive cells in its array so only the active cells are counted during the array cutting process. As a 2D analog to the 3D curve, Figure 65 shows how a 2D domain is decomposed and evenly distributed to 4 CPUs by cell numbering based on the SFC. Each color represents a CPU index and the numbers inside the cells represent the actual cell numbers in the computational array of the unstructured grid. The cell

numbers written on the cell intersections represent the parent cells in a tree data structure. The parent cells do not participate in computation but are often used for unrefining the grids or for finding neighbor's information. 3D domain decomposition follows the exact same procedure as the 2D example, and the 2D example is shown simply because it is easy to be understood and illustrated.

For the current work, the 3D Hilbert SFC is implemented in the initial grid generation routine, and the grid refinement and unrefinement routines of NASCART-GT. It requires a different method for finding the neighbor pointers and for shifting cell numbers after the refinement/unrefinement process from the previous algorithm. Actually, three neighbor pointers, out of six, can be trivially found by knowing the element number within which the point is located in.

Once the domain is evenly decomposed to the individual CPUs, state vectors of CPU boundary cells should be communicated among the CPUs that share the CPU boundary surface. This communication is performed by using usual MPI routines, and detailed algorithms for the communication will not be discussed in this thesis.

6.2 Destination Cell Flagging Technique

Due to the inherent nature of unstructured grids, where the demarcation for splitting up the domain by the SFC for different CPUs need not involve smooth boundaries, it takes a searching procedure to identify these cells, based on their destination CPUs that they are to communicate with. This process can be somewhat intricate in terms of efficiently managing the computer memory when a communicating cell has multiple destinations such 'A', 'B', 'C', and 'D' cell in Figure 66, which frequently happens in 3D. A simple way of flagging these cells would be by creating a memory slot of the size of the number of communicating cells times the number of communicating CPUs. However, it would waste a lot of available memory. Therefore, the present work suggests a simple technique to avoid this memory wasting problem as its idea

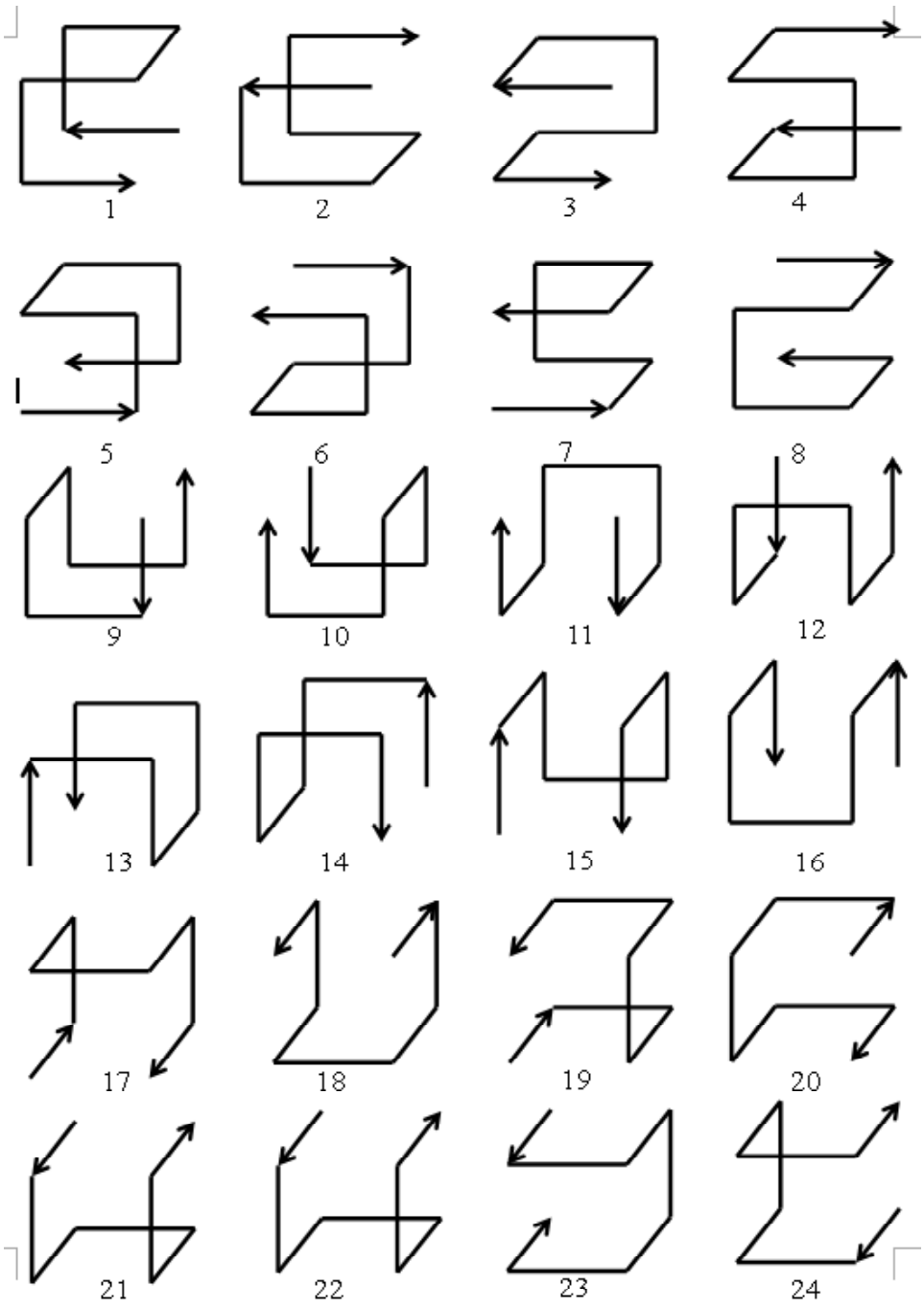

Figure 64: 24 Base Elements of 3D Hilbert Curve

Table 4: Refinement Combination and Order

Parent Element	Child1	Child2	Child3	Child4	Child5	Child6	Child7	Child8
1	16	24	24	10	10	3	3	15
2	11	20	20	13	13	4	4	12
3	18	2	2	23	23	14	14	17
4	21	1	1	19	19	9	9	22
5	15	19	19	9	9	8	8	16
6	12	23	23	14	14	7	7	11
7	17	5	5	24	24	10	10	18
8	22	6	6	20	20	13	13	21
9	3	11	11	5	5	22	22	4
10	8	12	12	1	1	18	18	7
11	20	2	2	21	21	10	10	19
12	23	6	6	17	17	9	9	24
13	7	15	15	2	2	21	21	8
14	4	16	16	6	6	17	17	3
15	19	5	5	22	22	14	14	20
16	24	1	1	18	18	13	13	23
17	13	19	19	12	12	3	3	14
18	9	20	20	16	16	7	7	10
19	5	15	15	4	4	18	18	6
20	2	11	11	8	8	17	17	1
21	14	24	24	11	11	8	8	13
22	10	23	23	15	15	4	4	9
23	6	12	12	3	3	21	21	5
24	1	16	16	7	7	22	22	2

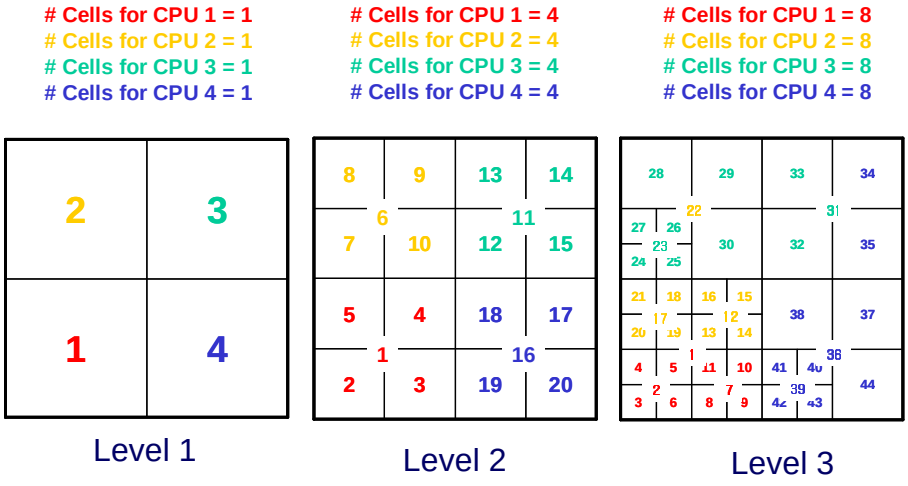

Figure 65: Domain Decomposition Process in 2D

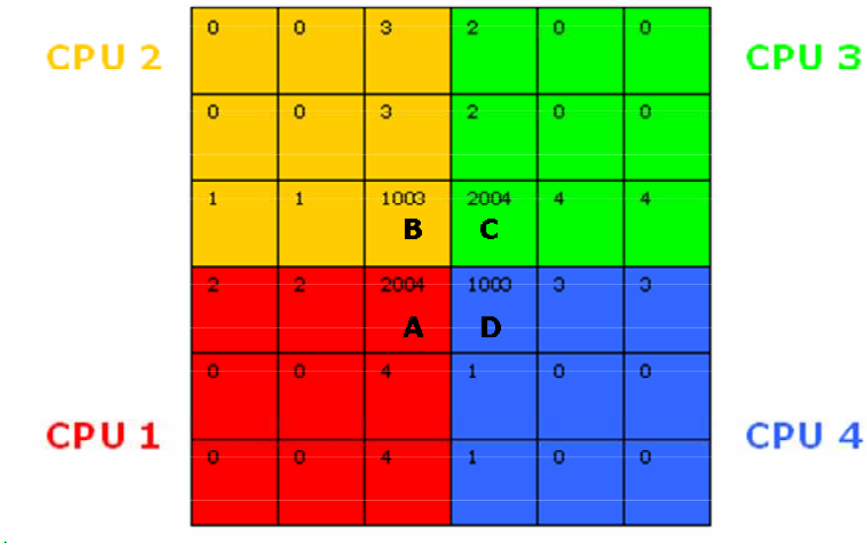

Figure 66: Illustration of Communicating Cell Flagging Technique

is illustrated in Figure 66. In the figure, each color of the domains represents a CPU number, and the number inside of the cells represents the flagging integer to be stored in the memory. If a cell has multiple destinations, it uses three digits for each destination of the FORTRAN long integer data type, which has sixteen digits, so that it can store up to five destinations. As an example, if the state vector information of cell number 1937483 has to be sent to CPU2, CPU13, CPU14, CPU17, and CPU 31, then the representation of this flagging interger would be "2,013,014,017,031". This technique can be flexibly expanded or contracted based on the total number of CPUs available and the size of the problem.

6.3 Results

With the method explained in Chapter 2, the decomposed domains are distributed to multiple CPUs. Figure 67 shows how the domains are distributed to 8 CPUs while performing the solution adaption. Distinct colors in the figures represent the CPU numbers. The example shown in the figures are for a M_∞=1.2 flow over a 3D sphere with a 3 degree angle of attack. Figure 67a is the initial grid at 0 iteration. Figure 67b is the intermediate grid at 4000 iterations after the 39th solution adaption while

developing a bow shock. The figures show that the CPU boundaries dynamically change as the local regions are finely refined due to the solution adaption.

Figure 68 shows the parallelization efficiency results based on the presented domain decomposition method for the case of figure 67. It shows nearly 90% speed up performance without solution adaption, which is consider as typical efficiency in unstructured grid based flow solvers [43] [79]. One sources of the 10% sublinear performance are due to the fact that surface boundary cells require somewhat more computational time than regular flow cells to enforce boundary condition in Cartesian boundary formulations. The speed up results with solution adaption show only 57% parallel efficiency. This is expected because the current thesis work does not include the parallelization of solution adaption scheme and grid generation.

The sample parallel speed-up results were run on a cluster with 16 AMD Opteron 248 processor with 1MB L2 cache.

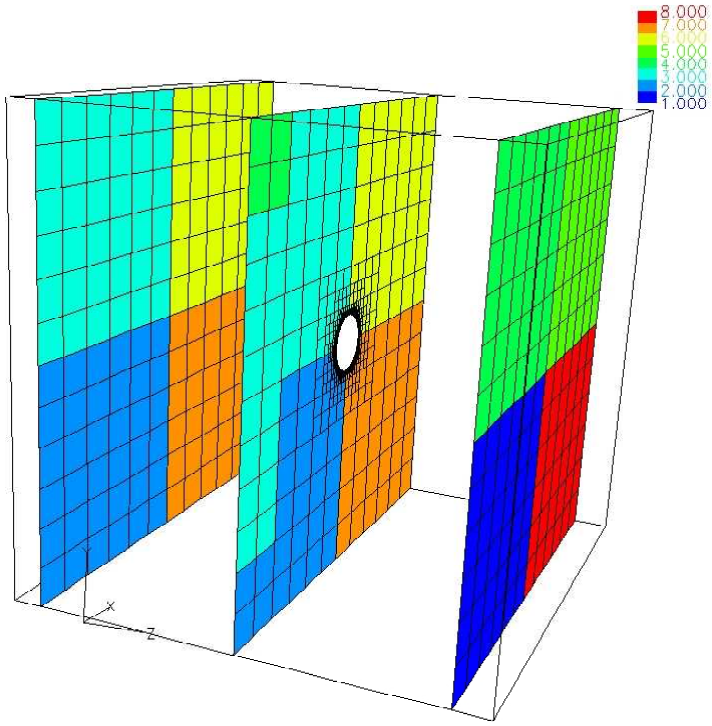

(a) a. Initial Grid

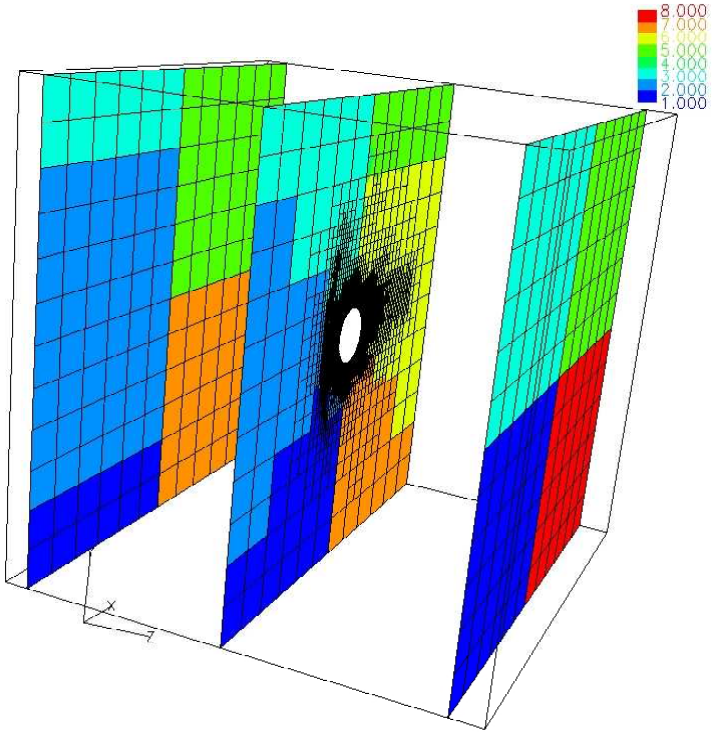

(b) b. Grid after 39th solution adaption

Figure 67: NASCART-GT 3D Decomposition of Solution adapted Grid over 3D Sphere

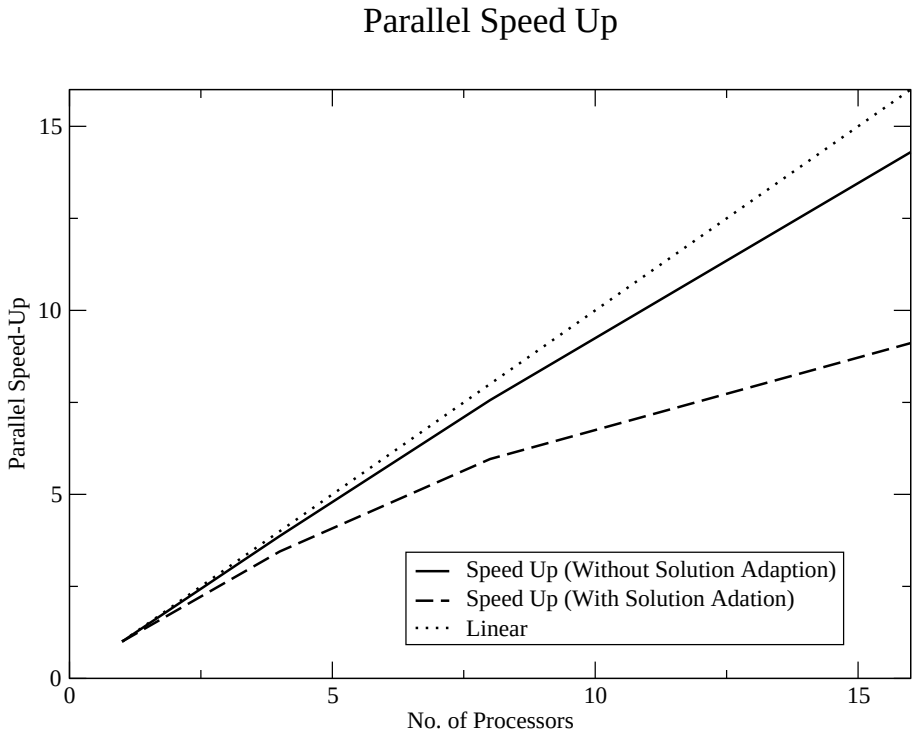

Figure 68: Current Parallel Speed Up vs. No. of CPUs †

CHAPTER VII

HYPERSONIC FLOW ANALYSIS OF BALLUTE

Hypersonic flow analysis of a clamped ballute in Titan's aerocapture mission is described in this section using the present development of the thermochemical nonequilibrium solver and the parallelization of unstructured Cartesian grids. In particular, the flow properties within the shock layer and the surface pressure at the peak dynamic pressure have been selected for the focus of analysis. Also, the deformation of the ballute has been considered for the realistic flow analysis by synthesizing the preceding ballute aeroelastic analysis [2].

7.1 Mission Description

The Titan's aerocapture mission and its trajectory using a ballute have been rigorously described in Westhelle and Masciarelli [80], James et al. [81], Miller et al.[33] [82], Johnson and Lyons [83], and Brown and Richardson [84]. Two reference trajectories, steep and shallow, have been defined for the clamped ballute configuration. For the current work, the steep trajectory has been selected because it produces a more intense flow environment around the ballute, and also since the results of the current work could be compared to the preceding perfect gas results by Rohrschneider [2].

Along the mission trajectory, the ballute is deployed at an interface of atmospheric entry at the altitude of 1000 km from Titan's surface with an entry velocity of 6.51 km/sec. The inertial flight path angle at this point is -31.93 degree. The ballute free-falls within the free molecular regime. Then, it slowly gets decelerated as it passes through the transitional regime. At this stage, shock waves form and the ballute experiences moderate thermal and mechanical loads on its surface. When the ballute

reaches the continuum regime, the shock wave becomes much stronger. Its thermal and mechanical loads reach the maximum when it attains the peak dynamic pressure of 44.5 Pa at an altitude of 530.8 km. At this trajectory point, a velocity of 4.266 km/sec, density of $5.663E-06kg/m^3$, temperature of 166 k, pressure of 2.733E-01 pa, and the local speed of sound of 259.9 m/sec define the freestream conditions. The Knudsen number at this point is 2.69E-03, which falls into the continuum regime. The atmospheric chemical composition at this altitude is 89.71% Nitrogen, 1.09% Methane, and 9.2% Argon.

7.2 Ballute Configuration and Structural Consideration

The clamped ballute proposed for the analysis, shown in Figure 69 is a 60 degree blunted cone with a 1.73 m minor radius torus. The total radius of the ballute, when undeformed, is 13.83 m. The inner radial part of the cone is made out of a 3.556E-4 m thick Nextel 312 AF-10 ceramic fabric, made by 3M, from the spacecraft attach point to 6.1m along the radial direction. The remaining part of the ballute is made out of Upilex polyimide film, made by DUPONT, 5.08E-5 m thick for the rest of the cone and 3.4E-4 m thick for the torus. The inflating gas is at a pressure of 2000 pa to avoid radial buckling. The average material temperature at the peak dynamic pressure point along the trajectory is estimated to be 228^oC using radiation and environment modeling tools: Thermal Synthesizer System (TSS) software, and Thermal Analysis Kit 2000 (TAK 2000). The solar absorptivity and IR emissivity are assumed to be $\alpha = 0.83$ and $\epsilon = 0.85$ respectably. And the inflating gas used for this analysis is GN_2, whose thermal conductivity is $K = 0.0446W/(mK)$. The material properties at this temperature are listed in Table 5.

For the realistic hypersonic analysis, the deformation of the ballute due to hypersonic pressure has been simulated by a structural dynamics tool LS-DYNA[85]. Since the feasibility study of LS-DYNA and its validation on an inflated column and an

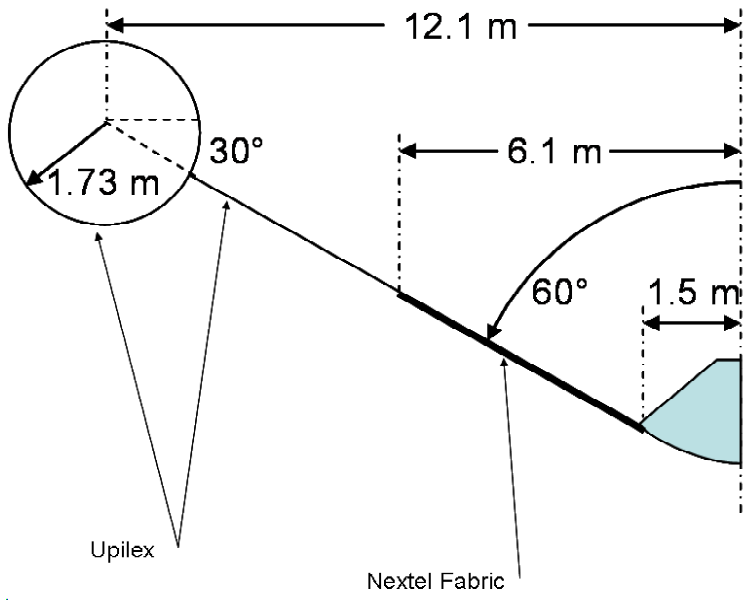

Figure 69: Axis Symmetric Profile of Undeformed Clamped Ballute [2]

Table 5: Material Property at Peak Dynamic Pressure Point

Material:	Upilex	Nextel
Modulus[Gpa]	3.883	7.00
Poisson Ratio	0.34	0.20

inflated torus already have been performed in the preceding analysis[2], those have not been repeated in the present work. The pressure feedback from the flow solver is transferred to the structural dynamics solver as the load input. And the deformation feedback from the structural dynamics solver is transferred to the flow solver. This loose coupling process is repeated until the static ballute's deformation has been obtained. The data transfer between LS-DYNA and the present flow solver was done via BAAT (Ballute Aeroelastic Analysis Tool) [2]. Figure 70 shows the iteration history in terms of the torus' leading edge displacement and it has converged at the 5th coupling iteration.

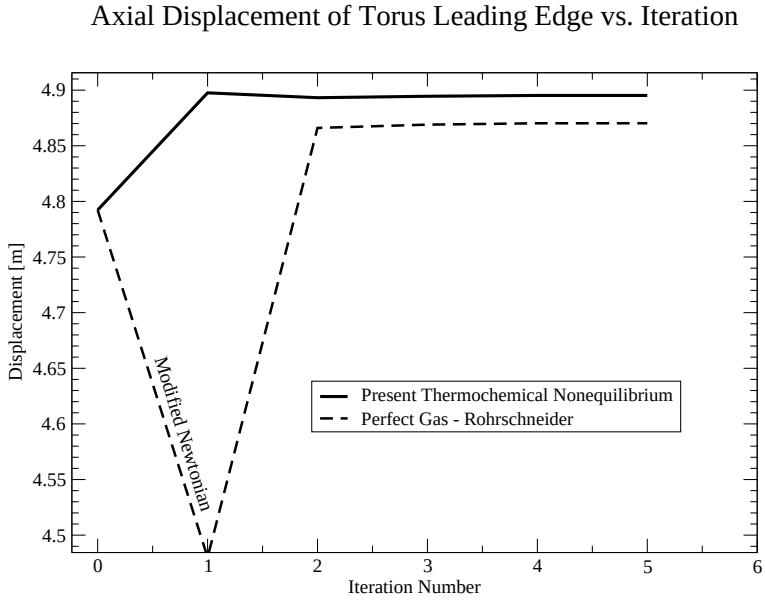

Figure 70: Displacement Convergence History at Flow-Structure Coupling Iteration

7.3 Ballute Hypersonic Flow Analysis

Hypersonic flow analysis was performed on a quarter model of the clamped ballute. Only the front side was simulated to avoid numerical challenges in computing the inviscid vacuum zone on the lee side. A total of 187,043 cells were used with solution adaption set up with amaxd = 1.0, amind = 0.2, amaxc = 1.0, and aminc = 0.4. The input parameters, amaxd and amind, are the solution adaption parameters for velocity divergence, and amaxc and aminc are those for species gradient. The solution adaption was performed every 100 iterations. A total of thirteen species (N_2, CH_4, Ar, N, C, C_2, CH, CH_2, CH_3, H, H_2, CN, and NH) were used for this simulation and the forward reaction rates were taken from Gökçen [66]. Figure 71 shows the grid and the flow pattern around the ballute. As desired, no shock-shock interaction is observed between the 60 degree cone and the torus, instead one large bow shock over the ballute is formed. Figures 72 to 76 show the flow properties around and on the surface of the ballute. The peak surface temperature outside of the thermal boundary layer is 7870K and it is located at the stagnation point. Its peak pressure points, 109Pa, and the peak density point, 5.13E-5kg/m^3, occur at the inner corner of

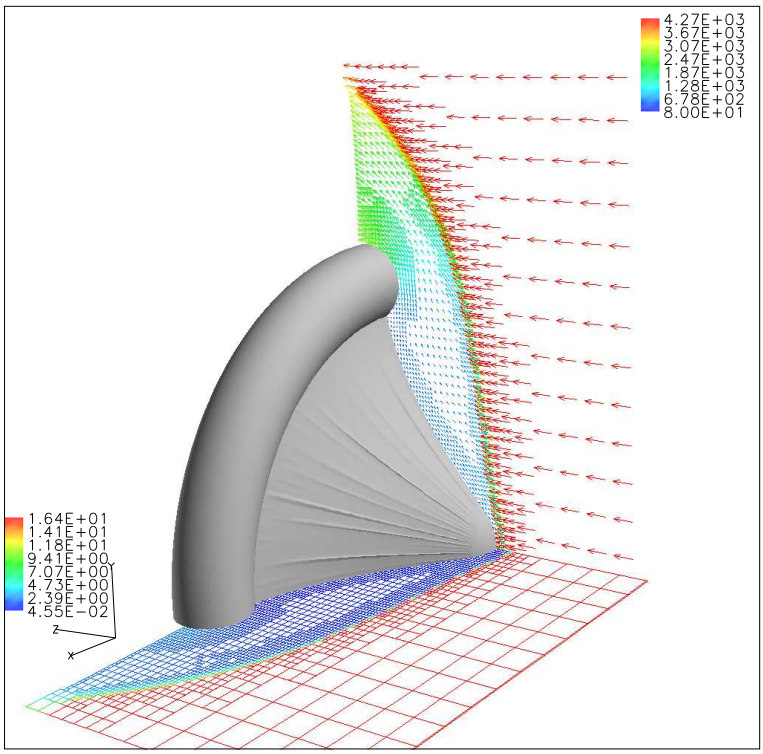

Figure 71: Grids over a clamped ballute, X-plane: Velocity Magnitude, Y-plane: Mach Number

the torus. The major species, N_2, gets dissociated gradually as it passes through the shock wave and its maximum dissociation of 8.25% by volume occurs near the torus. Most of the hydrocarbon species (CH_4,CH_3,CH_2,CH) get dissociated immediately after the shock wave due to their low activation energies. Therefore, only species like C, H, Ar, N_2, N are present as the major species near the surface except in the nose region. At the nose, the flow is in vibrational and chemical nonequilibrium as it can be seen from the figures. Figures 77 and 78 show the convective heating value and wall temperature at X-symmetry plane using the rapid aerothermodynamic prediction described in Section-5.2.3.1. Emissivity of $\epsilon = 0.85$ is also used for emissivity in this case.

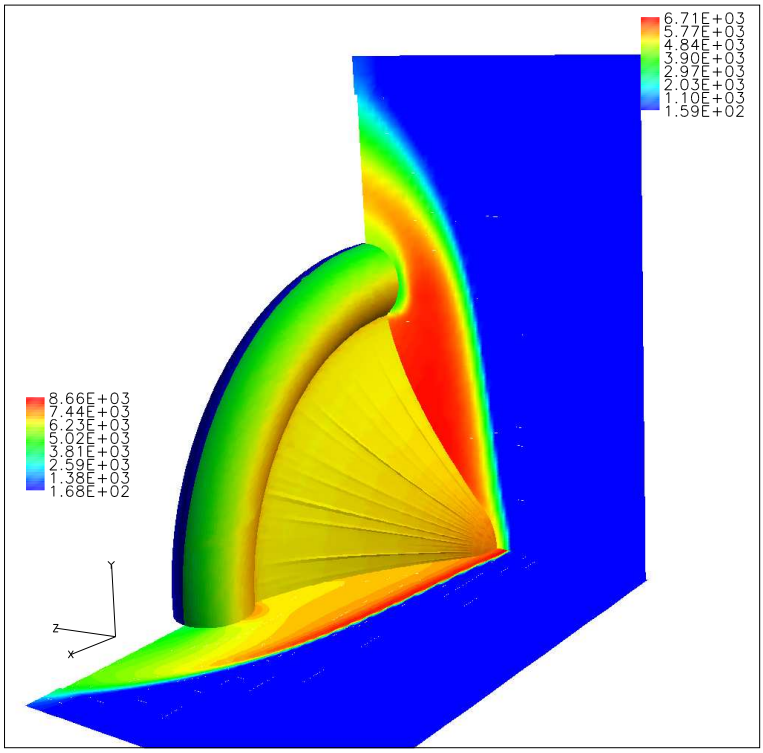

Figure 72: Translational Temperature and Vibrational-Electronic Temperature Contour, X-plane: V.E. Temp. and Y-plane and surface: Translational Temperature

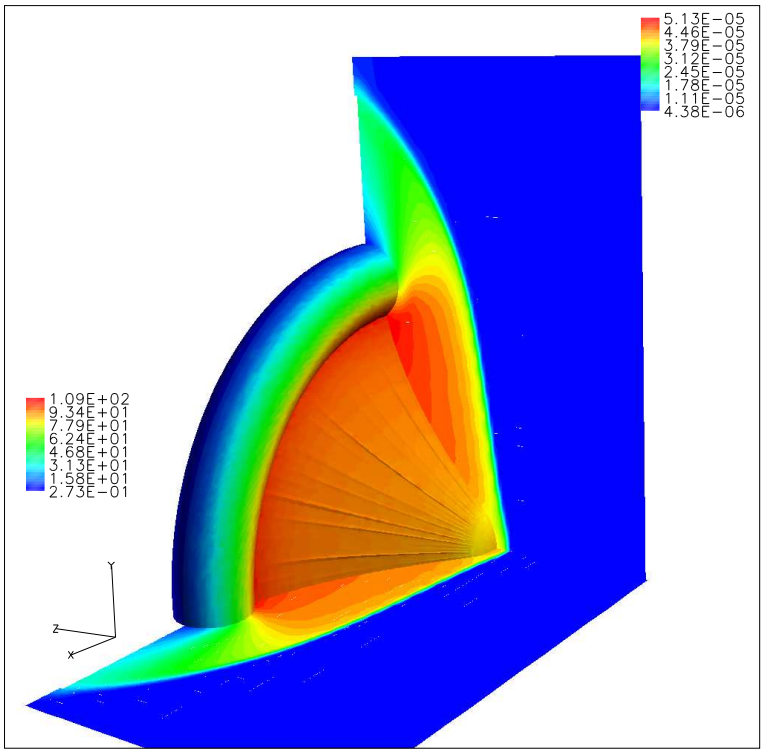

Figure 73: Pressure and Density Contour, X-plane: Density and Y-plane and surface: Pressure

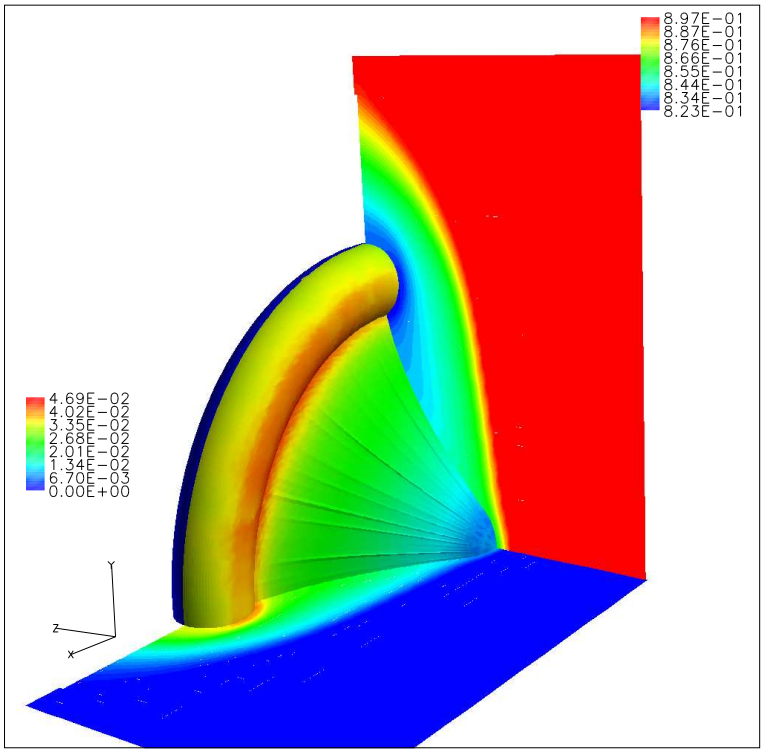

Figure 74: N2 and N Mole Fraction Contours, X-plane: N2 and Y-plane and surface: N

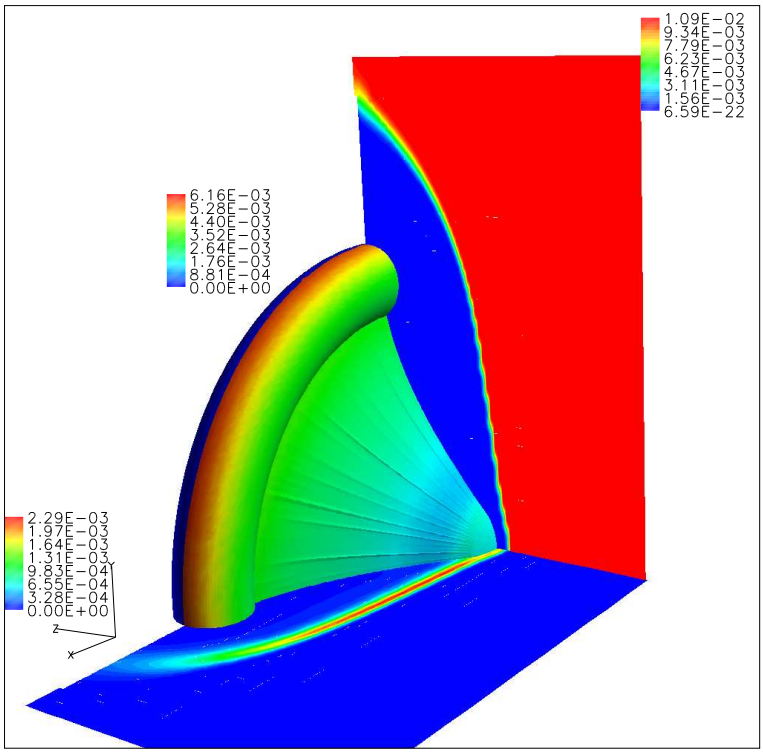

Figure 75: CH4, CH and C Mole Fraction Contours, X-plane: CH4, Y-plane: CH and surface: C

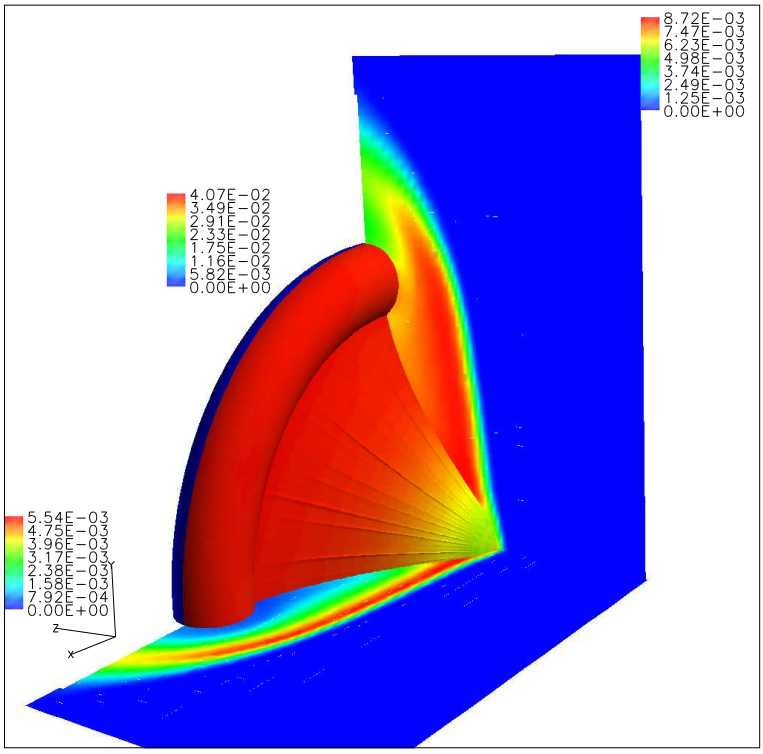

Figure 76: CN, H2 and H Mole Fraction Contours, X-plane: CN, Y-plane: H2 and surface: H

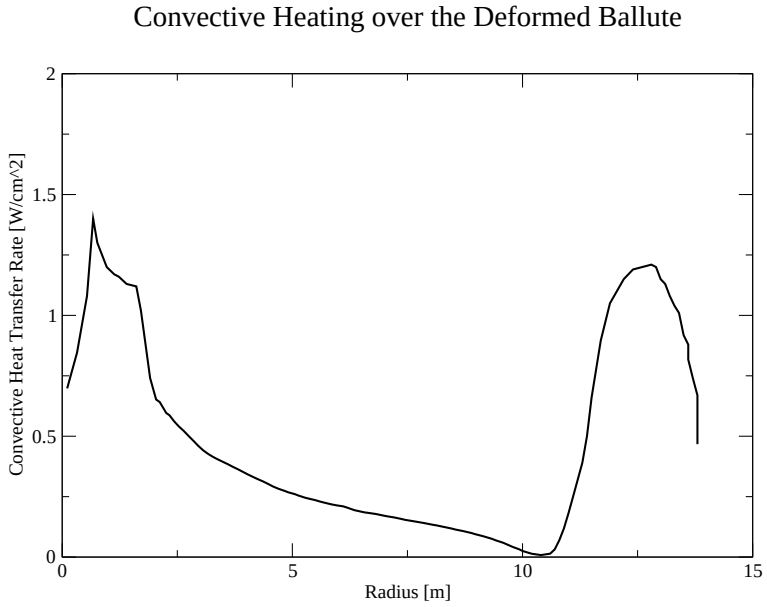

Figure 77: Convective Heating from Rapid Aerothemal Analysis Formulations

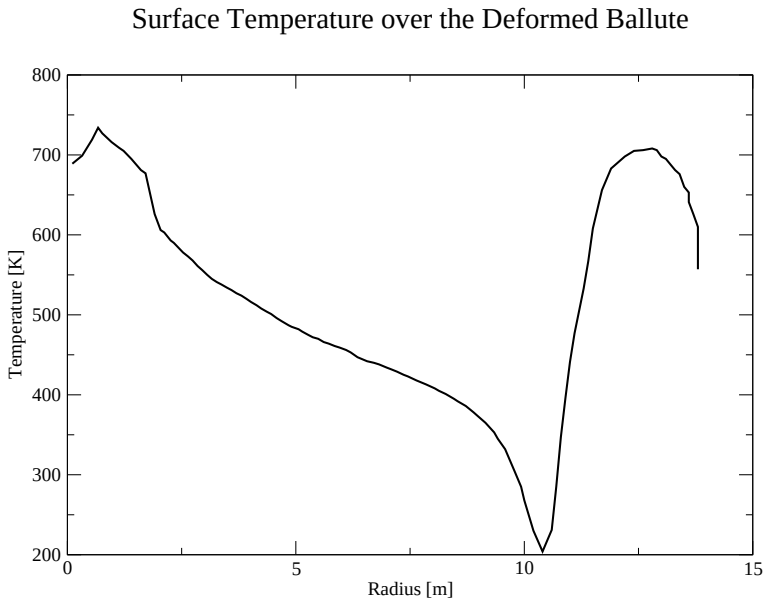

Figure 78: Wall Temperature from Rapid Aerothemal Analysis Formulations

CHAPTER VIII

CONCLUSION AND RECOMMENDATION

The parallelization work was initially developed from the scalar version of NASCART-GT. The 3D version of the Hilbert SFC was first implemented in the grid generation, refinement, and unrefinement routines of the code. Then, an algorithm for identifying the communicating cells was deviced, and these identified cells were flagged and grouped in terms of their destination CPUs. Communication to pass on the state vector information was programmed using the MPI library. As expected, the domain decomposition strategy using the 3D Hilbert Space Filling Curve (SFC) provided evenly distributed and block contiguous grid partitioning and showed 90% efficient parallel speed up. The additional time to enforce boundary condition in Cartesian boundary formulations resulted in 10% sub-linear performance. This sub-linear performance can be improved by weighting more time to the boundary cells, rather than simply dividing the domain based on the same number of cells. The master CPU redistributed the work load to each CPU after solution adaption so that load balancing is still maintained. However, the grid generation part of NASCART-GT including the grid refinement routine was not parallelized in this thesis work. Therefore, it showed sub-linear speed-up performance with the solution adaption turned on, but the one without solution adaption showed an almost linear speed-up. The recommendation for future work would be to parallelize the grid generation process to achieve a linear speed-up, even with the solution adaption turned on.

The nonequilibrium flow solver development was started from the calorically perfect gas code. The chemical nonequilibrium solver was developed as an initial effort

by adding the species equations and thermodynamic routines that define a thermally perfect gas. Then, vibrational nonequilibrium was added to compute the two-temperature thermochemical nonequilibrium part. The credibility of this work was verified against DPLR (NASA Ames' structured grid nonequilibrium flow solver). In general, the present nonequilibrium solver agreed well with the verification code. As expected, the AUSMPW+ scheme with MUSCL data reconstruction effectively resolved the stiff gradients at the shock wave, and the point implicitly treated chemical source terms did not degrade the existing CFL constraints of the explicit solver. Future recommendation for this work would be to expand it to treat hypersonic viscous flows and to add radiation effects to quantify convective and radiative heat transfer rates.

As an application of the above two topics, hypersonic flow analysis on a clamped ballute was performed. In this work, nonequilibrium flow solution was loosely coupled with an existing structural dynamics code, LS-DYNA, to model the flexible nature of the ballute surface definition. This structural coupling work was performed by synthesizing the preceding ballute aeroelastic analysis [2]. Finally, a rapid aerothermodynamic analysis was performed to calculate the convective heat transfer rate and the wall temperature. Future recommendation for this work would be to apply temperature dependent material properties to each panel in the structure model.

This thesis work, from the state-of-the-art point of view, suggests the unstructured Cartesian grid methodology for the analysis of flexible hypersonic objects, such as ballutes, by advancing the existing capabilities. Such analysis requires repeating grid generations and interactions with multidisciplinary tools. This thesis work demonstrates several advantages of the unstructured Cartesian grids in those kinds of analyses by involving minimal user intervention. This thesis work also provides a strong foundation to develop an unstructured grid based hypersonic aerothermodynamics tool, which is an unsolved task to today's CFD engineers.

REFERENCES

[1] Anderson, B. P., "Computational Continuum and Rarefied Flow Results For Ballute Applications," *AIAA Paper 2004–292*, Jan 2004.

[2] Rohrschneider, R. R., *Variable-Fidelity Hypersonic Aeroelastic Analysis of Thin-Film Ballutes for Aerocapture*, Ph.D. thesis, Georgia Institute of Technogy, 2005.

[3] Hornung, H. G., "Hypersonic Flow over Bodies in Tandem and Its Relevance to Ballute Design," *AIAA Paper 2001–2776*, Jun 2001.

[4] Howe, J. T., "Hypervelocity atmospheric flight: Real gas flow fields," Technical Memorandum 101055, NASA, 1989.

[5] Gupta, R. N., Yos, J. M., Thompson, R. A., and Lee, K. P., "A Review of Reaction Rates and Thermodynamic and Transport Properties for an 11-species Air Model for Chemcial and Thermal Nonequilibrium Calculation to 30,000k," *NASA Reference Publication 1232*, 1990.

[6] Aftosmis, M. J. and Baron, J. R., "Adaptive Grid Embedding in Nonequilibrium Hypersonic Flow," *AIAA Paper 89–1652*, Jun 1989.

[7] Gnoffo, P. A. and White, J. A., "Computational Aerothermodunamic Simulation Issues on Unstructured Grids," *AIAA Paper 2004–2371*, Jun 2004.

[8] Nompelis, I., Drayna, T. W., and Candler, G. V., "Development of a Hybrid Unstructured Implicit Solver for the Simulation of Reacting Flows Over Complex Geometries," *AIAA Paper 2004–2227*, Jun 2004.

[9] Tu, S., *Development of A Solution Adaptive Cartesian-Grid Solver for 2-D Thermochemical Nonequilibrium Flows*, Ph.D. thesis, Georgia Institute of Technogy, 2001.

[10] Karypis, G. and Kumar, V., "Analysis of multilevel graph partitioning," Technical Report TR 95-037, Department of Computer Science, University of Minnesota, 1995, Also available on WWW at URL http://www.cs.umn.edu/users/kumar/papers/mlevel analysis.ps.

[11] Moon, B, Jagadish, H. V., Faloutsos, C., and Saltz, J. H., "Analysis of the Clustering Properties of the Hilbert Space-Filling Curve," *IEEE Transactions on Knowledge and Data Engineering*, Vol. 12, No. 1, Jan 2001.

[12] Wright, M. J., Hollis, B. R., Bose, D., and Walpot, L., "Post-Flight Aerothermal Analysis OF Huygens Probe," .

[13] Kayser, L., "Pressure Distribution, Heat Transfer, and Drag Tests on the Goodyear Ballute," Tech. Rep. AEDC-TDR-62-39, Arnold Air Force Station, March 1962.

[14] London, H., "Change of Satellite Orbit Plane by Aerodynamic Maneuvering," *Journal of the Aerospace Sciences*, Vol. 29, No. 3, 1961, pp. 323–332.

[15] Walberg, G., "A Survey of Aeroassisted Orbit Transfer," *Journal of Spacecraft and Rockets*, Vol. 22, No. 1, 1985, pp. 3–18.

[16] Hall, J. and Le, A., "Aerocapture Trajectories for Spacecraft with Large, Towed Ballutes," *Advances in the Astronautical Sciences*, Vol. 108 II, Univelt Inc., San Diego, CA, 2001, pp. 1857–1872.

[17] Lockwood, M. K., "TITAN AEROCAPTURE SYSTEMS ANALYSIS," *AIAA Paper 2003–4655*, 2003.

[18] Gnoffo, P. A., "Computational Aerothermodynamics in Aeroassist Applications," *AIAA Paper 2001–2632*, June 2001.

[19] Rasheed, A, Fufii, k, and Hornung, H. G., "Experimental Investigation of the Flow over a Toroidal Aerocapture Ballute," *AIAA Paper 2001–2460*, Jun 2001.

[20] Moss, J., "DSMC Simulations of Ballute Aerothermodynamics Under Hypersonic Rarefied Conditions," *AIAA Paper 2005–4949*, 2005.

[21] Masciarelli, J. P., Lin, J. K. H., Ware, J. S., Rohrschneider, R. R., Braun, R. D., Bartels, R. E., Moses, R. W., and Hall, J. L., "Ultra Lightweight Ballutes for Return to Earth from the Moon," *AIAA Paper 2006–1698*, 2006.

[22] Gnoffo, P. A., Buck, G., Moss, J., Nielsen, E., Berger, K., Jonesk, W. T., and Rudavsky, R., "Aerothermodynamic Analyses of Towed Ballutes," *AIAA Paper 2006–3771*, Jun 2006.

[23] Coirier, W., *An adaptive-Refined, Cartesian, Cell-Based Scheme for the Euler and Navier-Stokes Equations*, Ph.D. thesis, University of Michigan, Ann Arbor, MI, 1993.

[24] Coirier, W., "An adaptive-Refined, Cartesian, Cell-Based Scheme for the Euler and Navier-Stokes Equations," Technical Memorandum 106754, NASA Lewis Research Center, Cleveland, OH, 1994.

[25] Lee, J., *Development of An Efficient Viscous Approach in A Cartesian Grid Framework and Application to Rotor-Fuselage Interaction*, Ph.D. thesis, Georgia Institute of Technogy, 2006.

[26] Marshall, D. D., *Extending the Functionalities of Cartesian Grid Solvers: Viscous Effects Modeling and MPI Parallelization*, Ph.D. thesis, Georgia Institute of Technogy, 2002.

[27] Udaykumar, H. S., "Multiphase Dynamics in Arbitrary Geometries on Fixed Cartesian Grids," *Journal of Computational Physics*, Vol. 137, 1997, pp. 366–405.

[28] Udaykumar, H. S., "A Sharp Interface Cartesian Grid Method for Simulating Flow with Complex Moving Boundary," *Journal of Computational Physics*, Vol. 174, 2001, pp. 345–380.

[29] Tseng, Y and Ferziger, J. H., "A Ghost-Cell Immersed Boundary Method for Flow in Complex Geometry," *Journal of Computational Physics*, Vol. 192, 2003, pp. 593–623.

[30] Anderson Jr., J. D., *Hypersonic and High Temperature Gas Dynamics*, McGraw-Hill, 1998.

[31] Vincenti, W. G. and Kruger Jr, C. H., *Introduction to Physical Gas Dynamics*, Krieger Publishing Co., INC., 1967.

[32] Mannella, G. G., "Chemical Reactions in Electrical Plasmas," *The OHIO Journal of Science*, Vol. 66, No. 3, May 1966.

[33] Miller, K. L., Gulick, D., Lewis, J., and Trochman, B., "Trailing Ballute Aerocapture: Concept and Feasibility Assessment," *AIAA Paper 2003–4655*, Jul 2003.

[34] Wright, M. J., Olejniczak, J., Walpot, L., Raynaud, E., Magin, T., and andHollis, B. R., C., "A Code Calibration Study for Huygens Entry Aeroheating," .

[35] Gnoffo, P. A., Mccandless, R. S., and Yee, H. C., "Enhancements to Program LAURA for computation of three-dimensional hypersonic flow," *AIAA Paper 1987–280*, Jan. 1987.

[36] Gnoffo, P. A., "Computational Fluid Dynamics Technology for Hypersonic Applications," *AIAA Paper 2003–3259*, July 2003.

[37] Hash, D., Olejniczak, J, Wright, M, Dinish, P., Pulsonetti, M., Hollis, B., Gnoffo, P., Barnhard, M, Nompelis, I, and Candler, G, "FIRE II Calculations for Hypersonic Nonequilibrium Aerothermodynamics Code Verification: DPLR, LAURA, and US3D," *AIAA Paper 2007–605*, 2007.

[38] Wright, M. J. and Candler, G. V., "A Data-Parallel Line Relaxation method for the Navier-Stokes equations," *AIAA Paper 1997–2046*, 1997.

[39] Wright, M. J. and andBose, D., C., "Data-Parallel Line Relaxation Method for the Navier-Stokes Equations," *AIAA Journal*, Vol. 36, No. 9, 1998.

[40] Wright, M. J., Bose, D., and Olejniczak, J.

[41] Walpot, L., *evelopment and Application of a Hypersonic Flow Solver*, Ph.D. thesis, T.U. Delft University, 2002.

[42] Mavriplis, D. J., "Revisiting the Least-squares Procedure for Gradient Reconstruction on Unstructured Meshes," Technical Report CR-2003-212683, NASA, 2003.

[43] Nompelis, I., Drayna, T. W., and Candler, G. V., "A Parallel Unstructured Implicit Solver for Hypersonic Reacting Flow Simulation," *AIAA Paper 2005–4867*, Jun 2005.

[44] Nelson, H. F., Park, C., and Whiting, E. E., "Titan Atmospheric Composition by Hypervelocity Shock-Layer Analysis," *AIAA Paper 1989–1770*, 1989.

[45] Park, C. S. and Bershader, D., "Determination of The Radiative Emission of Hypersonic Flow Simulating The Cassini-Titan Atmospheric Entry Probe Environment," *AIAA Paper 1990–1558*, 1990.

[46] Koffi-Kpante, K., Zeitoun, D., and Labracherie, L., *Shock Waves*, Vol. 7, 1997.

[47] Takashima, N., Hollis, B. R., Zoby, E. V., Sutton, K., Olejniczak, J., and Prabhu, D., "Preliminary Aerothermodynamics of Titan Aerocapture Aeroshell," *AIAA Paper 2003–4952*, 2003.

[48] Bhat, M. K. and Parikh, P., "Parallel Implementation of an Unstructured Grid-Based Navier-Stokes Solver," *AIAA Paper 99–16526*, Jan 1999.

[49] Parikh, P., "Application of a Scalable, Parallel, Unstructured Grid-Based Navier-Stokes Solver," *AIAA Paper 2001–2584*, Jun 2001.

[50] Park, Y. M. and Kown, O. J., "A Parallel Unstructured Dynamic Mesh Adaptation Algorithm for 3-D Unsteady Flows," *International Journal for Numerical Methods in Fluids*, Vol. 48, No. 6, June 2005, pp. 671–690.

[51] Karypis, G. and Kumar, V., "A fast and high qualitymultilevel scheme for partitioning irregular graphs," Technical Report TR 95-035, Department of Computer Science, University of Minnesota, 1995, Also available on WWW at URL http://www.cs.umn.edu/users/kumar/papers/mlevel serial.ps.

[52] Karypis, G. and Kumar, V., "Unstructured graph partitioning and sparse matrix ordering system," Tech. rep., Department of Computer Science, University of Minnesota, 1995, Available on WWW at URL http://www.cs.umn.edu/users/kumar/metis/metis.html.

[53] Pajarola, R. and Widmayer, P., "An Image Compression Method for Spatial Search," *IEEE TRANSACTIONS ON IMAGE PROCESSING*, Vol. 9, No. 3, 2003.

[54] Mitchell, L. K., "Techniques for Artistically Rendering Space-Filling Curves," Associate Professor of University of Advancing Technology.

[55] Hill, D. C., "Cartesian Mesh Generation and Highly-Compressed Storage Using Hilbert Codes," *AIAA Paper 2004–240*, Jan 2004.

[56] Aftosmis, M. J., Berger, M. J., and Murman, S. M., "Applications of Space-Filling-Curves to Cartesian Methods for CFD," *AIAA Paper 2004–1232*, Jan 2004.

[57] Peano, G., "Sur une Courbe qui Remplit Toute une Aire Plane," *Math. Ann.*, Vol. 36, 1890, pp. 157–160.

[58] Hilbert, G., "U ber die stetige Abbildung einer Linie auf Flachenstu ck," *Math. Ann.*, Vol. 38, 1891, pp. 459–460.

[59] Jagadish, H. V., "Linear Clustering of Objects with Multiple Attributes," Proc. ACM SIGMOD Conf., May 1990, pp. 332–342.

[60] Bonnie J. McBride, M. and Sanford Gordon, "NASA Glenn Coefficients for Calculating Thermodynamics Properties of Individual Species," Technical Paper TP-2002-211556, NASA, Sep 2002.

[61] Ait-Ali-Yahia, D and Habashi, W. G., "Finite Element Adaptive Method for Hypersonic Thermochemical Nonequilibrium Flows," *AIAA Journal*, Vol. 35, No. 8, 1997.

[62] Dunn, M. G. and Kang, S. W., "Theoretical and Experimental Studies of Reentry Plasmas," Technical Report CR-2232, NASA, Apr 1973.

[63] Park, C., "On Convergence of Computation of Chemically Reacting Flows," *AIAA Paper 85–0247*, 1985.

[64] Park, C., "A Review of Reaction Rates in High Temperature Air," *AIAA Paper 89–1720*, 1989.

[65] Park, C., "Review of Chemical-Kinetic Problems of Future NASA Missions," *Journal of Thermodynamics and Heat Transfer*, Vol. 7, No. 3, 1989.

[66] Gökçen, "N2-CH4-Ar Chemical Kinetic Model for Simulations of Atmospheric Entry to Titan," *AIAA Paper 2004–2469*, 2004.

[67] Park, C., "Assessment of Two-Temperature kinetic Model for Ionizing Air," *AIAA Paper 87–1574*, 1987.

[68] Millokan, R. C. and White, D. R., "Systematics of Vibrational Relaxation," *Journal of Chemical Physics*, Vol. 39, No. 12, 1963, pp. 3209–3213.

[69] Landau, L. and Teller, E., "Zur Theorie der Schalldispersion," *Physik Z. Sowjetunion*, Vol. 10, No. 1, 1963, pp. 34.

[70] Park, C., "Problems of Rate Chemistry in the Flight Regimes of Aeroassisted Orbital Trnasfer Vehicle," *Progress in Astronautics and Aeronautics, AIAA*, Vol. 96, 1985.

[71] Kim, K. H., Kim, C., and Rho, O. H., "Accurate Computations of Hypersonic Flows Using AUSMPW+ Scheme and Shock-Aligned Grid Technique," *Journal of Computational Physics*, Vol. 174, No. 38-80, 2001.

[72] Kim, K. H., Kim, C., and Rho, O. H., "Methods for the Accurate Computations of Hypersonic Flows," *AIAA Paper 98–2442*, 1998.

[73] Liou, M. S. and Steffen Jr., C. J., "A New Flux Splitting Scheme," *Journal of Computational Physics*, Vol. 107, No. 23-39, 1993.

[74] Liou, M. S. and Wada, Y., "A New Flux Splitting Scheme with High-Resolution and Robustness for Discontinuities," *AIAA Paper 94–0083*, 1994.

[75] Kim, K. H. and Rho, O. H., "An Improvement of AUSM schemes by introducing the pressure-based weight functions," *Computational Fluids*, Vol. 27, No. 331, 1998.

[76] Barbante, P. F., *Accurate and Efficient Modeling of High Temperature Nonequilibrium Air Flows*, Ph.D. thesis, Von Karman Institution, 2001.

[77] Vetter, M., Oliver, H., and Grönig, H., *"Flow over Double Ellipsoid and Sphere-Experimental Results", Hypersonic Flows for Reentry Problems*, Vol. 3, Academic Press, 1974.

[78] White, F. M., *Viscous Fluid Flow*, McGraw-Hill, 1991.

[79] Nompelis, I., Drayna, T. W., and Candler, G. V., "Development of Stencil-Based Mesh Partitioning for Parallel Unstructuted CFD Solvers," *AIAA Paper 2007–4087*, Jun 2007.

[80] Westhelle, C. and Masciarelli, J., "Assessment of aerocapture flight at itan using a drag-only device," *AIAA Paper 2003–5389*, 2003.

[81] James, B., Munk, M., and Moon, S., "Aerocapture technology project overview," *AIAA Paper 2003–4654*, 2003.

[82] Miller, K., Masciarelli, J., Hausle, F., Riesco, M., Sharma, D., Zeller, C., Gnoffo, P., Buck, G., Ware, J., and Rohrschneider, R., "Ultralightweight ballute technology for aerocapture and aeroassist missions," Technical Paper NASA-CR-1999-000000, NASA, Jan 2007.

[83] Johnson, W. and Lyons, D., "Titan ballute aerocapture using a perturbed TitanGRAM model," *AIAA Paper 2004–5280*, 2004.

[84] Brown, G. and Richardson, E., "Minimum-mass design for Titan aerocapture," *AIAA Paper 2005–1637*, 2005.

[85] Livermore Software Technology Corp., WWW at URL http://www.ls-dyna.com, *LS-DYNA Company Website*.